ATLAS jet trigger performance in Run 2 and searching for new physics with trigger-level jets

Dissertation

Presented in Partial Fulfillment of the Requirements for the Degree Doctor of Philosophy in the Graduate School of The Ohio State University

By

Bryan Reynolds, B.S., M.S.

Graduate Program in Physics

The Ohio State University

2021

CERN-THESIS-2021-237
16/11/2021

Dissertation Committee:

Professor Antonio Boveia, Advisor

Professor Linda Carpenter

Professor Stanley Durkin

Professor Christopher Hirata

© Copyright by

Bryan Reynolds

2021

Abstract

Hadronic jets play a vital role in the search for physics beyond the Standard Model at particle colliders. Jets are the most commonly produced collision products at hadron colliders like the LHC, and thus represent an extremely promising avenue for discovery. While this prevalence allows for Standard Model processes to be measured to extreme precision and exciting new physics to be searched for, analysis using jets comes with many challenges. The high rate of collision events that produce jets naturally leads to a large background that must be sorted through so that the most interesting events may be identified and recorded. This requires robust jet reconstruction, calibration, and triggering in order to maximize the amount of interesting jet events that can be analyzed for potential new discoveries.

In this thesis, an analysis of the performance of the ATLAS jet trigger system during CERN LHC Run 2 is presented. Jet Trigger efficiency curves are analyzed for the full suite of HLT triggers from each year of Run 2 data collection, with differences in run conditions from year to year reviewed and their impacts on jet trigger efficiency analyzed. The effects of an improved jet calibration scheme implemented midway through Run 2 on jet trigger efficiencies and the fraction of recorded fully efficient data that is most useful for further physics analysis are investigated.

Additionally, a search for new physics using dijet events at the trigger level is presented. Results of a partial Run 2 analysis using data collected through 2016 are presented and contributions to an upcoming full Run 2 analysis are discussed.

This thesis is dedicated to my loving family and friends.

Acknowledgments

I have been very fortunate to have met so many wonderful friends and colleagues from all around the world throughout my PhD journey. It is impossible to thank everyone who has made a positive impact on my life during these years in just a few pages, so to any friends who I do not explicitly mention, I express my sincerest gratitude for all of the happiness that you have added to my life.

First, I would like to thank my advisor, Dr. Antonio Boveia. Without his guidance, support, patience, and incredible knowledge none of this would have been possible. His advice at every step of the way has been truly invaluable. I would also like to thank the rest my thesis committee- Dr. Linda Carpenter, Dr. Stan Durkin, and Dr. Chris Hirata. Without their continuous support this thesis would not exist.

Through my association with CERN, I have had the pleasure of working alongside so many brilliant collaborators from all around the world. Dr. Caterina Doglioni has been a great mentor throughout much of my PhD journey, and I am immensely grateful for her constant enthusiasm and support. Dr. Will Kalderon, Dr. Steven Schramm, and Dr. Emma Tolley have been an absolute pleasure to learn from and work alongside on several projects.

I would also like to thank Dr. Miguel Mostafa. By opening his door to me as an undergraduate student at Penn State, he gave me my first experience with physics research and motivated me to continue along this path. I can confidently say that I

would never have come this far without his mentorship at the very beginning of my academic career.

I am grateful for the many residents of PRB 3000- Joey Adams, Chris Cappiello, Bryan Cardwell, Khan Cox, Kevin Jamison, Keith McBride, Brent Noesges, Amber Simmons, Bryan Smith, and Rebekah Smith- who turned the late nights of seemingly endless coursework into an experience that I will look back on fondly. I do not know how I would have survived those first few years without them.

I would also like to thank Allie Snyder, Julie Rolla, and Sean Chilleli for being some of the closest and most supportive friends that I have ever had. I am so thankful for the wonderful memories that we have made over the past few years and I look forward to many more good times.

I am thankful that I had the privilege of spending a year in Geneva, Switzerland where I was so incredibly lucky to find a fantastic group of housemates- Rado, Ramzi, Matthias, Kirsty, Fiona, Plami, Aidan, Helia, Dom, Giulia, Alan, Konstantina, Emil, and the rest of the Noyeres family. This wonderful group made a foreign country feel like home and I can't wait to go back and visit as soon as I can.

Last, and certainly not least, I would like to thank my family- my parents, Debra and the late John Reynolds, and my brother, John (and of course my cat, Denver). Without all of you and your love I would not be the person that I am today.

The research for this thesis was supported in part by the US Department of Energy (grant DE-SC0011726).

Vita

May 6, 1993	Born - West Chester, PA, USA
2014	Bert Elsbach Honors Scholarship in Physics, Pennsylvania State University
2015	B.S. Physics, Pennsylvania State University
2015-2017	Graduate Teaching Associate, The Ohio State University
2017	Hazel Brown Outstanding Teaching Assistant Award, The Ohio State University
2017	M.S. Physics, The Ohio State University
2017-2021	Graduate Research Associate, The Ohio State University
2021-present	Graduate Teaching Associate, The Ohio State University

Publications

Research Publications

Included in author list of 123 publications from ATLAS

ATLAS Collaboration. Search for Low-Mass Dijet Resonances Using Trigger-Level Jets with the ATLAS Detector in pp Collisions at $\sqrt{s}$=13 TeV. *Phys. Rev. Lett.* 121, 081801, 2018.

Fields of Study

Major Field: Physics

Table of Contents

Page

Abstract ii

Dedication iv

Acknowledgments v

Vita vii

List of Tables xii

List of Figures xiii

1. Introduction and Theory 1

    1.1 The Standard Model 1
        1.1.1 Fundamental Particles and Interactions 2
    1.2 Quantum Chromodynamics 4
        1.2.1 Parton Distribution Function 5
        1.2.2 Showering and Hadronization 7
    1.3 Beyond Standard Model Physics 8
        1.3.1 Evidence for Beyond Standard Model Physics 8
        1.3.2 Jets as a Potential Discovery Channel at the LHC 10

2. The Large Hadron Collider and ATLAS Experiment 13

    2.1 The Large Hadron Collider 13
        2.1.1 Beam Injection Chain 14
        2.1.2 Acceleration Mechanisms 17
        2.1.3 Bunch Filling and Pileup 19
    2.2 The ATLAS Detector 21
        2.2.1 Coordinate System 21

2.2.2 Inner Detector . . . 23
2.2.3 Calorimeters . . . 26
2.2.4 Muon Spectrometer . . . 35
2.2.5 Magnetic System . . . 39
2.2.6 Trigger System . . . 40

3. Jet Physics in ATLAS . . . 44

3.1 Jet Reconstruction . . . 44
3.1.1 Detector Signatures . . . 45
3.1.2 Jet Reconstruction Algorithms . . . 49
3.2 Jet Calibration . . . 51
3.2.1 Origin Correction . . . 52
3.2.2 Pileup Correction . . . 52
3.2.3 MC-Based Calibrations . . . 55
3.2.4 In Situ Calibrations . . . 60
3.3 Jet Energy Resolution and Cross-Section . . . 63
3.3.1 Jet Energy Resolution . . . 64
3.3.2 Jet Cross-Section . . . 66

4. Run-2 Jet Trigger Studies . . . 70

4.1 Jet Triggering . . . 71
4.1.1 Jet Trigger Menu . . . 73
4.1.2 Jet Trigger Prescaling . . . 75
4.2 Jet Trigger Efficiency Studies . . . 76
4.2.1 Introduction to Trigger Efficiency Curves . . . 77
4.2.2 Results From Run-2 Data . . . 81
4.3 Jet Trigger Impacts On Data . . . 111
4.4 Future Perspectives . . . 118

5. Search for New Physics with Dijet Trigger Level Analysis . . . 119

5.1 Dijet Searches And Trigger Level Analysis Motivation . . . 119
5.2 Analysis Strategy . . . 124
5.2.1 TLA Data Sample . . . 124
5.2.2 Trigger-Level Jet Calibration . . . 125
5.2.3 TLA Event Selection . . . 127
5.2.4 Background Estimation . . . 129
5.3 Results . . . 130
5.4 Full Run-2 Dijet TLA Analysis and End-Of-Fill Data . . . 133
5.5 Future Trigger-Level Analyses . . . 138

6. Conclusion 140

Bibliography 142

List of Tables

Table **Page**

4.1 The main ATLAS triggers used in 2015 for runs with peak luminosity $L = 5 \times 10^{33}$ $cm^{-2}s^{-1}$. The total rate shown here is for the full trigger menu, which includes many more triggers than those shown here. The information pertaining to jet triggers shown here is for several common lowest un-prescaled triggers [20] 72

4.2 Table showing example jet trigger names and descriptions. Many more triggers exist in the full trigger menu, but a sampling of the naming schemes are shown here. 74

4.3 Efficiency points for the various single jet triggers active in each year of Run 2 data collection as taken from the efficiency curves for each trigger. 114

4.4 The percentage of data collected using the full suite of single jet triggers that satisfies the listed trigger efficiency thresholds in each year. . . . 117

List of Figures

Figure **Page**

1.1 A summary of the SM, representing the current understanding of particle physics. Particle properties such as mass, charge, spin, and color are indicated. Also shown is a theorized but unconfirmed BSM particle, the graviton, which would act as a force carrier for the gravitational force [1]. 3

1.2 The parton distribution functions calculated from analysis of available hard scattering data. Shown here is the longitudinal momentum fraction, x, times the PDF, $f(x, Q)$, as a function of x for momentum transfer scales $Q^2 = 10$ GeV^2 (left) and $Q^2 = 10^4$ GeV^2 (right). PDFs are from the MMHT collaboration [36]. 6

2.1 Schematic diagram of the LHC ring showing the main detector positioning [16] 15

2.2 Schematic diagram of the LHC accelerator complex [15] 16

2.3 Interactions per bunch crossing for proton-proton collision data collected in each year of Run 2 [19] 20

2.4 A computer-generated schematic diagram of the full ATLAS detector [43] 22

2.5 A sketch of the ATLAS coordinate System [46] 23

2.6 A computer-generated schematic diagram of the ATLAS inner detector [41] 25

2.7 A computer-generated image showing a detailed view of the layers of the ATLAS inner detector [9] 27

2.8 A computer-generated image showing the full ATLAS calorimeter system with each component labeled [40] 28

2.9 A schematic diagram depicting a portion of the ATLAS EM calorimeter in the barrel region [47] 31

2.10 A schematic diagram depicting the full ATLAS hadronic tile calorimeter (left) and a detailed view of an individual tile module (right) [8] . 33

2.11 A schematic diagram depicting a cross-sectional view of the ATLAS hadronic tile calorimeter with tiles labeled [28] 34

2.12 A plot of stopping power for muons passing through copper as a function of muon momentum [48] 36

2.13 A computer-generated image showing the full ATLAS Muon Spectrometer [42] 37

2.14 A schematic diagram showing a cross-sectional view of the ATLAS Muon Spectrometer in the barrel region [21] 38

2.15 Schematic diagram of the ATLAS magnetic system [39] 40

2.16 Example L1 physics trigger rates from a typical run. Trigger rates shown are based on physics objects like electromagnetic clusters (EM), muon candidates (MU), jet candidates (J), missing transverse energy (XE) and tau candidates (TAU) [20] 42

2.17 Example HLT physics trigger rates from a typical run for each physics group. [20] 43

3.1 A sketch of topoclusters formed from a hypothetical calorimeter signal with the three types of cell classifications highlighted [38]. 47

3.2 Example outputs of each jet reconstruction algorithm when applied to simulated data [13]. 51

3.3 Example distributions of median p_T-density ρ for varying pileup conditions as measured by N_{PV}. [31] 54

3.4 Results of pileup subtraction showing the dependence of jet p_T on N_{PV}(a) and μ (b) as a function of $|\eta|$ N_{PV}. [31] 56

3.5 Representative example jet energy response plots at various reconstructed jet energy values. Plots depicted here show the jet energy response for small-R PFlow jets as a function of detector η. [31] . . . 57

3.6 Data-to-MC response ratio after each stage of the in situ calibration, shown here for small-R PFlow jets with JES calibrations applied. The black curve shows the result of the full in situ calibration. The purple band shows the total uncertainty of the full in situ curve and the red band shows only the statistical component of the uncertainty [31]. . . 63

3.7 (a) The jet energy resolution as a function of jet p_T, shown here for fully calibrated PFlow jets. Also shown is the isolated JER noise term and a comparison to the expected JER results from simulation. (b) Total uncertainty of the JER as a function of jet p_T, with individual contributions shown [31]. 65

3.8 (a) A comparison of the jet energy resolution for fully calibrated PFlow and EMTopo jets (a) as a function of jet p_T and (b) as a function of jet $|\eta|$ [31]. 66

3.9 Measured inclusive jet cross-sections as a function of jet p_T in six bins of $|y|$. A comparison to QCD simulation using the NLOJET++ package (yellow) is presented for comparison [27] 68

3.10 Measured dijet cross-sections as a function of dijet system invariant mass in six bins of y^*. A comparison to QCD simulation using the NLOJET++ package (yellow) is presented for comparison [27] 69

4.1 An example jet trigger turn-on curve showing the efficiency of the probe trigger HLT_j420 using HLT_j260 as the reference trigger with 2018 data. 77

4.2 (a) The cumulative integrated luminosity vs time over the course of LHC Run 2 proton-proton data taking. Shown is the LHC delivered, representing the luminosity delivered from the start of stable beams until ATLAS is put in standby mode, ATLAS recorded, which accounts for data acquisition inefficiencies and startup times of various sub detectors, and good for physics, representing when all reconstructed physics objects are of good quality, integrated luminosity distributions [19]. (b) Interactions per bunch crossing for proton-proton collision data collected in each year of Run 2 [19]. 82

4.3 The full set of single jet HLT trigger efficiency curves active in 2015 (a), 2016 (b), 2017 (c), and 2018 (d). 83

4.4 A zoomed-in view of the efficiency curves depicted in Figure 4.3a showing the lower-p_T (a), mid-p_T (b), and high-p_T (c) ranges of the 2015 single jet triggers. 84

4.5 A zoomed-in view of the efficiency curves depicted in Figure 4.3b showing the lower-p_T (a), mid-p_T (b), and high-p_T (c) ranges of the 2016 single jet triggers. 85

4.6 A zoomed-in view of the efficiency curves depicted in Figure 4.3c showing the lower-p_T (a), mid-p_T (b), and high-p_T (c) ranges of the 2017 single jet triggers. 86

4.7 A zoomed-in view of the efficiency curves depicted in Figure 4.3d showing the lower-p_T (a), mid-p_T (b), and high-p_T (c) ranges of the 2018 single jet triggers. 87

4.8 The full set of single forward jet ($3.2 < |\eta| < 4.9$) HLT trigger efficiency curves active in 2015 (a), 2016 (b), 2017 (c), and 2018 (d). 88

4.9 A zoomed-in view of the efficiency curves depicted in Figure 4.8a showing the lower-p_T (a), mid-p_T (b), and high-p_T (c) ranges of the 2015 single forward jet triggers. 89

4.10 A zoomed-in view of the efficiency curves depicted in Figure 4.8b showing the lower-p_T (a), mid-p_T (b), and high-p_T (c) ranges of the 2016 single forward jet triggers. 90

4.11 A zoomed-in view of the efficiency curves depicted in Figure 4.8c showing the lower-p_T (a), mid-p_T (b), and high-p_T (c) ranges of the 2017 single forward jet triggers. 91

4.12 A zoomed-in view of the efficiency curves depicted in Figure 4.8d showing the lower-p_T (a), mid-p_T (b), and high-p_T (c) ranges of the 2018 single forward jet triggers. 92

4.13 A selection of multi-jet HLT trigger efficiency curves active in 2015 (a), 2016 (b), 2017 (c), and 2018 (d). Note that more multi-jet triggers were active in each year that are not displayed here. Instead, the sets of triggers included here are intended to summarize the range of signatures covered by multi-jet triggers in each year. The x-axis shows the nth jet p_T, where n represents the jet multiplicity required by each trigger 94

4.14 A zoomed-in look at the j45 triggers with varying jet multiplicity active in 2015. The x-axis shows the nth jet p_T, where n represents the jet multiplicity required by the trigger, i.e. HLT_nj45. 95

4.15 A zoomed-in look at the j45 triggers with varying jet multiplicity active in 2016. The x-axis shows the nth jet p_T, where n represents the jet multiplicity required by the trigger, i.e. HLT_nj45. 96

4.16 A zoomed-in look at the j45 triggers with varying jet multiplicity active in 2017. The x-axis shows the nth jet p_T, where n represents the jet multiplicity required by the trigger, i.e. HLT_nj45. 97

4.17 A zoomed-in look at the j45 triggers with varying jet multiplicity active in 2018. The x-axis shows the nth jet p_T, where n represents the jet multiplicity required by the trigger, i.e. HLT_nj45. The uncharacteristic uptick in the 2018 trigger turn-on curve is due to the threshold of the reference trigger being too close to that of the j45 trigger being analyzed, as discussed in Section 4.2.1. 98

4.18 An inter-year comparison of the lowest unprescaled single jet trigger efficiency curves from each year of Run-2 data taking. Note that the lowest unprescaled trigger changes from year to year, going from HLT_j360 to HLT_j380 to HLT_j420 in 2015, 2016, and 2017/2018, respectively. 100

4.19 An inter-year comparison of the lowest unprescaled 4j multi-jet trigger efficiency curves from each year of Run-2 data taking. Note that the lowest unprescaled 4j trigger changes from year to year, going from HLT_4j85 to HLT_4j100 to HLT_4j120 in 2015, 2016, and 2017/2018, respectively. The 4j multi-jet trigger was chosen as a benchmark for comparing the trigger efficiency of the lowest unprescaled multi-jet triggers from each year. 102

4.20 An inter-year comparison of the HLT_j45 jet trigger efficiency curves from each year of Run-2 data taking. This trigger was selected as a benchmark for comparing the relative trigger efficiency from year to year. The uncharacteristic uptick in the 2018 trigger turn-on curve is due to the threshold of the reference trigger being too close to that of the j45 trigger being analyzed, as discussed in Section 4.2.1. 103

4.21 A comparison of the lowest unprescaled single jet trigger efficiency curves in 2017/2018 (HLT_j420) at each stage of the jet calibration chain. Data shown here is from the 2017 data-taking period only, as this is when the updated jet calibration scheme went into effect. 2018 data is not shown, but is expected to behave similarly as it relied on the same calibration scheme. 105

4.22 A comparison of the lowest unprescaled single jet trigger efficiency curves in 2017/2018 (HLT_j420), explicitly showing the effects of the additional calibrations added prior to data collection in 2017. Data shown here is from the 2017 data-taking period only, however a curve showing the 2016 calibration scheme applied to the 2017 data is shown for comparison. The calibration stages shown here include through the Jet Energy Scale calibration (the full 2016 calibration), with the trackless (calorimeter input only) GSC calibration step added, with the trackless GSC and in-situ calibration steps added, and with the full GSC calibration with tracks and in-situ steps added (the full, optimal 2017/2018 calibration). 106

4.23 A comparison of the lowest unprescaled 4j multi-jet trigger efficiency curves in 2017/2018 (HLT_4j120) at each stage of the jet calibration chain. Data shown here is from the 2017 data-taking period, when the updated jet calibration scheme went into effect. 2018 data is not shown, but is expected to behave similarly as it relied on the same calibration scheme. 107

4.24 A comparison of the lowest unprescaled 4j multi-jet trigger efficiency curves in 2017/2018 (HLT_4j120), explicitly showing the effects of the additional calibrations added prior to data collection in 2017. Data shown here is from the 2017 data-taking period only, however a curve showing the 2016 calibration scheme applied to the 2017 data is shown for comparison. The calibration stages shown here include through the Jet Energy Scale calibration (the full 2016 calibration), with the trackless (calorimeter input only) GSC calibration step added, with the trackless GSC and in-situ calibration steps added, and with the full GSC calibration with tracks and in-situ steps added (the full, optimal 2017/2018 calibration). 108

4.25 A comparison of the lowest unprescaled 7j multi-jet trigger efficiency curves in 2017/2018 (HLT_7j45) at each stage of the jet calibration chain. Data shown here is from the 2017 data-taking period, when the updated jet calibration scheme went into effect. 2018 data is not shown, but is expected to behave similarly as it relied on the same calibration scheme. 109

4.26 A comparison of the lowest unprescaled 7j multi-jet trigger efficiency curves in 2017/2018 (HLT_7j45), explicitly showing the effects of the additional calibrations added prior to data collection in 2017. Data shown here is from the 2017 data-taking period only, however a curve showing the 2016 calibration scheme applied to the 2017 data is shown for comparison. The calibration stages shown here include through the Jet Energy Scale calibration (the full 2016 calibration), with the trackless (calorimeter input only) GSC calibration step added, with the trackless GSC and in-situ calibration steps added, and with the full GSC calibration with tracks and in-situ steps added (the full, optimal 2017/2018 calibration). 110

4.27 The offline leading jet p_T for all events passing a minimum of one single jet trigger (HLT_jX) in 2015 data. Shaded regions indicate where the single jet triggers satisfy a specified efficiency threshold and therefor the regions where the data may be safe to use in further physics analyses. This analysis uses the 80% (red), 90% (violet), 95% (blue), and 99% (black) efficiency points. 112

4.28 The offline leading jet p_T for all events passing a minimum of one single jet trigger (HLT_jX) in 2016 data. Shaded regions indicate where the single jet triggers satisfy a specified efficiency threshold and therefor the regions where the data may be safe to use in further physics analyses. This analysis uses the 80% (red), 90% (violet), 95% (blue), and 99% (black) efficiency points. 113

4.29 The offline leading jet p_T for all events passing a minimum of one single jet trigger (HLT_jX) in 2017 data. Shaded regions indicate where the single jet triggers satisfy a specified efficiency threshold and therefor the regions where the data may be safe to use in further physics analyses. This analysis uses the 80% (red), 90% (violet), 95% (blue), and 99% (black) efficiency points. 115

4.30 The offline leading jet p_T for all events passing a minimum of one single jet trigger (HLT_jX) in 2018 data. Shaded regions indicate where the single jet triggers satisfy a specified efficiency threshold and therefor the regions where the data may be safe to use in further physics analyses. This analysis uses the 80% (red), 90% (violet), 95% (blue), and 99% (black) efficiency points. 116

5.1 Limits set by various collider experiments on coupling g_B between quarks and a theoretical Z' particle as a function of the Z' mass. The regions above each contour are excluded, meaning that for a given value of Z' mass along the x-axis, coupling values above each curve have been ruled out by the experiment responsible for setting the limit [32] 121

5.2 The full HLT event rate separated in terms of various data streams (a) and the corresponding trigger bandwidth used by each data stream (b) for a representative run from 2017 data collection [20]. 122

5.3 The number of dijet events as a function of dijet invariant mass, m_{jj}, collected for use in the TLA analysis (black points) compared to the number of events as selected by single jet triggers with prescaling applied (blue line). Also shown is the number of events corrected for prescaling (red line), representing the expected number of events if the single jet triggers were unprescaled [29]. 123

5.4 The calibration steps applied to trigger-level jets.[29] 125

5.5 The trigger-level in situ calibration curve for both the spline (dashed line) and polynomial $\log(p_T)$ fitted (solid line) combination methods. The lower panel shows the ratio between the curves generated by the two combination methods [29]. 127

5.6 The dijet invariant mass distribution reconstructed from trigger-level jets from the $|y^*| < 0.3$ and $|y^*| < 0.6$ signal regions. The results from data (black points) are compared against the background estimates (solid lines). The agreement between data and background is analyzed using the BumpHunter algorithm, with the most discrepant region marked (dashed lines). Also shown are two possible signal models of a hypothetical Z' particle as an example of how a significant signal over background would appear [29]. 131

5.7 The 95% confidence-level upper limits on g_q as a function of m'_Z for the leptophobic Z' dark matter model. A portion of the limits set by an offline dijet search[26] is shown for additional context [29]. 132

5.8 The 95% confidence-level upper limits on cross-section times acceptance as a function of m_G for a generic Gaussian signal model. Limits are calculated for four relative Gaussian widths σ_G/m_G [29]. 133

5.9 A summary of limits set on a Z' dark matter model by various ATLAS dijet searches. Limits on the coupling between quarks and the Z' particle, g_q, as a function of the particle mass, m'_Z. The constraints set by the dijet TLA are shown in blue [30]. 134

5.10 The L1 trigger rate and the rates of L1 triggers that seed the TLA data stream as a function of instantaneous luminosity (a) and time (b) for a LHC fill taken in 2018. The jumps in trigger rate seen are due to adjustments in prescaling at set luminosity thresholds.[20] 135

5.11 The HLT trigger rate as a function of time (a) and the corresponding HLT output bandwidth (b) for all trigger streams for a LHC fill taken in 2018.[20] 136

5.12 The L1 trigger efficiencies for single jet triggers key to seeding the TLA data stream in 2015/2016. The 2016 TLA used data seeded by the L1_J75 and L1_J100 triggers. The efficiencies of these triggers are expected to behave similarly in 2017 and 2018 data [18]. 137

Chapter 1: Introduction and Theory

In this chapter, the underlying theoretical foundation that motivates the contents discussed in the rest of this document is presented. A brief overview of the Standard Model (SM) of particle physics is presented and the known particles and interactions of the universe are discussed. Some of the shortcomings in the SM that motivate the search for beyond standard model (BSM) physics phenomena at particle colliders are highlighted. A brief overview of hadronic jet physics is presented and some of the motivations for searching for BSM phenomena using hadronic jets as a discovery mode are discussed.

1.1 The Standard Model

The SM of particle physics [12] is the most successful theory to date in terms of accurately describing the matter that makes up the universe at the particle level. The SM is a relativistic quantum field theory based on the gauge invariant symmetry group $SU(3) \bigotimes SU(2) \bigotimes U(1)$. The theory describes the fundamental interactions of quantum chromodynamics (QCD), quantum electrodynamics (QED), and the weak interaction. This accounts for three of the four fundamental forces of nature- the

strong nuclear force, the electromagnetic force, and the weak nuclear force. Gravity, the fourth fundamental force, is negligible at the particle level and is presently unaccounted for in the SM.

1.1.1 Fundamental Particles and Interactions

Particles in the SM are categorized as either fermions or bosons. The former are the particles making up the matter of the universe and the latter act as force carriers. Fermions are spin $\frac{1}{2}$ particles that are further categorized as either quarks or leptons. Fermions exist in three generations of increasing mass, each with two quarks and two leptons, amounting to a total of six quarks and six leptons. All fermions have an oppositely charged antimatter counterpart. Bosons, with the exception of the Higgs, are spin 1 particles. There are four such spin 1 bosons in total. The Higgs boson is a scalar particle, making it the only spin 0 particle in the SM, that is responsible for giving mass to the other SM particles. Figure 1.1 shows the various particles included in the SM, summarizing their properties such as mass, charge, spin, and color.

Figure 1.1 denotes the first generation of fermions as stable matter because the fermions in the higher, more massive generations promptly decay to lighter particles. Thus, the matter on Earth is made up of first generation fermions, with standard atoms containing up and down quarks and electrons.

A simplified version of the SM Lagrangian is given in Equation 1.1. The Lagrangian provides a mathematical description of the SM, describing the interactions between each class of particle. The first term describes the interactions between gauge bosons. The second line describes the interactions between fermions and gauge bosons. The third line describes the interactions of fermions with the Higgs field.

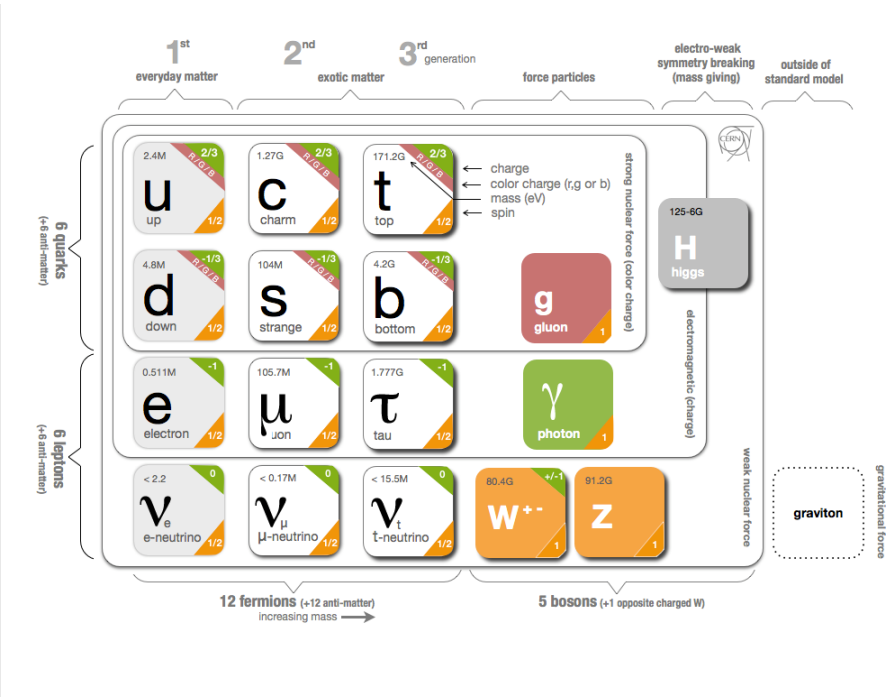

Figure 1.1: A summary of the SM, representing the current understanding of particle physics. Particle properties such as mass, charge, spin, and color are indicated. Also shown is a theorized but unconfirmed BSM particle, the graviton, which would act as a force carrier for the gravitational force [1].

The fourth line describes the interactions between gauge bosons and the Higgs field and adds the Higgs potential, which describes the Higgs boson coupling with itself.

$$\begin{aligned}\mathcal{L}_{SM} = & -\frac{1}{4}F_{\mu\nu}F^{\mu\nu} \\ & + i\bar{\psi}\not{D}\psi + h.c. \\ & + \psi_i y_{ij}\psi_j\phi + h.c. \\ & + |D_\mu\phi|^2 - V(\phi)\end{aligned} \tag{1.1}$$

The SM Lagrangian is based on the $SU(3) \bigotimes SU(2) \bigotimes U(1)$ symmetry group. Each gauge invariant symmetry translates to one of the fundamental forces of nature. The $SU(3)$ symmetry group generates the eight gluons (one for each possible color charge), which carry the strong nuclear force. The $SU(2)$ symmetry group generates the W^+, W^-, and Z bosons, which carry the weak nuclear force. The $U(1)$ symmetry group generates the photon, which carries the electromagnetic force. Notably missing is the fourth fundamental force, gravity, which is not included in the SM. A new boson, the graviton (included in Figure 1.1), has been theorized outside of the SM but has not been proven to exist.

All of these symmetries and corresponding fundamental forces are obviously important to the theory of particle physics, but the strong nuclear force and the theory of Quantum Chromodynamics (QCD) will be the focus of the next section. This is because hadronic jets, their measurement, and their potential as a discovery mode for new physics are central to the analyses discussed in Chapters 4 and 5.

1.2 Quantum Chromodynamics

The theory of QCD [33] describes the interactions of quarks, the fundamental particles making up hadronic matter, and gluons, the force carrier of the strong nuclear force responsible for binding quarks together. QCD introduces the color charge as a conserved quantity. Both quarks and gluons carry color charge, and thus their interactions are primarily mediated by the strong force. Gluons carry no electric charge, but quarks carry fractional electric charge, with the up, charm, and top quarks having a $\frac{2}{3}e$ charge and the down, strange, and bottom quarks having a $-\frac{1}{3}e$ charge.

Free particles with fractional electric charge and non-color-neutral states have not been observed in nature, and thus individual quarks are not observed by themselves. The concept that quarks must remain in color-neutral bound states and cannot be observed as free particle is known as color confinement. In order for quarks to remain in color-neutral bound states, the strong force must increase with distance. Since gluons also carry color charge, they undergo self-interactions which limits the range of the strong force and causes the strong coupling constant to increase with distance. Conversely, at very small distances, the strong force coupling constant decreases to the extent that quarks behave as nearly free particles. This effect is known as asymptotic freedom. These concepts have profound impacts on the dynamics of QCD particles, both in terms of the structure of matter found in nature and their behavior in particle collider experiments.

Hadrons are color-neutral bound states of quarks. Protons and neutrons are examples of hadronic states known as baryons, with the proton consisting of two up quarks and one down quark and the neutron consisting of two down quarks and one up quark. Hadron colliders, like the Large Hadron Collider at CERN, probe physics at small distance scales by colliding protons together at extremely high energy. The physics of a proton-proton collision is extremely complex and first requires understanding the make up of the proton in its initial state.

1.2.1 Parton Distribution Function

The proton is composed of the three primary valence quarks (uud), but also an indefinite number of virtual quarks, commonly referred to as sea quarks. These sea quarks arise through quantum fluctuations where quark-antiquark pairs are created

and annihilated within the proton. When protons collide at high energies, the interactions occur between the individual internal components of the protons. Collectively, these quarks and gluons making up the protons are referred to as partons. The total momentum of the proton is carried by the individual partons. Due to asymptotic freedom, the partons are free to move individually within the proton, with the net momentum of the parton system being that of the proton as a whole. Parton Distribution Functions (PDFs) are used to describe the initial state of the proton by modeling how momentum is distributed between the partons. PDFs are too complex to be calculated purely theoretically and instead must be found experimentally using measurements from deep inelastic scattering experiments.

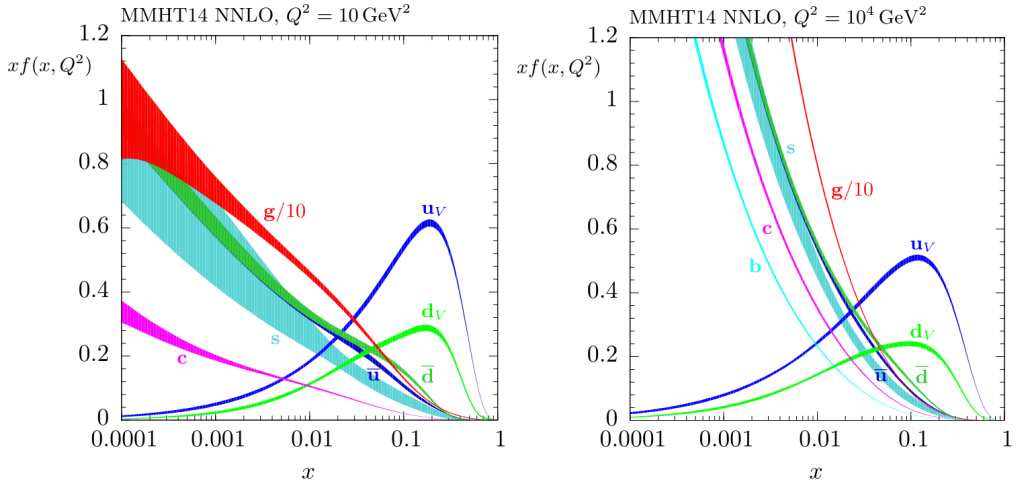

Figure 1.2: The parton distribution functions calculated from analysis of available hard scattering data. Shown here is the longitudinal momentum fraction, x, times the PDF, $f(x, Q)$, as a function of x for momentum transfer scales $Q^2 = 10$ GeV^2 (left) and $Q^2 = 10^4$ GeV^2 (right). PDFs are from the MMHT collaboration [36].

Figure 1.2 shows the fraction of longitudinal momentum, x, times the PDF, $f(x, Q)$, as a function of x for two different momentum scales. As is shown, the probability of a valence quark or gluon carrying a large fraction of the proton momentum is significantly higher than for any other partons, but the valence quarks become less dominant at higher momentum scales.

1.2.2 Showering and Hadronization

During a collision of two high energy protons, the partons of each proton involved in the interaction are given a tremendous amount of energy. This energy is dissipated through the radiation of gluons, which in turn radiate more gluons, creating a parton shower. Eventually, enough energy is dissipated through showering that the parton may no longer be treated as a free particle and must hadronize. Recall that the QCD law of color confinement states that particles carrying color charge cannot propagate freely, and thus any partons resulting from a hard scattering interaction in a proton-proton collision must form new color-neutral hadrons. This process is known as hadronization.

If the parton that initiates showering carries a large amount of energy, the radiated gluons will be sprayed in line with the initial parton. In this case, as the showering and hadronization processes unfold, a largely collimated spray of hadrons, known as a hadronic jet (or simply a jet for short), is created. Jets are extremely important physics objects for analysis as their properties represent those of the original partons that initiated the showering and hadronization processes. Jets at the Large Hadron Collider are a primary focus of the later chapters of this document.

1.3 Beyond Standard Model Physics

Despite the SM representing the most complete and successful theory to date in terms of explaining the particle content of the universe, there are many phenomena that the theory fails to explain. Such Beyond Standard Model (BSM) physics hints that additional particles and interactions must exist that are as of yet unaccounted for in the model. Some of the observed phenomena that serve as evidence of the existence of BSM physics are briefly discussed in this section.

1.3.1 Evidence for Beyond Standard Model Physics

Neutrino Mass

Perhaps the most glaring inaccuracy in the SM is its treatment of the neutrino mass [37]. The SM treats neutrinos as massless particles due to their lack of interaction with the Higgs field. Experimental observations contradict this, as the observation of neutrino flavor oscillation requires that neutrinos have non-zero mass states. Theories exist to add neutrino masses to the SM, however more experimental evidence is required to determine the correct extension of the model.

Matter-Antimatter Asymmetry

The SM accounts for matter and antimatter by giving each fermion an oppositely-charged antiparticle counterpart, which agrees with both theory and experimental observation of particle-antiparticle pair production and annihilation. The problem with this is the observed universe itself. If matter and antimatter existed in equal amounts, they would completely annihilate each other and there would be nothing left. Clearly, this is not the case.

The matter-antimatter asymmetry in the universe, also referred to as baryon asymmetry, implies the existence of several BSM physics processes [45]. In order for the amount of matter to so drastically outweigh the amount of antimatter in the universe, processes that violate charge parity (CP) and baryon number conservation must exist. Such processes so far remain undiscovered.

Dark Matter

Dark matter refers to non-luminous matter that has been indirectly observed through numerous pieces of evidence from astronomy and cosmology. Some of the most compelling observational evidence for the existence of dark matter includes galactic rotation curves and the cosmic microwave background.

Galactic rotation curves plot the velocities of stars orbiting their galactic centers. The results show that the observed rotational speeds are higher than to be expected if the visible matter of the galaxy constituted the entirety of the mass in the system. This implies that a large amount of non-luminous matter must exist beyond the visible galactic disk.

Measurement of the cosmic microwave background, when compared to predictions assuming various amounts of luminous and non-luminous matter, also indicate that a large fraction of mass in the universe is accounted for by dark matter. In fact, measurements of the cosmic microwave background indicate that approximately 25% of the matter in the universe is dark matter, with standard matter accounting for only about 5%. The remaining approximately 70% is accounted for by dark energy.

It is theorized that new BSM particles are required to explain the existence of dark matter. Since such particles have yet to be detected in particle physics experiments and dark matter has so far only been observed to interact with standard

matter through gravitational interactions, dark matter particles are required to be very weakly interacting with standard matter. Many experiments are underway to search for particle dark matter, including at particle colliders. One such search is described in Chapter 5.

1.3.2 Jets as a Potential Discovery Channel at the LHC

The search for new BSM physics at particle collider experiments, like the ATLAS experiment at the Large Hadron Collider, discussed in Chapter 2, includes a huge number of analyses searching for a multitude of different particle signatures in the products of proton-proton collisions. Common search strategies for BSM physics are precision measurements of known SM processes and analyses that probe for anomalous signatures that could represent new physics. The former involves repeated measurement of already confirmed SM processes so that the behavior of the SM may be understood to an extreme level of precision, with the hope that unexpected behavior may emerge in the form of interactions between SM particles and BSM physics through processes so rare that they have so far escaped detection. The latter involves analysis of specific detector signatures and searching for excess numbers of events above SM predictions that could lead to the discovery of a new particle. In each case, hadronic jets are very useful as a potential discovery channel in the search for BSM physics.

Due to their prevalence amongst the collision products, searches involving hadronic jets in particular represent exciting potential for discovery, but also present many technical challenges. Precision measurements of the SM and searches for BSM physics processes that involve very rare decays or weak coupling to SM particles, like dark

matter for example, may benefit from the extremely high rate of collisions that produce high energy hadronic jets. However, with jets being the most common physics objects produced in proton-proton collisions, this large event rate naturally comes with a large background that must be sifted through for the most interesting physics processes.

One specific area where jets act as an exciting potential discovery channel is at the electroweak scale ($\mathcal{O}(100$ GeV$)$). This energy scale is where the most recent particle discoveries have occurred, such as the W and Z bosons and the top quark. While probing higher energies may also lead to discoveries of new physics, it is natural to think that new particles may still reside undetected at the electroweak scale. There are, however, some difficulties in analyzing jet data in this energy range due to experimental considerations related to the high event rate and SM background that restrict the amount of lower-energy jet data that can be collected. These considerations are expanded on further in the later chapters of this document. The discovery potential of this energy range combined with the challenges of data collection there underscore the importance of maximizing the performance of the systems involved in jet detection and measurement.

Analyses involving hadronic jets in the final state require sophisticated jet reconstruction and calibration algorithms, as discussed in Chapter 3, to ensure that the most interesting jet objects are accurately measured. Equally important is a robust trigger system that maximizes discovery power through optimally efficient jet triggers, ensuring that these interesting physics events are successfully recorded. An analysis of the ATLAS jet trigger performance is presented in Chapter 4, where the

performance is analyzed over the course of Run 2 data collection and the effects of evolving run conditions and updated jet calibrations are investigated.

Even with optimally performing jet reconstruction, calibration, and triggering, it is difficult to gain the experimental precision needed to search for the rarest BSM physics processes. This is again due to the extremely high rate of events containing jets, as it is impossible to record all such events and still have bandwidth remaining for all of the other exciting analyses being conducted at the LHC. This issue, and a strategy to mitigate it, is discussed further in Chapter 5, where a creative search for BSM physics using jets at the trigger-level is presented.

Chapter 2: The Large Hadron Collider and ATLAS Experiment

The most important experimental tools in the search for evidence of new physics beyond the Standard Model are powerful particle accelerators capable of colliding particles at very high energies and sophisticated detectors that are able to accurately detect the products of these collisions. In this chapter, two such tools will be described in detail- the Large Hadron Collider [34], currently the world's most powerful particle accelerator, and the ATLAS detector [8], one of the general-purpose detectors integral to the collection of particle collision data.

2.1 The Large Hadron Collider

The Large Hadron Collider (LHC), located at the European Organization for Nuclear Research (CERN) near Geneva, Switzerland, is the highest energy particle collider in the world. The LHC operates by accelerating particle beams through a circular underground tunnel that is 27km in circumference and spans the Swiss-French border. These particle beams are made up of either protons or heavy ions, but the discussion presented here will be focused on proton-proton collisions, as this is the operation that provides the greatest potential for detecting evidence of new physics

and is what the ATLAS detector was designed for. For the duration of Run 2 proton-proton operation from 2015-2018, the energy of each proton beam at the point of collision was 6.5 TeV, corresponding to a center of mass collision energy of $\sqrt{s}$ =13 TeV.

During operation, two particle beams are accelerated through the beampipe in opposite directions where they collide at four predetermined collision points. At each of these collision points, one of four main detectors is installed, as diagrammed in Figure 2.1. These main detectors are ATLAS, CMS, LHCb, and ALICE. ATLAS and CMS serve as multipurpose detectors studying the the products of proton-proton collisions in search of evidence of new physics or making precision measurements of known processes, LHCb specializes in studies of flavor physics, and ALICE is dedicated to heavy ion physics and studying a new state of matter known as quark-gluon plasma.

2.1.1 Beam Injection Chain

In order to accelerate the protons to the extreme energies required to probe for new physics, a multistage beam injection chain consisting of multiple pre-accelerators is utilized. In order of lowest to highest energy, the full accelerator complex includes Linear Accelerator 2 (Linac2) [2], Proton Synchrotron Booster (PSB) [4], Proton Synchrotron (PS) [3], Super Proton Synchrotron (SPS) [5], and finally the LHC itself. A schematic diagram of CERN's accelerator complex is shown in Figure 2.2.

The first stage of the injection chain begins with a humble bottle of hydrogen gas, from which protons are extracted through ionization by an electric field. These protons then enter the first component of the accelerator complex, Linac2, where they

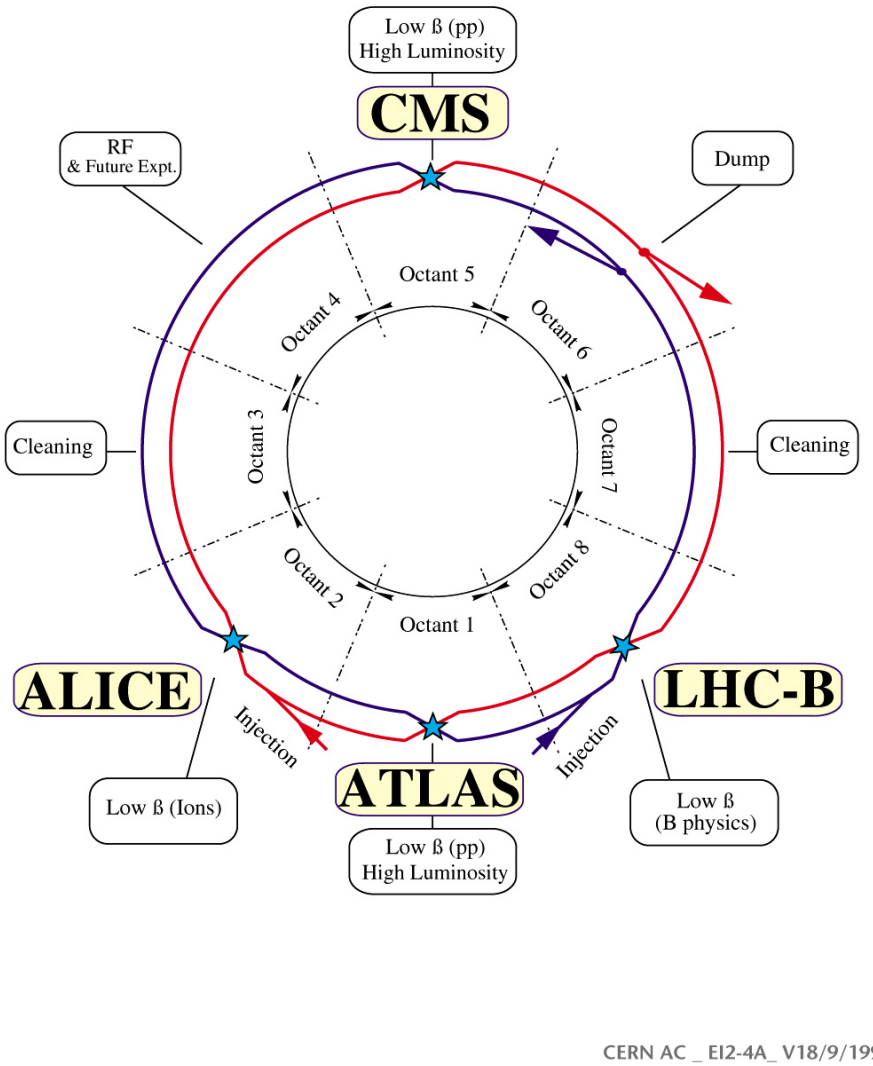

Figure 2.1: Schematic diagram of the LHC ring showing the main detector positioning [16]

are accelerated to an energy of 50 MeV. Beginning operation in 1978 when it replaced Linear Accelerator 1, Linac2 is a 37 m linear accelerator that uses radio frequency

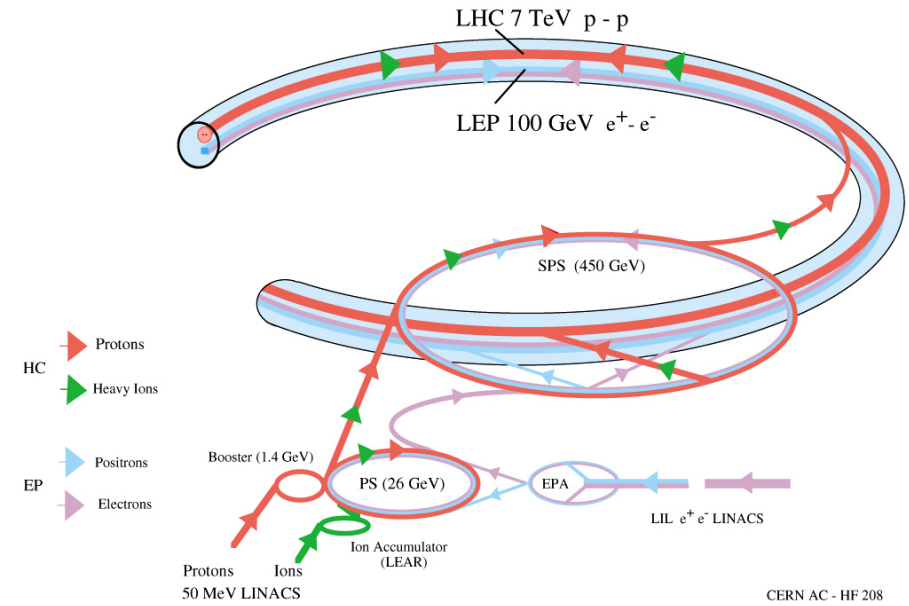

Figure 2.2: Schematic diagram of the LHC accelerator complex [15]

cavities to accelerate protons along its length. Linac2 is set to be replaced by a new linear accelerator, Linac4, as part of the LHC's high-luminosity upgrades prior to Run 3 data collections. Linac4 will be more powerful, increasing proton energy from 50 MeV to 160 MeV.

The next stage of the injection chain is the Proton Synchrotron Booster (PSB). As the name suggests, PSB is a synchrotron accelerator which boosts the proton beam energy from 50 MeV to 1.4 GeV. PSB began operation in 1972. Prior to this, protons entered the next phase of the injection chain, the Proton Synchrotron (PS), straight from the linear accelerator. This greatly limited the number of protons that could be accepted by the PS, leading to the implementation of the PSB in the injection chain.

The PSB allows the PS to accept over 100 times more protons than when they came straight from the linear accelerator.

The third stage of the injection chain, the PS, began operation in 1959 as CERN's first synchrotron and was briefly the world's highest energy particle accelerator. After new accelerators were built at CERN, the PS's role shifted to supplying particles to these new machines. Comprised of a 628 m ring, the PS uses 277 electromagnets to accelerate protons to an energy of 25 GeV.

The final stage of the pre-acceleration process before the protons enter the LHC happens in the Super Proton Synchrotron (SPS), where the proton energy is further increased to 450 GeV by 1317 electromagnets. At 7 km in circumference, the SPS is the second-largest machine in CERN's accelerator complex and provides high energy protons to a number of experiments. In addition to the LHC, the particles accelerated by the SPS are used in experiments such as COMPASS, NA61/SHINE, and NA62. Becoming operational in 1978, the SPS was instrumental to the Nobel Prize-winning discovery of the W and Z bosons in 1983, when it was operating as a proton-antiproton collider.

Finally, the proton beams enter the LHC from the SPS. In the LHC, the protons are accelerated to their maximum Run 2 energy of 6.5 TeV, just short of the machine's design energy of 7 TeV.

2.1.2 Acceleration Mechanisms

The LHC uses a sophisticated system to accelerate protons around the accelerator ring. The most important components are the magnets, which serve to guide the proton beams through the beampipes, and the radiofrequency (RF) cavities, which

accelerate the proton beams to their maximum energy and aid in the formation of bunches.

The LHC ring contains eight arcing segments, each subdivided into 23 subsections that use six superconducting dipole magnets apiece to curve the proton beams through the path set by the beampipes. The dipole magnets, totalling 1104 throughout the entire LHC ring, are designed to guide both proton beams at once as they travel in opposite directions around the ring in separate beampipes. At the design energy of 7 TeV, the dipole magnets are requited to produce a 8.33 T field. To achieve this, the superconducting cables making up the dipole magnets must be cooled to 1.9 K with liquid Helium and a current of 11.85 kA must be applied. In addition to these dipole magnets, many higher-order superconducting magnets are also used, including quadrupole magnets to focus the beams and sextupole, octupole, and decapole magnets that finely correct the beams at the edges of each dipole magnet's reach.

Between each arcing section of the LHC ring is a straight section. Within these eight straight sections are the four interactions points, two collimation systems, a beam dump region, and the RF system. The relative positions of each of these systems may be seen in Figure 2.1. Arguably the most important of these is the RF system, as this is what accelerates the proton beams to the high energy requited to search for evidence of new physics.

The superconducting RF cavities are able to accelerate the proton beams from their injection energy of 450 GeV out of the SPS to the LHC design energy of 7 TeV. This is done using eight RF cavities positioned in series with an oscillating electric field applied in such a way that the direction of the internal electric field alternates in each successive cavity with a frequency of 400 MHz. This causes protons that match

the RF cavity frequency to gain energy as they are accelerated by the electric field. If incoming protons do not match the RF cavity frequency, they will be accelerated or decelerated in such a way that they will form groups called bunches. These bunches are very important as they ensure high luminosity at the collision points.

2.1.3 Bunch Filling and Pileup

The time frame corresponding to the 400 MHz frequency of the RF cavities that each proton bunch occupies is 2.5 ns. This time window is called a bucket. There are approximately 37000 buckets around the LHC ring in total, however only one in every ten buckets is filled with a proton bunch in the standard LHC bunch filling scheme. This corresponds to a 25 ns separation between bunches, resulting in a bunch crossing frequency of 40 MHz. The 25 ns bunch separation is important for minimizing so-called out of time events which can occur when collision products resulting from a preceding bunch crossing are misidentified as part of the collision event being analyzed. There also exists a 3 μs gap in filled buckets in which a beam dump may be toggled. All of this amounts to a maximum of 2808 buckets containing a proton bunch throughout the LHC ring. The number of protons per bunch during nominal LHC operation is designed to be 1.15×10^{11}.

Due to the large number of protons per bunch, there are many proton-proton collisions per bunch crossing. This phenomenon is commonly referred to as pileup. Pileup is an unfortunate byproduct of the high luminosity that is required to increase the LHC's discovery power, as accurately matching collision products to individual proton-proton interactions becomes increasingly difficult as more collisions occur in the same bunch crossing. Thus, the presence of pileup reduces the resolution that

the detector is able to measure the collision products with. The average pileup over all of Run 2 data taking, measured by the average interactions per bunch crossing, $< \mu >$, is shown in Figure 2.3. The average interactions per bunch crossing over all of Run 2 was measured as $< \mu >$=33.7, with pileup increasing between 2015 and 2018 due to increasing luminosity over the course of Run 2. Techniques used to reduce the effects of pileup are discussed in the later chapters of this document, but the effects are never entirely eliminated.

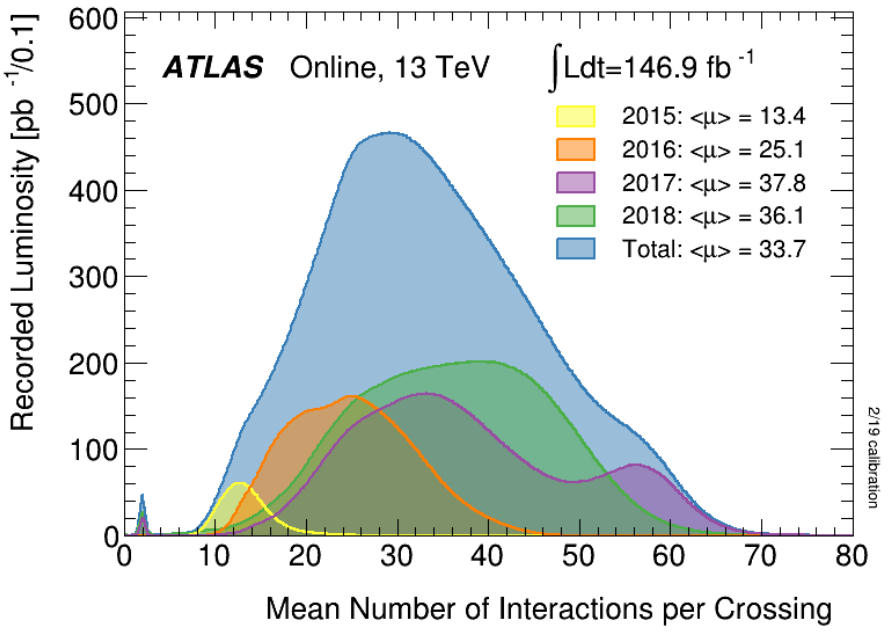

Figure 2.3: Interactions per bunch crossing for proton-proton collision data collected in each year of Run 2 [19]

2.2 The ATLAS Detector

The ATLAS (**A** **T**oroidal **L**HC **A**pparatu**S**) detector is a general-purpose detector situated at one of the LHC interaction points where collisions occur that was used to collect all data discussed in the remaining chapters of this document. A computer-generated image of the ATLAS detector is shown in Figure 2.4. Measuring 25 m in height, 44 m in length, and weighing approximately 7000 tons, the ATLAS detector is a massive machine with many important components. The main components of the ATLAS detector may be broken down into two categories: tracking detectors and calorimeters. The former classification includes the inner detector, made up of pixel detectors, semiconductor trackers, transition radiation trackers, and the muon spectrometer, which, as the outer-most detector element, sets the overall dimensions of the ATLAS detector. The latter includes the electromagnetic calorimeter, the hadronic calorimeter, and the forward/backward calorimeters. These detectors, as well as the ATLAS magnetic and trigger systems, are described in detail in this section. An overview of the ATLAS coordinate system is also presented.

2.2.1 Coordinate System

A right-handed coordinate system is used throughout ATLAS, with the origin defined as the interaction point where the particle collisions occur. The positive x-direction points from the origin towards the center of the LHC ring, the positive y-axis points towards the earth's surface, and the z-axis points along the beamline. The x-y plane is referred to as the transverse plane, while the z-direction represents

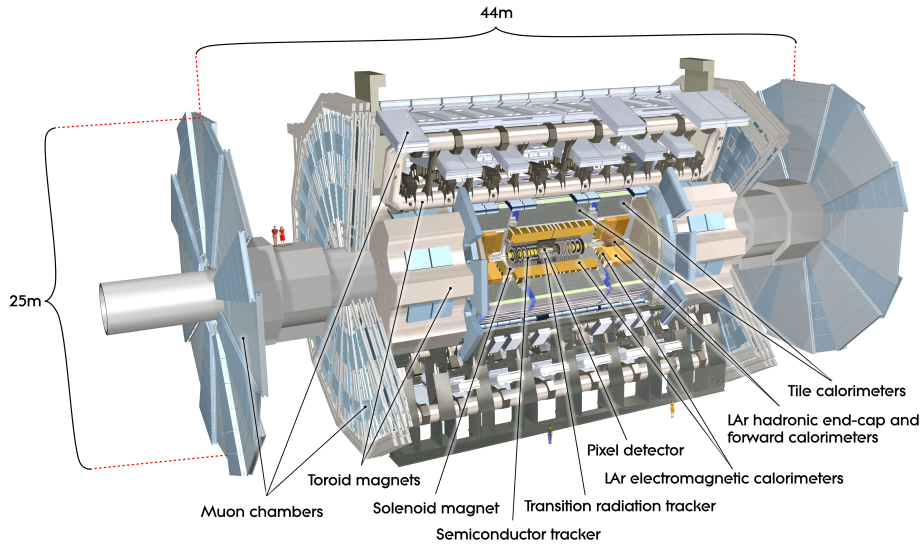

Figure 2.4: A computer-generated schematic diagram of the full ATLAS detector [43]

the longitudinal direction. Quantities such as transverse energy and transverse momentum, which will be used extensively in the coming chapters, are given as E_T and p_T, respectively. These refer to the energy and momentum of a collision product in the transverse direction. A spherical polar coordinate system is also commonly used. In these coordinates, the polar angle θ is measured from the positive z-axis, the azimuthal angle ϕ is measured from the positive x-axis, and the radial coordinate $r = \sqrt{x^2 + y^2}$ measures distance from the beamline. A helpful diagram of these coordinates can be seen in Figure 2.5.

The pseudorapidity, denoted as η, is a useful quantity in particle physics defined as $\eta = -\ln[\tan(\theta/2)]$. Pseudorapidity is often used in place of θ because differences in pseudorapidity are invariant under boosts in the z-direction. The initial z-direction momentum of colliding partons varies and is not precisely known, meaning that the

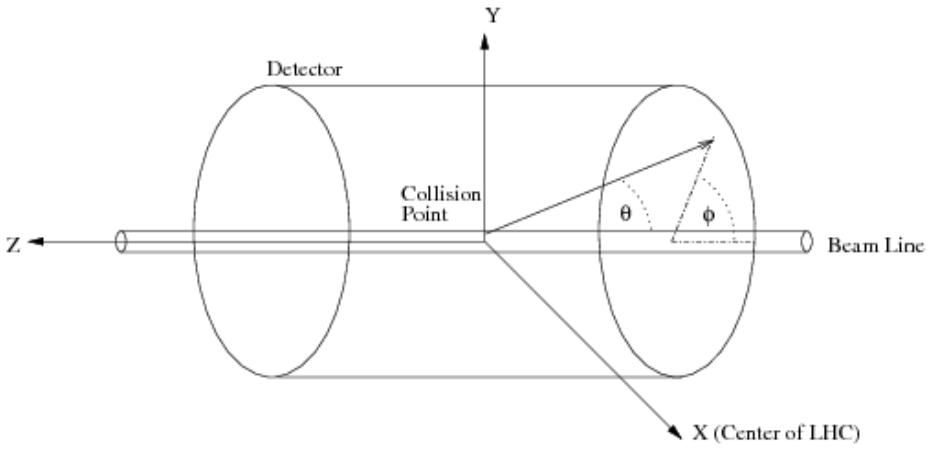

Figure 2.5: A sketch of the ATLAS coordinate System [46]

center of mass frames of individual parton-parton collision events have different boosts in the z-direction relative to the lab frame. Thus, the use of a quantity invariant under boosts in the z-direction is quite convenient. Written in terms of pseudorapidity, the distance between two points in the η-ϕ plane is given by $\Delta R = \sqrt{\eta^2 + \phi^2}$. This quantity is also invariant under boosts in the z-direction and is used frequently when describing the separation between products of a particle collision. An in-depth discussion of relativistic kinematics can be found in Ref [48].

2.2.2 Inner Detector

The first component of the ATLAS detector that particles encounter after they are produced in collisions at the interaction point is the Inner Detector, which houses tracking detectors used to follow the trajectories of charged particles. The closest layer of the Inner Detector was located just 33 mm from the interaction point during Run 2. This close proximity to the interaction point has two major consequences-

the detectors in this region must reliably perform under extreme radiation levels and have very fine granularity needed to overcome a very large track density to achieve the desired momentum and vertex resolution. This is accomplished through the combined use of silicon pixel detectors, silicon microstrip detectors (referred to as the semiconductor tracker, or SCT), and the transition radiation tracker (TRT). The silicon detectors track the position of charged particles by measuring charge collected after an electron-hole pair is formed by energy deposited in the detectors as charged particles pass through the active detector area. The TRT measures transition radiation emitted as particles cross interfaces between areas of different indices of refraction. The elements of the Inner Detector span a pseudorapidity range of $|\eta| < 2.5$. A diagram showing the layout of the inner detector is presented in Figure 2.6, with a more detailed view of each layer shown in Figure 2.7.

In the barrel region, the tracking detectors are arranged in concentric cylinders around the beam axis and in the end-cap regions they are on disks aligned perpendicular to the beam axis. The pixel detectors are located closest to the interaction point and provide the highest detector granularity, with each pixel measuring $50 \times 400 \mu\text{m}^2$. Particles typically pass through three pixel layers as they traverse the Inner Detector.

In the time between LHC Run 1 and LHC Run 2, an addition to the inner detector was made in the form of a new layer of pixel detectors in the barrel region. This upgrade, called the Insertable B-Layer (IBL)[14], was made to cope with the potential loss in track reconstruction caused by irreversible damage to the existing pixels due to prolonged exposure to high amounts of radiation. The installation of the IBL decreased the inner radius of the Inner Detector's barrel region from 50 mm to approximately 33 mm. The pixels in this layer measure $50 \times 250 \mu\text{m}^2$. The closer

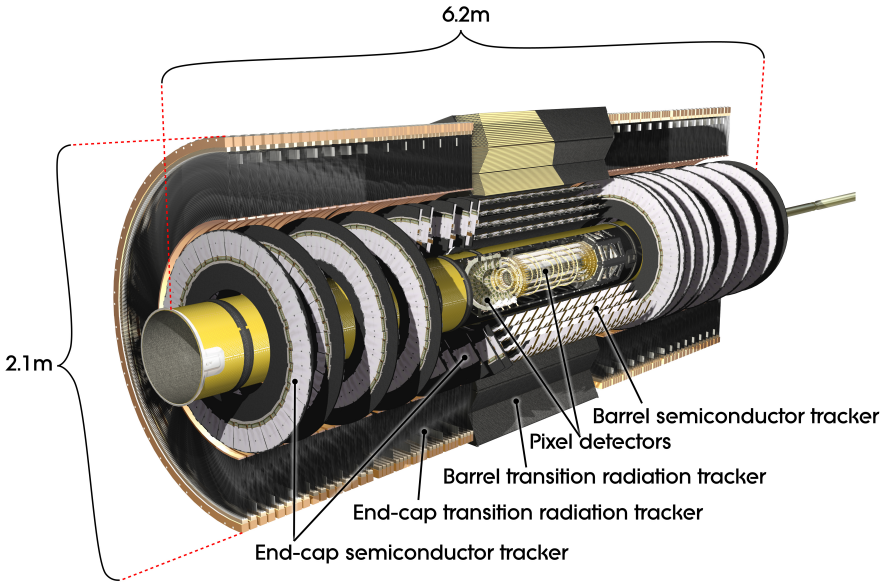

Figure 2.6: A computer-generated schematic diagram of the ATLAS inner detector [41]

proximity to the interaction point and improved pixel resolution allows for improved vertex reconstruction to help mitigate the effects of pileup.

The next closest tracking detectors to the interaction point are the SCT layers, extending the radius of the Inner Detector from 123 mm at the edge of the pixel layers to 514 mm from the interaction point. The SCT can be thought of as a larger version of the pixel detectors, using the same particle detection techniques with larger silicon microstrip detectors instead of pixels. Each individual silicon microstrip measures $126 \times 80 \mu\text{m}^2$. A typical particle travels through four layers of SCTs in the barrel region.

The final layer of the inner detector is the TRT, further extending the radius of the Inner Detector to 1082 mm. The TRT provides a large number of tracking points-

36 for the typical track- however the resolution is not as fine as the other components of the Inner Detector. Unlike the pixel and SCT detectors, the TRT is a gaseous ionization detector. Rather than utilize silicon detectors, the TDT employs an array of cathode tubes, called straws, that are filled with Xenon gas and contain an anode wire running through the center. When a charged particle transitions from one detector medium to another, transition radiation inversely proportional to the particle's mass is emitted. This transition radiation induces a signal within the straws that is read out by the anode wires. Due to the mass dependence of the amount of transition radiation produced, the TRT aids in particle identification as lighter particles, like electrons, will induce a larger signal than heavier particles like muons or charged pions.

2.2.3 Calorimeters

Energy measurements of particles passing through the ATLAS detector are primarily made by the calorimeter system, which is designed to fully absorb the incident particles. This is complimentary to the tracking detectors in the Inner Detector, which optimally measure the energy of charged particles with low enough transverse momentum such that their tracks are sufficiently deflected when passing through the tracker layers. Fully absorbing and measuring the energy of incident particles requires a sophisticated and well-understood calorimeter system with a large volume located in the central region of the detector, between the inner detector trackers and the outer muon spectrometer system. ATLAS uses sampling calorimeters [35] made up of alternating layers of active material and dense absorber material. Sampling calorimeters

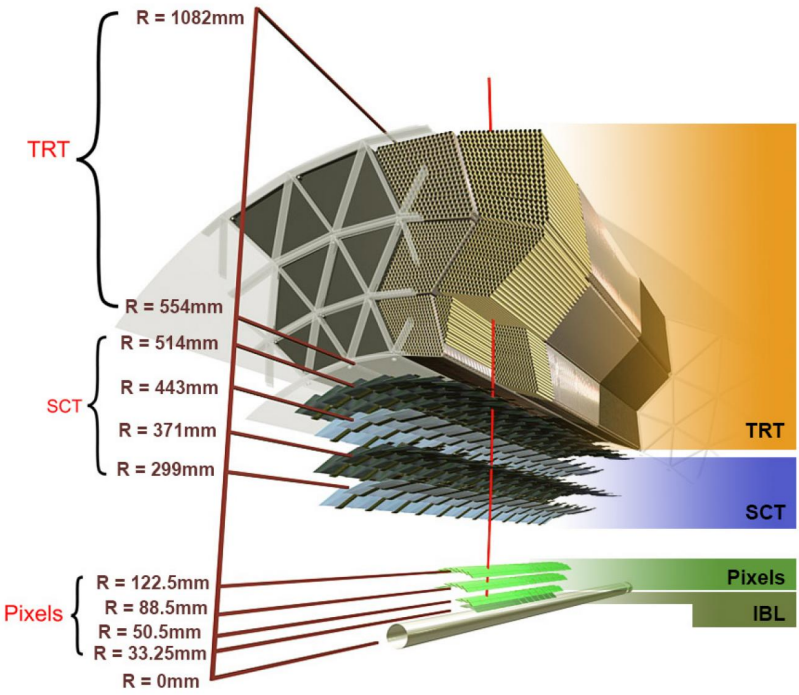

Figure 2.7: A computer-generated image showing a detailed view of the layers of the ATLAS inner detector [9]

are designed to induce showers through the incident particle's interactions with the detector medium. The energy of the secondary particles in these showers is measured in the active detector layers and the incident particle energy is reconstructed.

The ATLAS calorimeters are split into two categories: electromagnetic calorimeters and hadronic calorimeters. The former, making up the inner layers of the calorimeters, uses liquid argon (LAr) calorimeters and is optimized for the detection of signals induced by electrons and photons while the latter, making up the outer layers, employs tile calorimeters and is designed to measure the particle jets created by hadrons interacting with the detector medium. It should be noted that

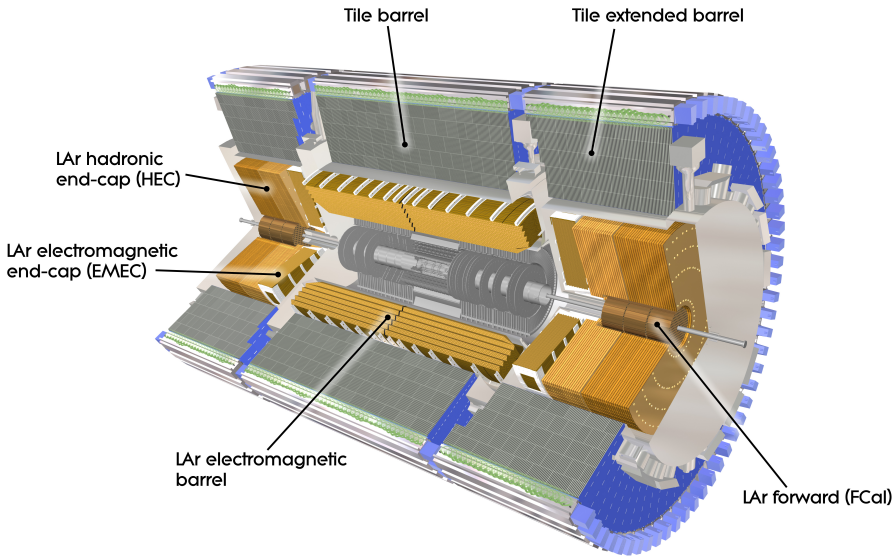

Figure 2.8: A computer-generated image showing the full ATLAS calorimeter system with each component labeled [40]

the EM calorimeter is not expected to fully absorb the energy of all incident EM particles, as those with sufficiently high energies will continue through to the hadronic calorimeter layers. However, because EM showers are faster developing than their hadronic counterparts, it is expected that most energy deposited in the inner layers of the calorimeters will be from EM particles and most energy deposited in the outer layers will be from hadronic particles. A diagram showing the various components of the ATLAS calorimeter system is shown in Figure 2.8.

The calorimetry system in ATLAS must meet several design requirements. On the technical side, the calorimeters must have a fast response time to minimize the effects of pileup and low amounts of detector noise to avoid producing fake signals. The calorimeters must also be radiation hard due to the high particle flux they must endure

and fit the geometric constraints necessary to have full coverage in the azimuthal direction and up to $|\eta| = 4.9$ (approximately 1° from the beam pipe). In terms of physics capabilities, the calorimeters are required to provide energy measurements of particles spanning a range of MeV to TeV, as well as spatial resolution necessary to identify particles by their shower profile. In this section, an overview of the the main components of the ATLAS calorimeter system is presented. A detailed discussion of reconstruction and calibration of hadronic jets in the calorimeter may be seen in Chapter 3.

Electromagnetic Calorimeter

The electromagnetic (EM) calorimeter measures energy deposited in the detector medium by incident charged particles and photons. The two main processes that govern energy deposition in the EM calorimeter from a high-energy charged particle are bremsstrahlung and ionization [35]. Bremsstrahlung refers to the process of a charged particle emitting photons as it is decelerated through interactions with a dense medium. Incident charged particles may also lose energy through collisions with atoms in the medium, which results in ionization. Bremsstrahlung dominates at high incident particle energies (greater than about 10 MeV), while ionization is more significant at lower energy. High energy photons tend to deposit energy in the calorimeters through electron-positron pair-production. The electrons and positrons resulting from pair-production then emit more photons through bremstrahlung, which may undergo pair-production processes themselves, thus resulting in an electromagnetic shower in the calorimeter. These EM showers, also refered to as EM jets, are

collimated cascades of electrons, positrons, and photons propagating through the detector. The properties of these EM showers are used to identify the incident particle and reconstruct its energy, as discussed further in Chapter 3.

The EM calorimeter is located closest to the interaction point and is divided into a barrel portion and two end-caps. The barrel portion, covering $|\eta| < 1.475$, has a total thickness of approximately 22 radiation lengths (X_0) while the end-cap components span $1.375 < |\eta| < 3.2$ and have a thickness of roughly $24X_0$. Radiation length is a quantity defined as the average distance that an electron must travel in a medium to lose $\frac{1}{e}$ of its original energy. For the materials making up the EM calorimeter, the radiation length is approximately 1.8 cm. The ATLAS EM calorimeter is made up of active layers of liquid argon alternating with lead absorber layers. Incident particles induce showers when interacting with the lead absorber material and the liquid argon serves as the active medium where ionization electrons are collected on electrodes to be read out as signal. The absorber plates and electrodes that read out the signal from the active layers are designed with an accordion geometry that serves a dual purpose of allowing for faster readings and providing full azimuthal coverage by eliminating dead zones caused by cracks between electrodes.

Sampling calorimeters like those used throughout the ATLAS calorimeter system are easily segmented in the latitudinal and longitudinal directions, which provides spacial resolution and thus improved particle identification capabilities. In the $|\eta| < 2.5$ region (consisting of the barrel and a portion of the end-cap regions) where high transverse momentum physics objects of interest are detected, the EM calorimeter is segmented into three sections, as shown in Figure 2.9. Working from the interaction point outward, the first section is intended to provide very fine resolution for the

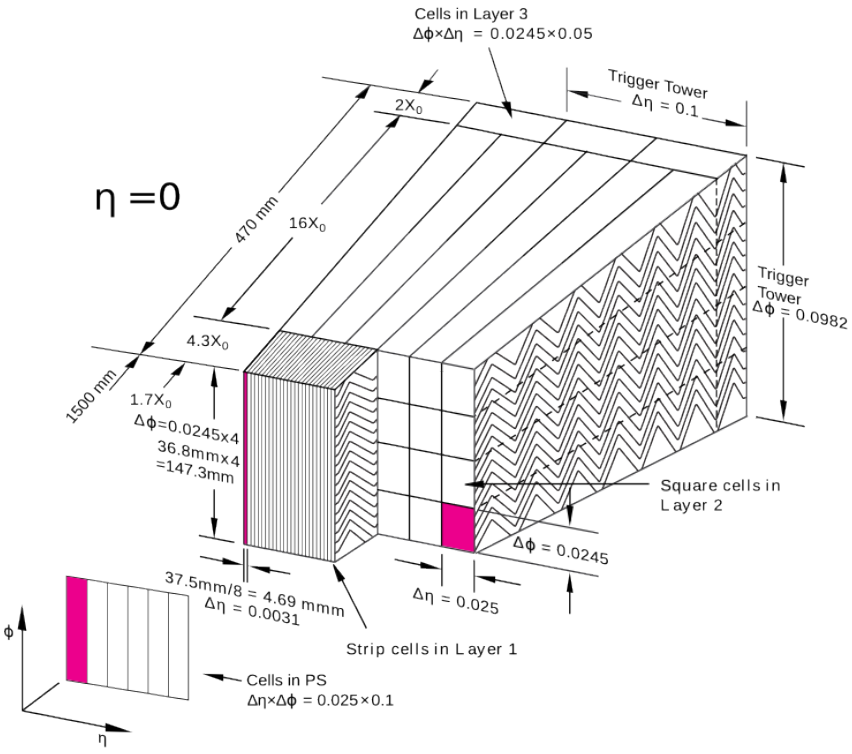

Figure 2.9: A schematic diagram depicting a portion of the ATLAS EM calorimeter in the barrel region [47]

purpose of distinguishing signals from photons versus neutral pions based on the shower profile, the next section is designed to fully contain EM showers with energies less than approximately 50 GeV, and the final section is designed to only be reached by high-energy electrons and is used for triggering. The inner portion of the end-cap EM calorimeter is segmented into two sections depth-wise and is not as finely segmented laterally.

Hadronic Calorimeter

Hadronic jets are similar to the EM jets introduced in the previous section in that they are produced through a series of interactions in the calorimeter, with the main

difference being that these interactions are largely moderated by the strong force. Energy is deposited in the calorimeters by the incident hadrons through two types of effects- the production of secondary hadrons and hadronic collisions with nuclei in the calorimeter material. The secondary hadrons that are produced, such as charged and neutral pions, typically carry energies on the GeV scale. Hadronic interactions with nuclei in the detector material results in particles with energy on the order of the MeV scale through processes like spallation, neutron capture, and nuclear recoil [35]. Due to the presence of neutral pions, hadronic jets have an electromagnetic component. As these neutral pions decay into two photons, which go on to interact with the detector electromagnetically through the bremsstrahlung and pair-production proceses discussed in the previous section, there is a significant portion of the incident hadron's energy deposited in the calorimeters through EM interactions. There is also a component of so called "invisible energy" present in hadronic jets [44]. This energy is largely due to the binding energy of nucleons and is not detectable in the hadronic calorimeter. This invisible energy contributes negatively to the energy resolution of hadronic jets, which will be discussed further in Chapter 3.

The hadronic calorimeter system, located immediately outside of the EM calorimeter, is comprised of the tile and end-cap hadronic calorimeters. The tile calorimeter covers a total range of $|\eta| < 1.7$ and consists of a barrel and two extended barrel regions. A diagram of the full tile calorimeter system is shown in Figure 2.10. The end-cap hadronic calorimeters cover the range $1.5 < |\eta| < 3.2$. The tile calorimeter's absorber and active materials are steel and plastic scintillator, respectively. The hadronic end-cap calorimeter's absorber and active materials are copper and liquid argon. Liquid argon was chosen as the active material for the calorimeters in this

region due to its radiation hardness, as the forward region of the detector endures the highest flux of incident particles.

In order to obtain spatial resolution, the hadronic calorimeter is segmented into modules. In each module of the tile calorimeter, the energy deposited in the scintillators by ionizing particles is converted to light and read out by photomultiplier tubes (PMTs) via an optical fiber. A detailed sketch of an individual tile module may be seen in Figure 2.10.

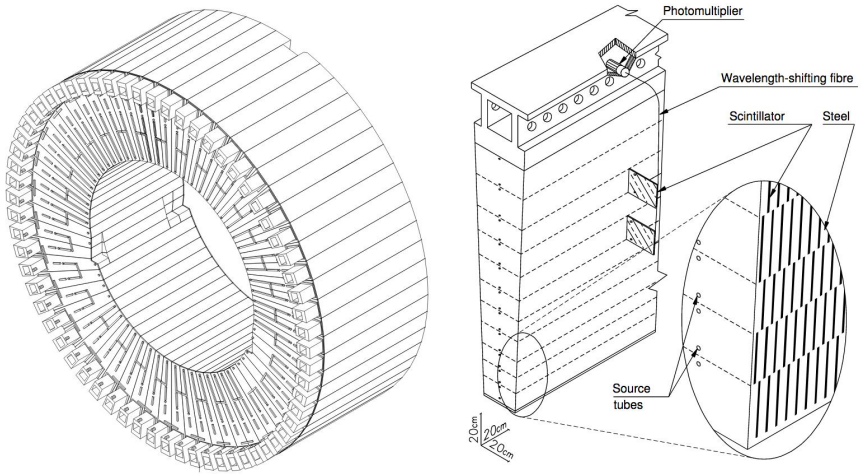

Figure 2.10: A schematic diagram depicting the full ATLAS hadronic tile calorimeter (left) and a detailed view of an individual tile module (right) [8]

Similar to the EM calorimeter, the central barrel of the hadronic tile calorimeter is sectioned into three segments of different depths. In terms of hadronic interaction length λ, the segments have thicknesses of 1.5λ, 4.1λ, and 1.8λ at $\eta = 0$, measured from the innermost to outermost segments. Hadronic interaction length is defined

as the length required to reduce the number of relativistic hadrons in a shower by a factor of $\frac{1}{e}$. Figure 2.11 shows a schematic diagram of the relative configuration of tile calorimeter layers in the barrel and extended barrel regions. The endcap regions are segmented as well, and utilize readout electrodes in the liquid argon active layers to measure ionized charge rather than PMTs. The thickness of the hadronic endcap calorimeters is approximately 12λ.

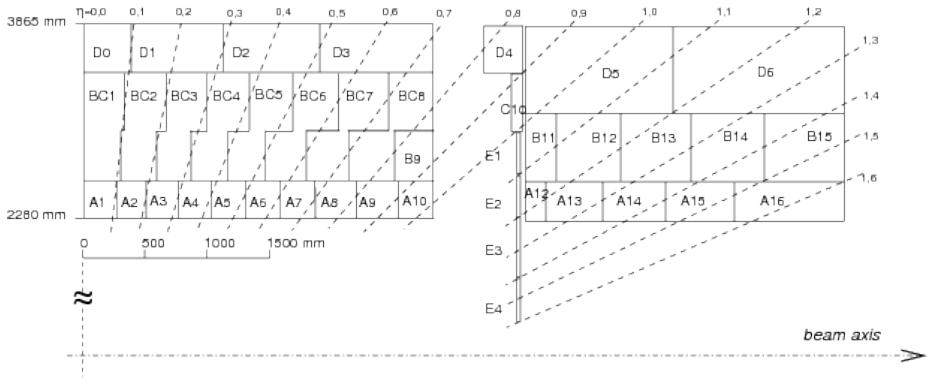

Figure 2.11: A schematic diagram depicting a cross-sectional view of the ATLAS hadronic tile calorimeter with tiles labeled [28]

The segmentation of the hadronic calorimeter is not as fine as that of the EM calorimeter. Cells in the EM calorimeter range from $\Delta\eta$x$\Delta\phi = 0.003$x0.1 to $\Delta\eta$x$\Delta\phi =$ 0.025x0.025 versus $\Delta\eta$x$\Delta\phi = 0.1$x0.1 in the hadronic calorimeter. This is by design, as hadronic-induced jets typically have a wider shower profile than EM showers.

Forward Calorimeter

The final component of the ATLAS calorimeter system is the forward calorimeter (FCal). The FCal spans a range of $3.1 < |\eta| < 4.9$. The FCal aids in achieving as close to full calorimeter coverage in $|\eta|$ as possible and reduces background radiation that makes it beyond the calorimeter system to the muon spectrometer. Due to the large amount low transverse momentum particles produced in the proton-proton collisions, the particle flux in the forward region is very high. To reduce the radiation levels at the front face of the FCal, it is recessed by 1.2 m from the front face of the surrounding EM end-cap calorimeter, putting constraints on the depth of the FCal and necessitating that it have a higher density design than the other calorimeters. Like the rest of the calorimeter system, the FCal consists of an inner layer designed for electromagnetic calorimetry and an outer layer intended for hadronic calorimetry. The active material in both layers is liquid argon. Copper plates are used as the absorbing material in the inner layer while tungsten plates are used in the outer layer. All told, the total depth of the FCal is approximately 10 interaction lengths.

2.2.4 Muon Spectrometer

The outer-most portion of the ATLAS detector is the muon spectrometer (MS). At the energy scale of the LHC, muons produced in proton-proton collisions are expected to primarily be minimally ionizing particles. This means that the energy losses of muons as they pass through the detector medium are minimal. However, it should be noted that energy loss of particles passing through material is dependent on the energy of the incident particle, as seen in the plot of stopping power versus muon momentum presented in Figure 2.12. Sufficiently energetic muons would deposit

significant amounts of energy in the calorimeters, but because this is quite rare, the vast majority of muons must be measured outside of the calorimeters in the MS.

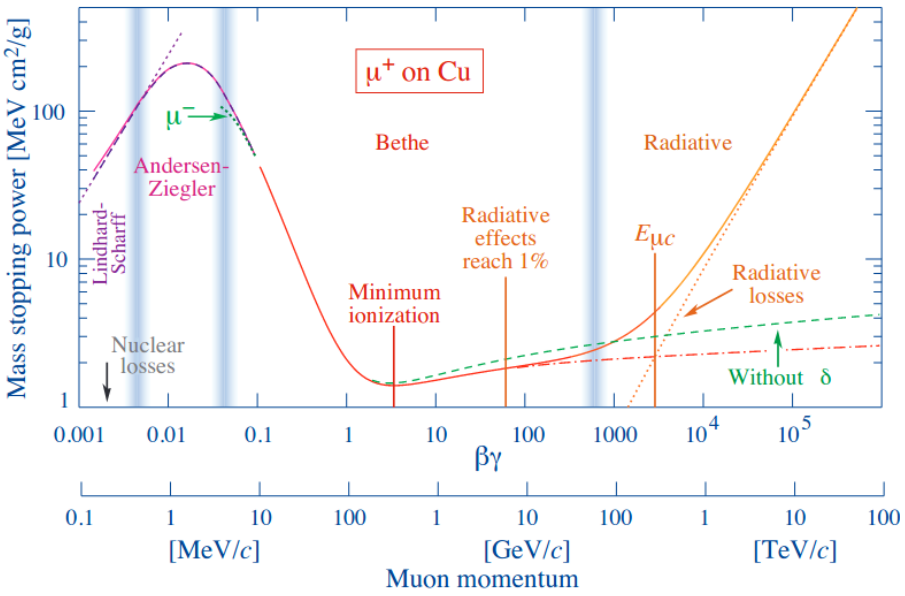

Figure 2.12: A plot of stopping power for muons passing through copper as a function of muon momentum [48]

Muons are not expected to deposit amounts of energy in the calorimeters significant enough to be stopped and thus are expected to pass all the way through the ATLAS detector. For this reason, the hardware devoted to tracking muons is situated in the outer layer of ATLAS. This design conveniently minimizes the number of other particles that will make it through the calorimeters to the muon spectrometer, as neutrinos are the only other type of particle expected to regularly pass through the full detector volume. Neutrinos do not leave tracks and it is considered negligibly rare that they leave a signal in any part of the detector.

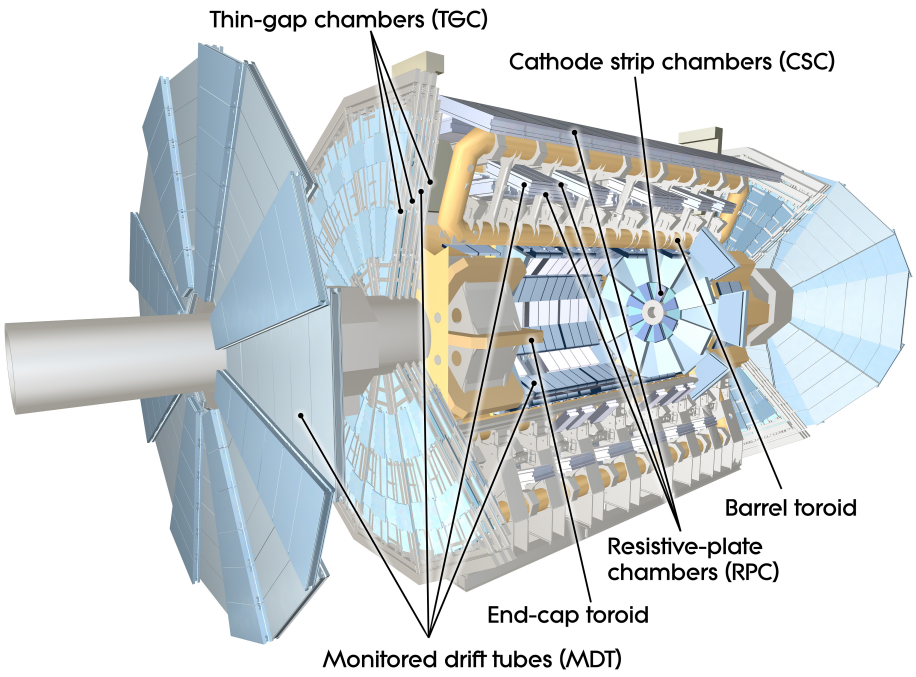

Figure 2.13: A computer-generated image showing the full ATLAS Muon Spectrometer [42]

The MS is made up of several types of gaseous tracking detectors arranged in a cylindrical geometry in the barrel region and as disks perpendicular to the beamline in the endcap region. The full MS is shown in Figure 2.13 and a detailed cross-sectional view is presented in Figure 2.14. The MS is designed such that a typical muon is expected to pass through three layers of tracking detectors. The momentum of charged particles passing through these layers is measured based on the deflection of their reconstructed tracks in the torroidal magnetic field of ATLAS.

Multiple technologies are utilized in the MS to provide tracking measurements in the different regions of the ATLAS detector. In the barrel region of the detector ($|\eta| < 2.0$), Monitored Drift Tubes (MDTs) are used to measure muon tracks. MDTs are

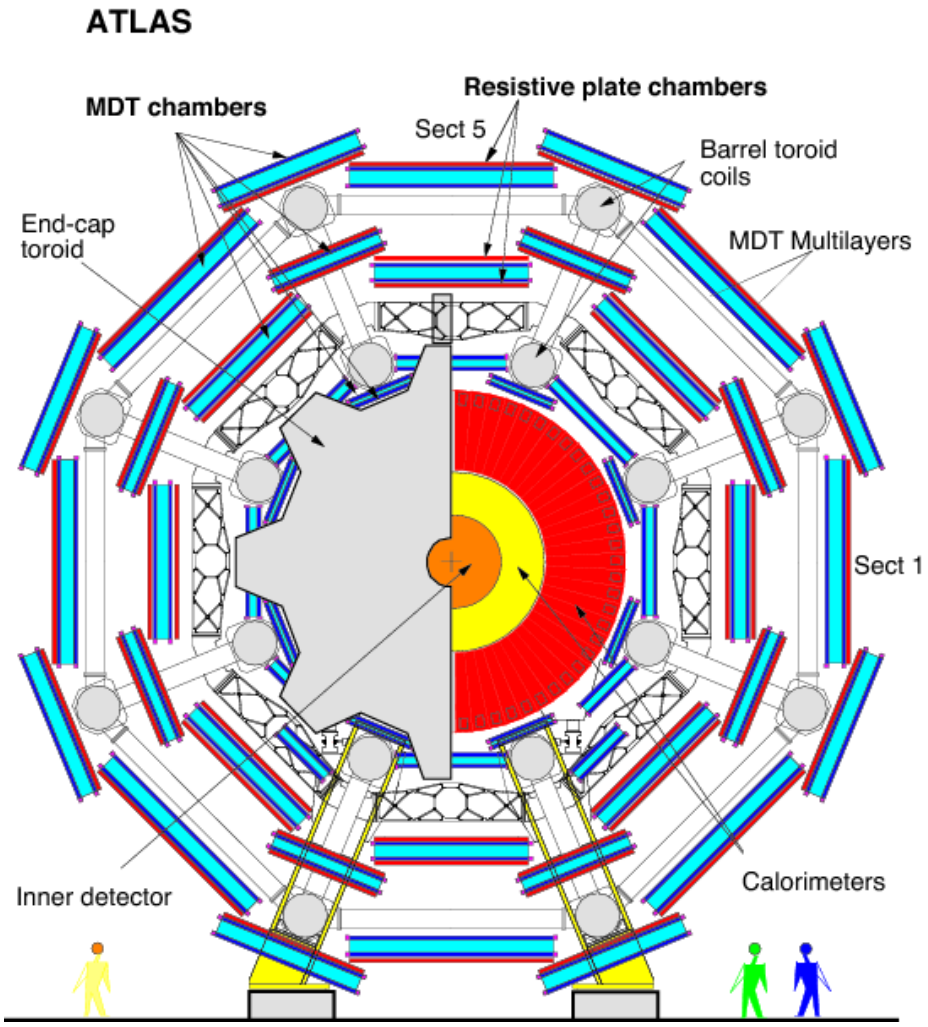

Figure 2.14: A schematic diagram showing a cross-sectional view of the ATLAS Muon Spectrometer in the barrel region [21]

composed of gas-filled tubes with anode wires running down the center. When a muon passes through the tube, the gas is ionized and the ionization electrons are collected by the anode, creating a signal. In the end-cap region ($2.0 < |\eta| < 2.7$), two layers of MDTs are used with the layer between them utilizing Cathode Strip Chambers (CSCs). CSCs are employed here for their higher granularity, which is necessary due

to the high particle flux in this region. The CSCs are wire chambers comprised of cathode strips arranged perpendicular to anode wires. A position measurement is obtained by measuring the charge induced on the cathode by an avalanche signal in the anode wire.

In addition to tracking, a muon trigger that uses separate hardware is also present in the MS. The muon trigger system uses Resistive Plate Chambers (RPCs) and Thin Gap Chambers (TGCs) to obtain rapid measurements of signals from passing muons. The RPCs cover the $|\eta| < 1.05$ region and the TGCs cover $|\eta| > 1.05$. The RPCs are comprised of two parallel metal plates held at opposite voltages with a thin layer of gas between them. When a muon passes through an RPC, the gas is ionized and the ionization electrons collect on one of the metal plates from which the signal is read out. The TGCs use very similar technology, with the difference being the addition of anode wires between the two metal plates.

2.2.5 Magnetic System

A well-understood magnetic field permeating the detector volume is necessary for tracking charged particles and measuring their momentum as they pass through the ATLAS tracking detectors. The magnetic field present throughout the detector is a result of three superconducting magnet subsystems: a central solenoid, a barrel toroid, and two end-cap toroids. A schematic diagram of the ATLAS magnetic system is shown in Figure 2.15.

The central 2 T solenoidal magnetic field aids in charged particle identification and momentum measurements in the inner tracker. The axis of the solenoid providing this magnetic field lines up with the beam axis. The axial length of the solenoid is

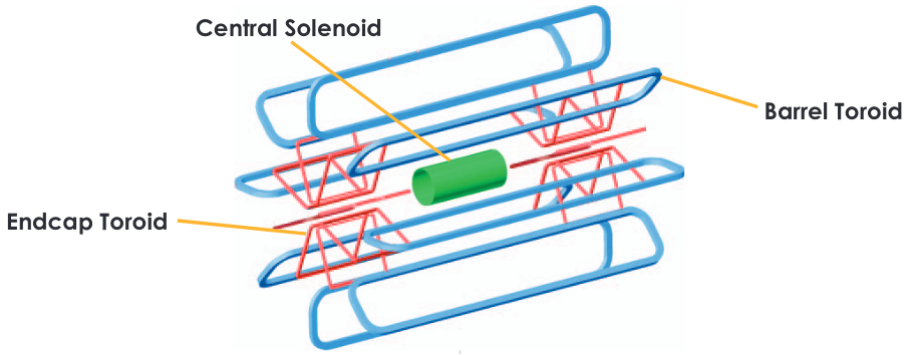

Figure 2.15: Schematic diagram of the ATLAS magnetic system [39]

5.3 m and its diameter is 2.5 m. A solenoidal field is preferable in this region, as a strong, regular magnetic field is necessary to achieve precise measurements of charged particles passing through the high-granularity tracking detectors located nearest to the interaction point.

As its name suggests, ATLAS employs toroidal magnets in the barrel and end-cap regions to generate magnetic fields throughout the volume occupied by the muon spectrometer. The toroidal magnetic field in this region is directed perpendicular to the trajectory of particles that pass through the inner detector and calorimeters. The use of torroidal magnets in the outer regions of ATLAS was largely motivated by size and cost constraints, as the commissioning of a large enough solenoidal magnet would not have been possible.

2.2.6 Trigger System

The trigger system [25] plays a very important role in the ATLAS experiment through managing the recorded event rate while ensuring that the most important physics events are saved for future analysis. Because it is impossible to save the

detector signals from every collision event at the design bunch crossing frequency of 40 MHz, the trigger system identifies potentially interesting events and directs that the detector signals for these events be saved to disk. This is accomplished with a two-level trigger system consisting of the Level-1 (L1) hardware trigger followed by the software-based High Level Trigger (HLT). All told, the ATLAS trigger system reduces the final event rate down to approximately 1 kHz.

The L1 trigger first reduces the initial event rate down to approximately 100 kHz, with a decision time of 2.5 μs. The L1 trigger uses information from the calorimeters and muon spectometer to identify events containing high momentum physics objects and define regions-of-interest (RoIs). ROIs identify where in the detector, measured in η and ϕ, interesting physics is taking place. Information from the L1 trigger is then passed to the HLT which then uses data from all detector components in the RoIs to further process events.

The HLT further reduces the L1 output event rate to about 1 kHz, taking roughly 200 ms. At the HLT level, physics objects are reconstructed from the RoIs and HLT trigger decisions are made based on the kinematic properties of these objects. Analyses may set trigger requirements on L1 and HLT criteria like type and number of physics objects, minimum momentum magnitude, specific η range, etc. in the trigger menu. Figure 2.16 and Figure 2.17 show a typical selection of example L1 trigger and HLT rates for the various ATLAS physics groups, respectively.

Not all triggers are able to be saved at their full rate due to trigger bandwidth and storage limitations, especially those which trigger on a low p_T threshold. In order to control the rate of such triggers to keep them within the trigger bandwidth allocated to them, they are often prescaled. A prescaled trigger is assigned a prescale factor,

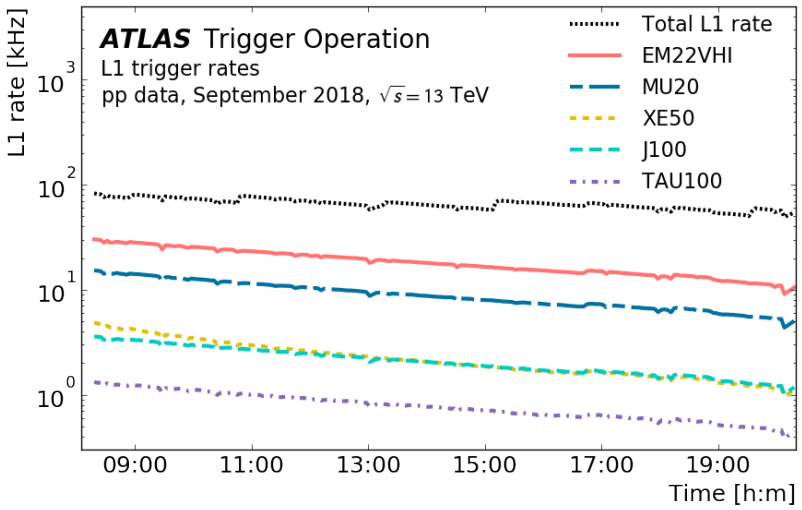

Figure 2.16: Example L1 physics trigger rates from a typical run. Trigger rates shown are based on physics objects like electromagnetic clusters (EM), muon candidates (MU), jet candidates (J), missing transverse energy (XE) and tau candidates (TAU) [20]

N_{ps}, meaning that only one out of every N_{ps} events passing the trigger will be saved. This allows for trigger bandwidth to be limited for triggers that account for more well-observed physics processes and instead allocated to infrequently firing triggers. Prescaling does however contribute to a lessening of sensitivity to low-p_T processes due to a loss of statistical precision in this regime. The negative effects of prescaling make an optimized physics object reconstruction and calibration scheme all the more important, as will be discussed in detail for the case of jet objects in Chapter 4.

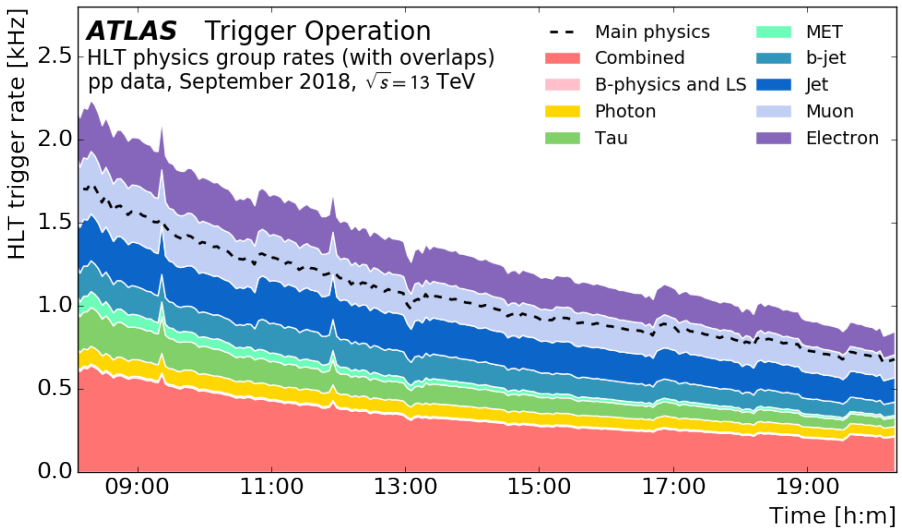

Figure 2.17: Example HLT physics trigger rates from a typical run for each physics group. [20]

Chapter 3: Jet Physics in ATLAS

According to the theory of QCD and color confinement, quarks are never found in isolation. Nevertheless, they still leave a unique, detectable signature in the form of a collimated spray of particles, known as a jet. Not only are jets central to the analyses presented later in this document, but accurate measurement, reconstruction, and calibration of these jet objects in the ATLAS detector is of great importance to maximizing the impact of the data collected in the hunt for new physics at the LHC.

This chapter focuses on experimental measurement techniques applied to hadronic jets in the ATLAS detector. A detailed overview of the signatures of jets in the detector, jet reconstruction algorithms, and the jet calibration sequence is presented.

3.1 Jet Reconstruction

In the proton-proton collisions at the LHC, tremendous numbers of high energy particles are produced, leading to a barrage of activity in the ATLAS calorimeters. While the signals picked up in the calorimeters are often induced by high energy quarks (and therefore jets), they must be differentiated from other particles like electrons, photons, and muons that also deposit energy in the calorimeter layers. There is also the issue of differentiating the signal coming from the primary hard-scattering event from those due to pileup that further clutters the detector environment. For

these reasons, it is important to have well-defined processes to pick out jet objects based on their detector signatures and sophisticated algorithms to reconstruct those signals into physics objects to be used for analysis.

3.1.1 Detector Signatures

It is helpful, both in terms of computation time and jet energy resolution, to identify interesting detector regions or physics objects to pass to the jet reconstruction algorithms. Traditionally, jet object definitions have been based primarily on calorimeter information, but some reconstruction algorithms also take track information into account.

Topological Clusters

The primary detector signal indicating that a jet has been produced in a collision event and interacted with the detector is the so-called topocluster [11], referring to topologically connected calorimeter cells that detect a signal above a set energy threshold in the same collision event. As discussed earlier, the ATLAS calorimeters are finely segmented, allowing for the formation of topoclusters using only the calorimeter cells where the incident jet has deposited energy. The formation of topoclusters allows for regions of high energy density to be isolated, which helps to suppress background fluctuations due to pileup and calorimeter noise. The observable governing the formation of topoclusters is cell signal significance, S_{cell}, as given in Equation 3.1. Cell signal significance is defined as the ratio of cell signal, E_{cell}, to the average expected noise, σ_{noise}, as estimated for each run year.

$$S_{cell} = \frac{E_{cell}}{\sigma_{noise}} \tag{3.1}$$

Topoclusters are seeded by cells with a highly significant seed signal and grow in three dimensions through the inclusion of neighboring cells based on a growing-volume algorithm. This clustering algorithm grows the clusters by adding neighboring cells that satisfy progressively lessened cell signal significance criteria. In this case, "neighboring cells" refers to adjacent calorimeter cells in the same layer, or cells in adjacent layers having at least partial overlap in the $\eta - \phi$ plane. The topocluster formation scheme used by ATLAS has three steps- seeding, growth, and boundary cell identification. Each step relies on one of three parameters, S, N, and P, respectively. These parameters represent cell signal thresholds for each step of the clustering algorithm in terms of σ_{noise}, as summarized in Equation 3.2.

$$|S_{cell}| > \{S, N, P\} \rightarrow |E_{cell}| > \{S, N, P\}\sigma_{noise} \tag{3.2}$$

The first step of the clustering algorithm defines the primary seed threshold, with the default value of the seed threshold parameter S set to S=4. This means that any cells detecting a signal $E_{cell} > 4\sigma_{noise}$ are treated as seed cells for a topocluster.

The next step builds topoclusters around the identified seed cells by including neighboring cells that satisfy a minimum energy requirement based on the growth control parameter N, set to N=2 in ATLAS. This means that cells topologically connected to the seed cell that detect a signal $E_{cell} > 2\sigma_{noise}$ are identified as growth cells and added to the growing topocluster.

The final step defines the edges of the topoclusters by identifying boundary cells. In ATLAS, the parameter P, known as the principle cell filter, is set to P=0. This means that any cell neighboring a growth cell, but that does not satisfy the N=2 growth cell threshold itself, is included in the topocluster regardless of its signal.

This allows for cells on the boundary of the topocluster registering signal near noise levels to be included. A simple sketch illustrating the formation of topoclusters in a hypothetical calorimeter signal is shown in Figure 3.1.

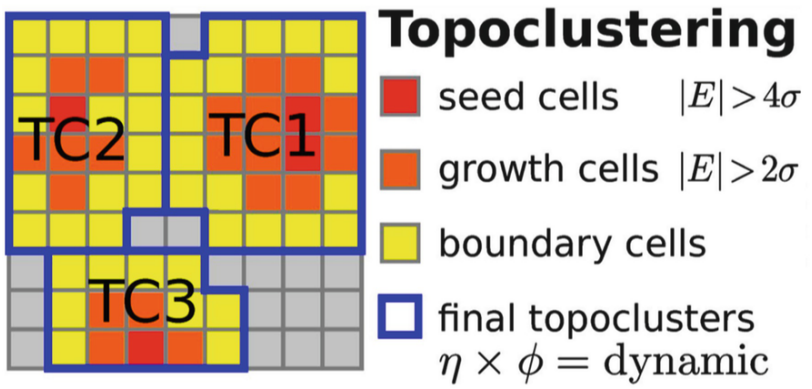

Figure 3.1: A sketch of topoclusters formed from a hypothetical calorimeter signal with the three types of cell classifications highlighted [38].

After they are formed, topoclusters are calibrated to more closely reflect the energy of the incident particle leaving a signal in the calorimeter. Topoclusters are first brought to the EM scale, where the calorimeters are capable of correctly measuring the energy of incident electromagnetic showers. Measurements at this scale are less accurate for hadronic showers due to the calorimeter response being lower by variable amounts depending on the location of the shower in the calorimeter. To counteract this, a further calibration known as local hadronic cell weighting (LCW) is applied to account for the effects of the lesser calorimeter response to hadrons, accidental signal losses due to the topocluster formation algorithms, and energy losses in any inactive material near the topocluster. LCW is derived from MC simulations of charged and

neutral pions interacting with the calorimeters and is able to classify topoclusters as either hadronic or electromagnetic and apply energy corrections accordingly. Through these calibrations applied at the topocluster-level, the eventual energy resolution of reconstructed jets is improved. A number of additional calibrations are applied to reconstructed jet objects, as will be discussed later in this chapter.

Particle Flow

Particle flow (PFlow) objects are an alternative jet input [10]. PFlow objects combine track information from the inner detector with topocluster information from the calorimeter. This is beneficial because the inner detector excels at measurement of lower p_T charged particles while also providing the ability to match individual particles to their vertex, and the calorimeter is necessary for measuring high p_T particles while also having the capability to measure neutral particles.

$$\Delta R' = \sqrt{\left(\frac{\Delta\phi}{\sigma_\phi}\right)^2 + \left(\frac{\Delta\eta}{\sigma_\eta}\right)^2} \tag{3.3}$$

The PFlow algorithm forms objects starting from tracks of $p_T < 40$ GeV originating from a primary vertex. The algorithm then attempts to match these tracks to the nearest topoclusters in the calorimeter based on the distance metric $\Delta R'$, as defined in Equation 3.3. Here, the $\Delta\eta$ and $\Delta\phi$ terms represent the angular distances between the track and the barycenter of the nearest topocluster and the σ_η and σ_ϕ terms represent the angular width of the topocluster, calculated as the standard deviation of the of the distance of the topocluster's cells from its barycenter. Tracks are matched to the nearest topocluster based on $\Delta R'$ value. In the case that no topocluster exists within $\Delta R' < 1.64$, the particle producing the track is assumed to have not

produced a topocluster in the calorimeter. In the event that the PFlow algorithm finds multiple possible topocluster matches for a single track, multiple topoclusters may be considered as part of a single PFlow object.

The composite track-topocluster objects make up the PFlow objects that are passed on to the jet reconstruction algorithms. The use of PFlow objects has been shown to improve jet p_T resolution and angular resolution while providing additional pileup mitigation.

3.1.2 Jet Reconstruction Algorithms

After jet detector signatures have been identified, these objects are input into jet reconstruction algorithms. The jet reconstruction algorithm used in ATLAS is the Anti-k_t Clustering Algorithm [13].

$$d_{ij} = min\left(p_{Ti}^{2p}, p_{Tj}^{2p}\right) \frac{\Delta R_{ij}^2}{R^2} \tag{3.4}$$

$$d_{iB} = p_{Ti}^{2p} \tag{3.5}$$

In the anti-k_t algorithm, a jet finding sequential recombination scheme is used to select topoclusters to be grouped to form jets. The basis of this grouping is two distance parameters as defined in Equations 3.4 and 3.5. Here, d_{ij} and d_{iB} represent distance metrics between two topoclusters and one topocluster and the beamline, respectively. Here, $\Delta R_{ij} = (y_i - y_j)^2 + (\phi_i - \phi_j)^2$, with y_i, ϕ_i, and p_{Ti} representing the rapidity, azimuthal angle, and transverse momentum of the ith topocluster, respectively. The radius parameter R sets the radius of the reconstructed jets, typically set to $R = 0.4$ or $R = 1.0$ in ATLAS for small and large radius jets, respectively.

The parameter p controls the order of topocluster combination by placing a relative importance on the topocluster energy versus geometrical distance in terms of which topoclusters are the first to be grouped. The implications of each choice of p parameter value are briefly discussed later in this section.

The jet reconstruction algorithm iterates through all identified topoclusters and calculates d_{ij} and d_{iB} for every possible pair of topoclusters. If the minimum value of d_{ij}, representing the distance between the two nearest topoclusters, is less than d_{iB}, then topoclusters i and j are combined into one object. If this criteria is not met, topocluster i is categorized as a jet and removed from consideration in further iterations of the algorithm. The distance metrics are then recalculated and the process repeated, iterating until all topoclusters have been addressed.

The parameter p sets the order of topocluster combination as it defines the relative importance of topocluster energy versus geometrical distance. The magnitude of p is unimportant in the distance metric calculations, but the sign controls the order of topocluster combination. Thus there are three options for the parameter- $p = -1, 0, 1$. The anti-k_t algorithm used by ATLAS is defined by its choice of $p = -1$. This choice of p puts a greater importance on the energy of the topocluster objects being combined, making the algorithm group the highest-p_T objects first. This means that the jet axis is largely defined in the first iteration of the sequential recombination scheme and the angular width of the jet is defined by the radius parameter R.

Other jet clustering algorithms are defined by different choices of value for the parameter p. The k_t algorithm uses $p = 1$, meaning that the softest jet constituents are grouped first. As softer constituents have more bearing on the shape of the jet, this algorithm generally produces jets with a more irregular shape. The Cambridge/Aachen

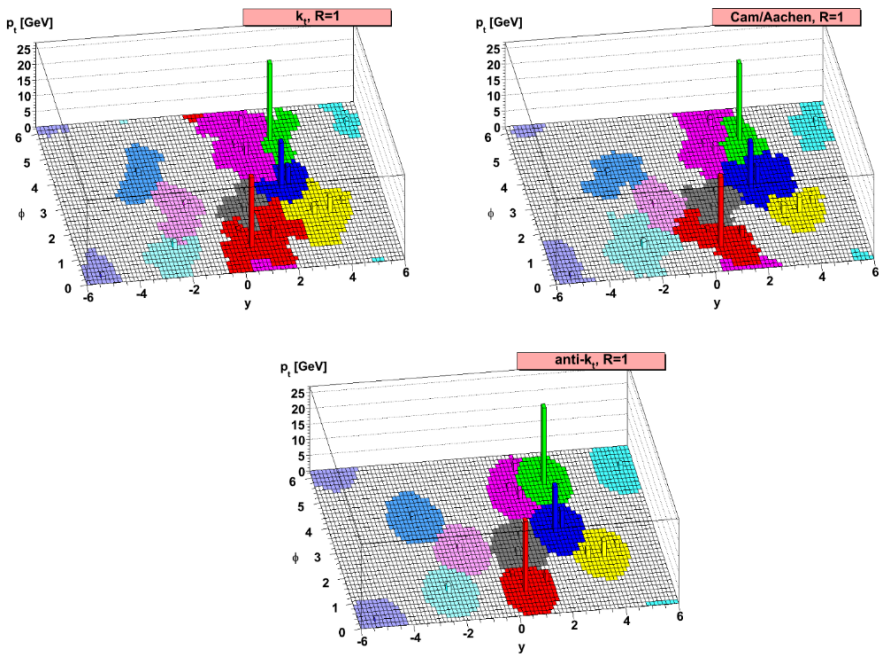

Figure 3.2: Example outputs of each jet reconstruction algorithm when applied to simulated data [13].

algorithm uses a value of $p = 0$, meaning that the topoclusters are grouped independent of p_T with the pairs with the smallest angular separation grouped together first. A comparison of the jets resulting from the various algorithms when applied to simulated data is shown in Figure 3.2.

3.2 Jet Calibration

After the jets have been reconstructed but before they may effectively be used for physics analysis, a sophisticated calibration scheme must be applied to adjust the signatures seen by the detector to more useful observables such as particle-level energy and mass. The full calibration scheme is broken down into a chain of smaller

steps, each aiming to correct different detector effects causing the raw jet signal to differ from the particle-level values.

In this section, an overview of the full jet calibration chain will be presented, with specific attention paid to the calibration as applied to small-radius (small-R) jets recorded during LHC Run 2. Over the course of this data-taking period, the jet calibration scheme was updated and improved, as will be discussed extensively in Chapter 4 and noted here when relevant. A complete discussion of small-R jet calibration schemes can be seen in [31].

3.2.1 Origin Correction

The first step of the jet calibration process, an origin correction, occurs at the topocluster level before the jet objects are fully reconstructed. This is the only step of the calibration process described in this section to be applied before the topoclusters are reconstructed.

The origin correction modifies the four-momenta of the topoclusters to point to the primary vertex of the hard-scattering interaction producing the topoclusters, rather than the center of the detector coordinate system. This correction does not alter the overall energy of the topoclusters. The application of this origin correction results in improved η-resolution in the eventual reconstructed jets.

3.2.2 Pileup Correction

The next step of the jet calibration process is focused on the mitigation of pileup. As discussed previously, pileup refers to the detector signatures coming from interactions separate from the hard-scatter event of interest. Because pileup is an unavoidable consequence of the high luminosity required to maximize the discovery power of

the LHC, it is important that methods are in place to correct for the extra energy deposited in the detector due to pileup interactions.

$$p_T^{corr} = p_T^{reco} - \rho \times A - \alpha \times (N_{PV} - 1) - \beta \times \langle \mu \rangle \tag{3.6}$$

The pileup correction applied to small-R jets includes three terms that are subtracted from the reconstructed jet p_T, as seen in Equation 3.6 [31]. The first term subtracted from reconstructed p_T is an area-based pileup subtraction and the latter two terms are residual N_{PV} and μ-based subtraction.

Area-based pileup subtraction

The first term subtracted from the reconstructed jet p_T is proportional to the area, A, of the jet and the median p_T-density, ρ, of all reconstructed jets in the event. The jet area serves as a measure of pileup susceptibility, as the larger the jet, the more likely it is to overlap with energy deposits originating from pileup events. The p_T-density p_T/A is calculated for each reconstructed jet, and the median p_T-density, ρ, is used to determine the contributions from pileup. The median p_T-density is used rather than the mean to avoid bias due to hard-scatter jets skewing the average to higher p_T values. The k_t algorithm is used to reconstruct the jets used for the calculation of ρ, taking advantage of the fact that this algorithm is more sensitive to soft radiation than than the anti-k_t algorithm used for jet physics object reconstruction. Only jets in the central region of the detector are considered in the calculation of ρ, as the detector granularity is not high enough in the forward region to properly account for pileup contributions. Example ρ distributions are shown in Figure 3.3 for various

pileup conditions. As expected, it is seen that ρ tends to be larger for higher values of N_{PV}.

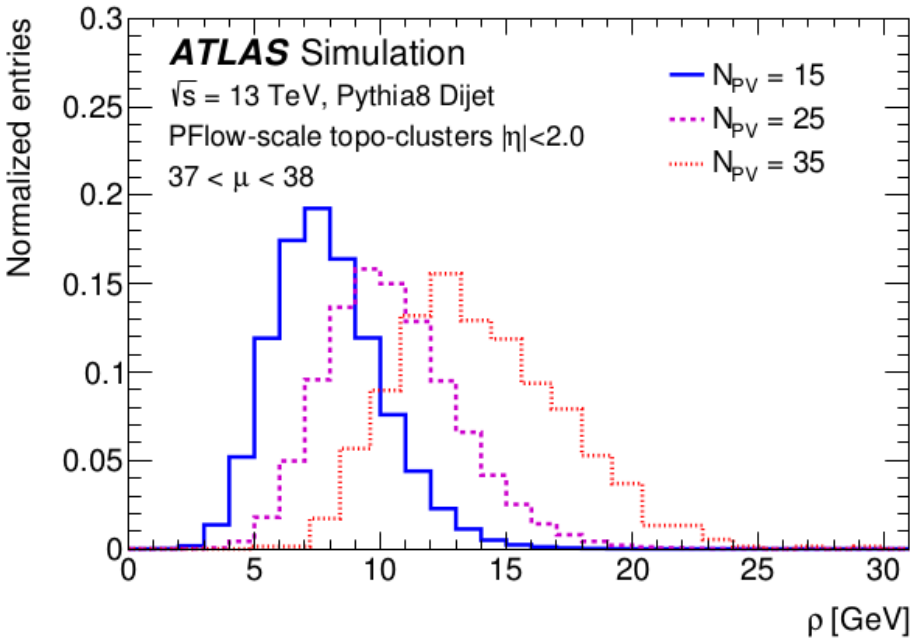

Figure 3.3: Example distributions of median p_T-density ρ for varying pileup conditions as measured by N_{PV}. [31]

Because the sensitivity to pileup is non-constant across the full detector volume, the jet area-based correction is not sufficient on its own and a residual dependence of the reconstructed jet p_T on pileup remains. Thus, additional terms must be subtracted from the reconstructed jet p_T to arrive at a suitably corrected value.

Residual pileup subtraction

In addition to the jet area-based subtraction, two more terms are subtracted from the reconstructed jet p_T to correct for residual p_T dependence on the pileup variables N_{PV} and $\langle\mu\rangle$. The residual pileup subtraction is performed by matching reconstructed jets to truth jets and calculating the difference between the truth jet transverse momentum and the reconstructed jet transverse momentum as a function of N_{PV} and μ. This serves to account for the dependence on both in-time and out-of-time pileup, measured by N_{PV} and μ, respectively. The residual dependencies of p_T on both N_{PV} and μ are seen to be approximately linear and fits are applied in bins of p_T^{truth} and $|\eta|$. The slopes of the linear fits, α and β corresponding to the N_{PV} and μ plots, respectively, are found to have logarithmic dependence on p_T^{truth} and fits are performed over the range $20 < p_T^{truth} < 200$ GeV in each $|\eta|$ bin. The nominal values of α and β are taken to be the values of these fits at $p_T = 25$ GeV, representing the p_T range where the pileup dependence is most pronounced. Lastly, linear fits are performed to the α and β coefficients as a function of $|\eta|$, reducing the effects of statistical fluctuations and allowing for smooth sampling in $|\eta|$.

The results of the full pileup subtraction scheme, including the area-based and residual subtractions, when applied to simulated data can be seen in Figure 3.4. The resulting jet p_T shows little dependence on pileup after the subtraction is applied.

3.2.3 MC-Based Calibrations

The next steps of the jet calibration scheme are categorized as simulation or Monte Carlo (MC)-based calibrations. These include an absolute jet energy scale calibration and the Global Sequential Calibration (GSC). The ultimate goal of these calibration

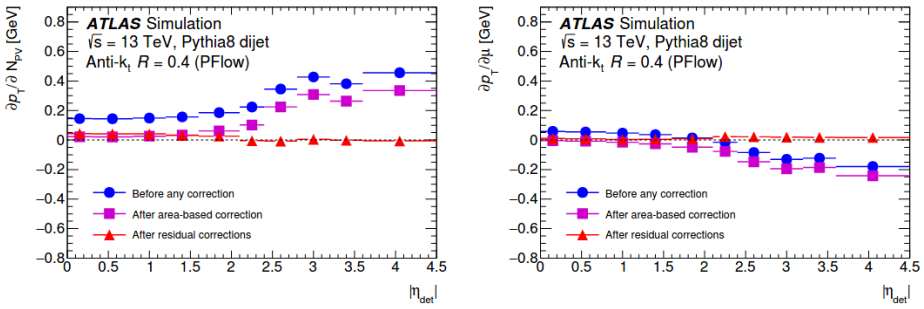

(a) In-time pile-up dependence

(b) Out-of-time pile-up dependence

Figure 3.4: Results of pileup subtraction showing the dependence of jet p_T on N_{PV}(a) and μ (b) as a function of $|\eta|$ N_{PV}. [31]

steps is to adjust the reconstructed jet four-momentum to match the simulated truth jets. Simulated data comes from PYTHIA 8 simulations.

Absolute Jet Energy Scale Calibration

The absolute jet energy scale calibration aims to bring the reconstructed jet four-momentum, specifically the jet energy and η, to that of the truth jet. The comparison between these objects is defined using the energy response, defined as the ratio of reconstructed jet energy to truth jet energy (E^{reco}/E^{truth}), and the pseudorapidity difference, defined as $\Delta\eta = \eta^{reco} - \eta^{truth}$. Both of these quantities are seen to vary throughout the detector, most significantly in transition regions where different detector technologies meet. Figure 3.5 shows the energy response for small-R PFlow jets as a function of detector pseudo rapidity, η_{det}, for several values of reconstructed jet energy. The jet energy response is higher for PFlow jets at low energies compared to EMTopo jets due to the addition of tracking information, but the characteristic shape of the distribution as a function of η_{det} remains similar. The shape of the

distribution reflects the geometry of the calorimeter system, with dips in the jet energy response corresponding to transitions regions at $|\eta_{det} = 1.4|$ and $|\eta_{det} = 3.1|$, representing the barrel-endcap and endcap-forward transitions, respectively. The jet energy response is seen to dip in these regions because there is less active detector area in the transition regions.

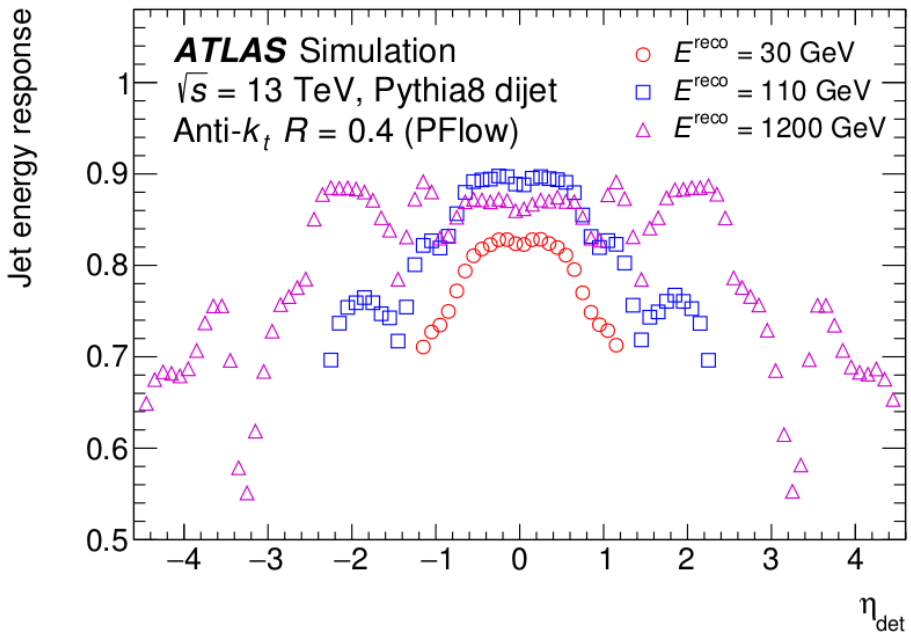

Figure 3.5: Representative example jet energy response plots at various reconstructed jet energy values. Plots depicted here show the jet energy response for small-R PFlow jets as a function of detector η. [31]

The average energy response, $R_E = \langle E^{reco}/E^{truth} \rangle$, is calculated as the mean of a guassian fit to the energy response distribution in each bin of truth jet energy and detector pseudo rapidity. A calibration factor, c_{JES} is then calculated as the inverse of

the average energy response and applied to bring the reconstructed jet four-momenta to that of the truth jets.

Global Sequential Calibration

Because the absolute jet energy scale calibration corrects based on the average jet energy response, some fluctuations remain due to the flavor, particle composition, and shower development varying from jet to jet. These fluctuations have a detrimental effect on the jet energy resolution (JER), defined as the width of the guassian fit to the jet response. To account for this, the global sequential calibration (GSC) [23] is applied.

The GSC applies a series of multiplicative corrections to small-R jets, correcting jets based on their longitudinal shower shape and associated track characteristics to improve the JER while leaving the average jet energy response unchanged. The five corrections (or six corrections if using PFlow jets) applied by the GSC use observables describing energy deposits in the calorimeter, track information, and energy deposits in the muon spectrometer. A multiplicative correction to the jet four-momentum is calculated as a function of p_T^{truth} and $|\eta_{det}|$ for each observable. The observables used by the GSC include:

- f_{charge} - the fraction of jet p_T measured from associated tracks with $p_T > 500MeV$ (only applied to PFlow jets)
- f_{Tile0} - the fraction of the jet energy measured in the first (0th) layer of the hadronic tile calorimeter
- f_{LAr3} - the fraction of the jet energy measured in the third layer of the EM liquid argon calorimeter

- n_{track} - the number of charged particle tracks associated with the jet
- $width_{track}$ - the average distance, weighted by p_T, between the associated tracks and the jet axis
- $N_{segments}$ - the number of muon spectrometer layers traversed by tracks associated with the jet

These observables carry information about the jet substructure and help correct for effects that negatively impact the calorimeter response to incident jets, including calorimeter non-compensation, differences in jet flavor and composition, energy losses due to inactive material in some areas of the detector, and energy deposited outside of the calorimeter layers. The f_{layer} variables are used to characterize the longitudinal jet structure. A large fraction of jet energy deposited in the hadronic calorimeter layers typically leads to a lower response due to calorimeter non-compensation. The tracking variables are used to differentiate jet flavors. Jets originating from a gluon tend to be softer, which leads to a lower calorimeter response. These gluon-initiated jets are identified by their wider shower profile, which corresponds to a larger n_{track} than for jets originating from quarks or leptons. For jets detected near a transition region between calorimeter modules, the width is also correlated to how many particles in the shower traverse the relatively poorly instrumented transition regions. The calorimeter response to uncontained jets that pass through the calorimeters to interact with the muon spectrometer is highly correlated to the number of muon spectrometer segments that detect a signal, $N_{segments}$. This depends on both the jet energy and the amount of detector material that the jet must pass through, which varies with η_{det}.

The GSC corrections are applied in the order listed above, however the improvements in JER are independent of the order. Different subsets of corrections are applied by the GSC depending on the $|\eta|$ range where the jet is detected. In the range $|\eta| < 1.7$, all five (or six if using PFlow jets) corrections are applied. In the range $1.7 < |\eta| < 2.5$, all except for the f_{Tile0}-based correction are applied. In the range $2.5 < |\eta| < 2.7$, only the f_{LAr3} and $N_{segments}$-based corrections are applied. Finally, in the range $2.7 < |\eta| < 3.5$, only the f_{LAr3}-based correction is applied.

The GSC can be split into corrections involving only calorimeter-based variables, and those using additional track-based variables. This is useful because tracking may not be available for all jet objects, especially at the trigger level, so it is possible to apply versions of the GSC with and without the track-based corrections.

The GSC was not implemented in the jet calibration scheme until 2017 and it led to significant improvements in jet trigger efficiencies, as will be discussed in detail in Chapter 4.

3.2.4 In Situ Calibrations

The simulation-based calibrations discussed in the previous section correct the jet four-momenta to that of simulated truth jets. The in situ calibrations, the final step of the calibration chain, account for any possible inaccuracies in the modeling when simulating physical processes or detector behavior including imperfections in the simulation of the hard scatter and underlying event, jet formation, pile-up, and interactions between particles and detector materials.

The in situ calibration includes multiple distinct analyses, all of which rely on a common method of calculating jet response by analysing events containing a jet

recoiling off of a well-calibrated reference object and taking the average ratio of the jet p_T to the reference object p_T. This in situ jet response is denoted as R_{insitu} in Equation 3.7. R_{insitu} is calculated in data and MC separately and their ratio is taken as a final in situ calibration factor to be applied to the data, denoted as the double ratio, c, in Equation 3.8. The calibration factor c provides an accurate estimate of the differences between jet response in simulation versus data and is robust against detrimental effects on the jet response like out-of-cone radiation and additional radiative jets, as these are canceled out in the ratio. c is measured in bins of reference object p_T and η before being parametrized as a function of jet p_T and η.

$$R_{insitu} = \frac{\langle p_T^{jet} \rangle}{\langle p_T^{ref} \rangle} \tag{3.7}$$

$$c = \frac{R_{insitu}^{data}}{R_{insitu}^{MC}} \tag{3.8}$$

The three stages of in situ analysis include the η-intercalibration, the Z+jet and γ+jet balance, and the multijet balance (MJB). These analyses are carried out sequentially. The first stage, the η-intercalibration, corrects the energy scale of forward jets ($0.8 < |\eta| < 4.5$) using dijet events where forward jets are balanced against a central jet ($|\eta| < 0.8$). This matches the energy scale of the forward jets to that of the central jets. Next, the Z+jet and γ+jet analyses balance jets recoiling against the p_T of a calibrated Z boson or photon. This step serves to correct low p_T jets. Lastly, the MJB analysis calibrates single high p_T jets recoiling off of systems of multiple low p_T jets, which have been well-calibrated in the previous steps. The response ratios measured in the latter two steps are then combined, resulting in a smooth, continuous calibration curve that is applicable over the full p_T range.

As the three analyses making up the in situ calibration are performed sequentially, the systematic uncertainties are propagated from one analysis to the next. Systematic uncertainties arise from the same three causes for each analysis- mismodeling of physics processes in simulation, uncertainty of measurement of reference objects, and uncertainties in the expected p_T balance due to the event topology. The uncertainty due to mismodeling is estimated by comparing the predictions of two different MC event generators and taking the difference as the uncertainty. The systematic uncertainty of measurement of the reference objects is taken as the $\pm 1\sigma$ uncertainties in each reference object's calibration, according to the ATLAS recommendations. The uncertainty arising from event topology is estimated by varying the event selections and studying the impact on the resulting response ratio between data and simulation.

The data-to-MC response ratio after each individual stage of the in situ calibrations, along with the result of the full in situ calibration, is shown in Figure 3.6. The data shown here is for small-R PFlow jets with the JES calibration already applied. The high level of agreement between data and MC response is indicative of what is seen in EMTopo jets as well. At low p_T, the full in situ calibration is dominated by contributions from the Z+jet and γ+jet analysis while the MJB dominates in the high p_T range. As the Z boson is a very well understood particle, the results of the Z+jet analysis provide strong calibrations with a high degree of statistical certainty. The γ+jet analysis is also able to provide very accurate calibrations due to high resolution when detecting photons relative to that of jet objects. Unfortunately, these more accurate analyses are limited in the high p_T range and the less-precise MJB analysis takes over. As jet objects typically have a lower resolution than Z bosons or

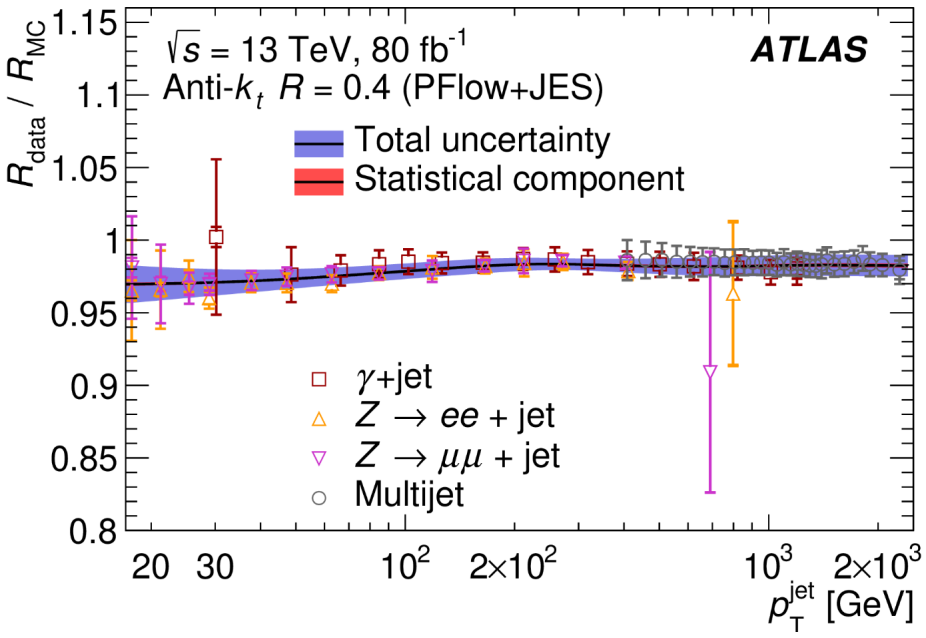

Figure 3.6: Data-to-MC response ratio after each stage of the in situ calibration, shown here for small-R PFlow jets with JES calibrations applied. The black curve shows the result of the full in situ calibration. The purple band shows the total uncertainty of the full in situ curve and the red band shows only the statistical component of the uncertainty [31].

photons, the MJB has a higher uncertainty while still contributing to a useful in situ calibration factor in this range.

3.3 Jet Energy Resolution and Cross-Section

It is important to precisely understand the jet energy resolution (JER) and cross-section when conducting physics measurements and performing searches for new physics using jets. The JER is a primary contributor to the uncertainty in physics analyses performed with jets. Additionally, good jet energy resolution is required for accurate measurement of missing transverse momentum, which is a very important

observable in many analyses. The jet cross-section provides important information about the strong coupling constant and the structure of the proton. Additionally, jet events are a predominate background at hadron colliders, and thus a firm understanding of their cross-section is crucial to carrying out predictive QCD calculations relevant to many searches for new physics.

3.3.1 Jet Energy Resolution

The JER is measured as the width of the gaussian p_T response distribution in a given bin. The JER is then parameterized as a function of p_T, using the expected dependence on calorimeter-based resolution with the three terms seen in Equation 3.9. Here, the three independent contributions are the noise, stochastic, and constant terms, represented by N, S, and C, respectively.

$$\frac{\sigma(p_T)}{p_T} = \frac{N}{p_T} \quad \oplus \frac{S}{\sqrt{p_T}} \quad \oplus C \tag{3.9}$$

The noise term describes the contribution to the detected signal from both electronic noise and pileup. Because both of these noise sources contribute directly to the energy measured by the calorimeter and are approximately independent of the energy deposited by particles traversing the calorimeter, the noise contribution to the JER scales as $1/p_T$. Thus, the noise term is expected to be most significant in the low-p_T region, up to approximately 30 GeV. The stochastic term describes statistical fluctuations in the amount of energy deposited by showering particles. The stochastic term scales as $1/\sqrt{p_T}$ and dominates in the p_T-range up to several hundred GeV. The constant term represents fluctuations that may be considered a constant fraction of the jet p_T, including energy deposited in inactive detector material, hadronic calorimeter

non-compensation, and differences in calorimeter response in different regions. The constant term dominates in the high-p_T range, above approximately 400 GeV.

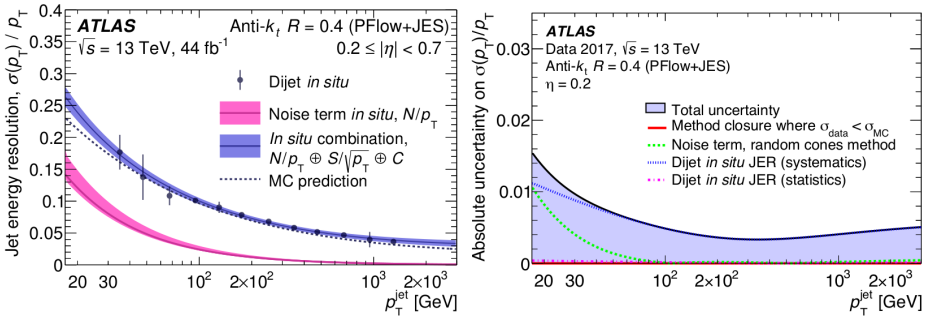

(a) (b)

Figure 3.7: (a) The jet energy resolution as a function of jet p_T, shown here for fully calibrated PFlow jets. Also shown is the isolated JER noise term and a comparison to the expected JER results from simulation. (b) Total uncertainty of the JER as a function of jet p_T, with individual contributions shown [31].

The JER measurement is done primarily using the momentum balance between the two leading jets in well-measured dijet events. The full JER is obtained by performing a fit to the dijet balance measurements, as shown in Figure 3.7 for fully calibrated PFlow jets. A comparison between the JER for PFlow jets and EMTopo is shown in Figure 3.8. As expected, the performance is similar between jet object types, but with PFlow jets performing better at the lower p_T range due to the inclusion of tracking information, which leads to both improved JER and less uncertainty.

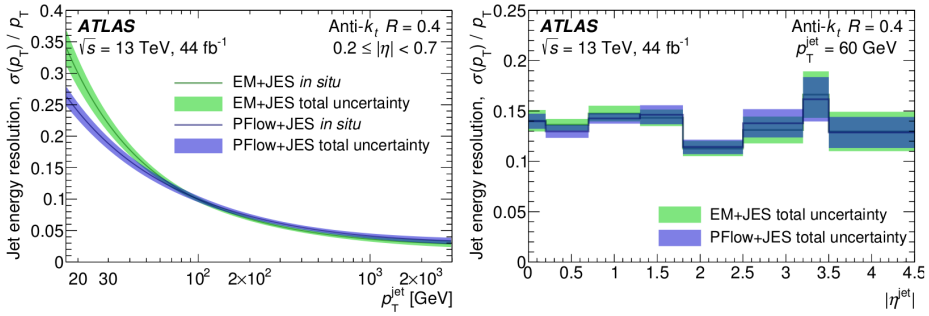

Figure 3.8: (a) A comparison of the jet energy resolution for fully calibrated PFlow and EMTopo jets (a) as a function of jet p_T and (b) as a function of jet $|\eta|$ [31].

3.3.2 Jet Cross-Section

Measurements of the inclusive jet cross-section [27] are determined using fully calibrated jets from data. The inclusive jet double-differential cross-sections are measured as a function of jet p_T, considering only jets with $p_T > 100$ GeV and $|y| < 3.0$, ensuring that the jet energy scale is well understood. Inclusive jet cross-section is measured as a function of jet p_T in six equal bins of the jet rapidity, $|y|$. The inclusive jet production cross-section is defined as seen in Equation 3.10, with N_{jets}, $\mathcal{L}$, Δp_T, and Δy denoting the number of jets in data in a given momentum and rapidity interval, integrated luminosity of the data in the same interval, the p_T range, and the rapidity range, respectively.

$$\frac{d^2\sigma}{dp_T dy} = \frac{N_{jets}}{\mathcal{L}\Delta p_T \Delta y} \tag{3.10}$$

Similarly, the dijet double-differential cross-section is also measured, as defined in Equation 3.11. This has a very similar form to the inclusive jet cross-section, but

depends on N_{dijet}, the number of dijet events in a given invariant mass and rapidity interval, Δm_{jj}, the interval of the invariant mass of the dijet system, and Δy^*, the interval of rapidity separation between jets in the dijet event. Similar to the inclusive jet cross-section, the dijet cross-section is measured as a function of the invariant mass of the dijet system, and divided into six equal bins of y^*.

$$\frac{d^2\sigma}{dm_{jj}dy^*} = \frac{N_{dijet}}{\mathcal{L}\Delta m_{jj}\Delta y^*} \tag{3.11}$$

The resulting inclusive jet and dijet cross-section measurements using data jets from $\sqrt{s} = 13$ TeV proton-proton collision data are shown in Figures 3.9 and 3.10, respectively. The measured cross-sections are compared to QCD simulations and show good agreement.

The high degree of agreement between the simulated predictions from theory and the measured cross-sections from data jets confirms that the jet reconstruction and calibration techniques discussed in this chapter successfully prepare the recorded jet objects for further analysis. As will be discussed extensively in the next chapter, it falls upon the jet trigger system to ensure that the discovery power of ATLAS is maximized by identifying and recording as many of these well-reconstruced and calibrated jets as possible.

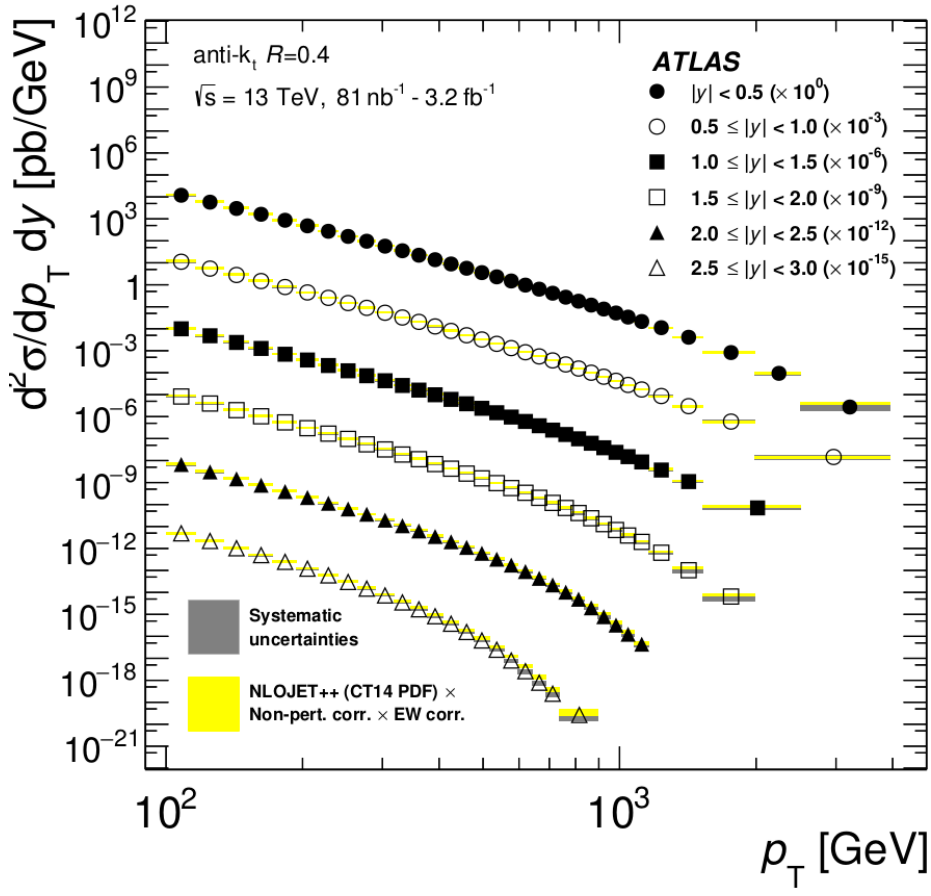

Figure 3.9: Measured inclusive jet cross-sections as a function of jet p_T in six bins of $|y|$. A comparison to QCD simulation using the NLOJET++ package (yellow) is presented for comparison [27]

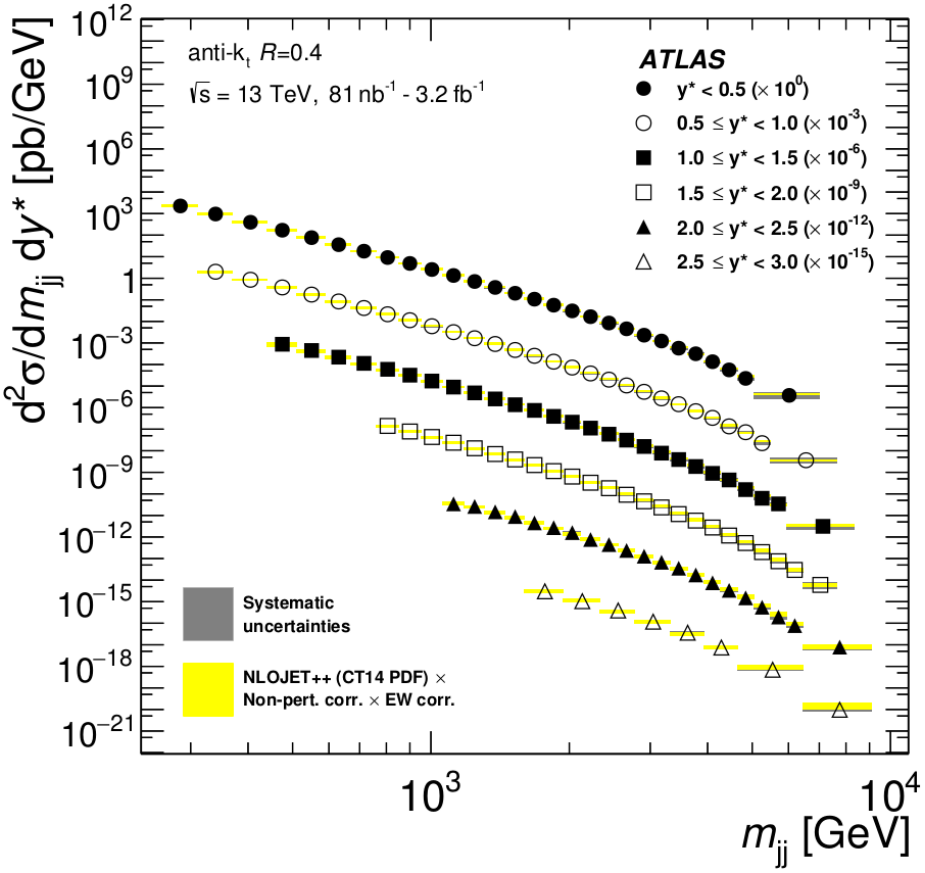

Figure 3.10: Measured dijet cross-sections as a function of dijet system invariant mass in six bins of y^*. A comparison to QCD simulation using the NLOJET++ package (yellow) is presented for comparison [27]

Chapter 4: Run-2 Jet Trigger Studies

The ATLAS jet trigger system plays a vital role in the experiment as a whole. All physics measurements and searches for new physics that require jet objects in the final state rely on the performance of the jet trigger system. Thus, it is vitally important that this system is optimized to ensure that as much of the data saved to disk is useful for further analysis as possible. This requires in-depth study of each jet trigger in the trigger menu, so as to understand the effects of changes over the course of Run-2 data taking, including changes to the jet calibration scheme, LHC operating conditions, and trigger prescaling.

In this chapter, the results of an analysis investigating the performance of the jet trigger system over the full Run-2 data-taking period are presented. First, the ATLAS jet trigger system is briefly re-introduced. Next, a discussion of jet trigger efficiencies and how to evaluate them is presented, highlighting the effects of improved jet calibrations and challenges due to increased luminosity and jet trigger prescaling. The results of a full analysis of the ATLAS Run-2 jet triggers are presented, specifically focusing on HLT jet triggers. Finally, a summary analysis showing the fraction of usable data for further physics analysis passing the jet triggers is shown.

4.1 Jet Triggering

The jet trigger system is responsible for identifying and saving interesting collision events that result in a final state involving one or more jet objects. As with the general ATLAS trigger system discussed in Chapter 2, the jet trigger system uses a hardware-based Level-1 (L1) trigger followed by a software-based High-Level Trigger (HLT). The L1 trigger uses combined input from the LAr and tile calorimeters to reconstruct jet objects. The HLT then takes the events passing the L1 trigger and applies online calibrations before checking that the events meet predefined trigger criteria (leading jet p_T, jet $|\eta|$, number of jets in the event, etc.) to be saved. Typical event rates in the HLT for the full trigger menu are shown in Figure 2.17 for an example LHC fill from 2018. Here the total rate at which events passing any jet triggers are written to disk is approximately 0.3 kHz at the start of the fill and drops to about 0.1 kHz at the end of the fill due to decreased beam intensity.

A table displaying an abridged ATLAS trigger menu for 2015 data taking is shown in Table 4.1. Here, the rate of several unprescaled jet triggers is shown, along with several other physics triggers and the total rate of the full ATLAS trigger system. Despite jets being the most frequently produced product of proton-proton collisions, the full ATLAS trigger bandwidth must be split between all possible signal types. As is evident in both Table 4.1 and Figure 2.17, the jet trigger accounts for just a portion, less than approximately 20%, of the full ATLAS trigger rate, thus the bandwidth reserved for the jet trigger must be allocated strategically to maximize its impact.

Trigger	**Typical offline selection**	**Trigger Selection**		**Level-1 Peak Rate (kHz)**	**HLT Peak Rate (Hz)**
		Level-1 (GeV)	HLT (GeV)	$L = 5 \times 10^{33}$ cm^{-2}s^{-1}	
Single leptons	Single iso μ, $p_{\mathrm{T}} > 21$ GeV	15	20	7	130
	Single e, $p_{\mathrm{T}} > 25$ GeV	20	24	18	139
	Single μ, $p_{\mathrm{T}} > 42$ GeV	20	40	5	33
	Single τ, $p_{\mathrm{T}} > 90$ GeV	60	80	2	41
Two leptons	Two μ's, each $p_{\mathrm{T}} > 11$ GeV	2×10	2×10	0.8	19
	Two μ's, $p_{\mathrm{T}} > 19, 10$ GeV	15	18, 8	7	18
	Two loose e's, each $p_{\mathrm{T}} > 15$ GeV	2×10	2×12	10	5
	One e & one μ, $p_{\mathrm{T}} > 10, 26$ GeV	20 (μ)	7, 24	5	1
	One loose e & one μ, $p_{\mathrm{T}} > 19, 15$ GeV	15, 10	17, 14	0.4	2
	Two τ's, $p_{\mathrm{T}} > 40, 30$ GeV	20, 12	35, 25	2	22
	One τ, one μ, $p_{\mathrm{T}} > 30, 15$ GeV	12, 10 (+jets)	25, 14	0.5	10
	One τ, one e, $p_{\mathrm{T}} > 30, 19$ GeV	12, 15 (+jets)	25, 17	1	3.9
Three leptons	Three loose e's, $p_{\mathrm{T}} > 19, 11, 11$ GeV	15, 2×7	17, 2×9	3	< 0.1
	Three μ's, each $p_{\mathrm{T}} > 8$ GeV	3×6	3×6	< 0.1	4
	Three μ's, $p_{\mathrm{T}} > 19, 2 \times 6$ GeV	15	18, 2×4	7	2
	Two μ's & one e, $p_{\mathrm{T}} > 2 \times 11, 14$ GeV	2×10 (μ's)	2×10, 12	0.8	0.2
	Two loose e's & one μ, $p_{\mathrm{T}} > 2 \times 11, 11$ GeV	2×8, 10	2×12, 10	0.3	< 0.1
One photon	one γ, $p_{\mathrm{T}} > 125$ GeV	22	120	8	20
Two photons	Two loose γ's, $p_{\mathrm{T}} > 40, 30$ GeV	2×15	35, 25	1.5	12
	Two tight γ's, $p_{\mathrm{T}} > 25, 25$ GeV	2×15	2×20	1.5	7
Single jet	Jet ($R = 0.4$), $p_{\mathrm{T}} > 400$ GeV	100	360	0.9	18
	Jet ($R = 1.0$), $p_{\mathrm{T}} > 400$ GeV	100	360	0.9	23
$E_{\mathrm{T}}^{\mathrm{miss}}$	$E_{\mathrm{T}}^{\mathrm{miss}} > 180$ GeV	50	70	0.7	55
Multi-jets	Four jets, each $p_{\mathrm{T}} > 95$ GeV	3×40	4×85	0.3	20
	Five jets, each $p_{\mathrm{T}} > 70$ GeV	4×20	5×60	0.4	15
	Six jets, each $p_{\mathrm{T}} > 55$ GeV	4×15	6×45	1.0	12
b−jets	One loose b, $p_{\mathrm{T}} > 235$ GeV	100	225	0.9	35
	Two medium b's, $p_{\mathrm{T}} > 160, 60$ GeV	100	150, 50	0.9	9
	One b & three jets, each $p_{\mathrm{T}} > 75$ GeV	3×25	4×65	0.9	11
	Two b & two jets, each $p_{\mathrm{T}} > 45$ GeV	3×25	4×35	0.9	9
b−physics	Two μ's, $p_{\mathrm{T}} > 6, 4$ GeV plus dedicated b-physics selections	6, 4	6, 4	8	52
Total				70	1400

Table 4.1: The main ATLAS triggers used in 2015 for runs with peak luminosity L $= 5 \times 10^{33}$ cm^{-2}s^{-1}. The total rate shown here is for the full trigger menu, which includes many more triggers than those shown here. The information pertaining to jet triggers shown here is for several common lowest un-prescaled triggers [20]

.

4.1.1 Jet Trigger Menu

The ATLAS trigger system is configured with a list of criteria for events to satisfy in order to be saved to offline storage, known as the trigger menu. The trigger menu is designed to include a full set of triggers covering all physics channels of interest while managing trigger bandwidth limitations. The jet trigger menu refers to the subset of the full ATLAS trigger menu accounting for events involving jet objects and will be the focus of this section.

The jet trigger menu sets trigger criteria based on variables like number of jet objects in an event, jet p_T, jet η range, and other parameters that describe the quality of jet identification or reconstruction at the trigger level. Jet triggers follow a naming scheme that describe the trigger criteria. Jet trigger names start with a string denoting the trigger level, "L1" or "HLT", followed by a string describing the details of the trigger criteria. This string will always include an upper or lowercase "j", corresponding to L1 and HLT jet triggers, respectively. The number of jets required by the trigger is denoted by an integer preceding the "j" in the trigger name, with no integer in the name implying that it is a single jet trigger requiring only one jet at minimum. Immediately following the "j" in this detail string is the p_T threshold each trigger jet is required to meet in order to pass the trigger. After this, additional identifying information may be included in the trigger name, such as required η range of the trigger jets or identifiers describing the jet reconstruction algorithm used. If no extra identifying information is present, it is implied that the trigger is based on anti-k_t jets with a small-R radius parameter of 0.4. Several example jet trigger names are listed in Table 4.2, along with descriptions of the trigger parameters.

Jet Trigger Name	Description
HLT_j420	Single jet HLT trigger requiring leading jet p_T above 420 GeV
HLT_4j60	Multijet HLT trigger requiring at least four jets with p_T above 60 GeV
HLT_j260_320eta490	Single forward jet HLT trigger requiring leading jet p_T above 260 GeV and $3.2 < \|\eta\| < 4.9$
HLT_j225_gsc440_boffperf_split	Single jet HLT trigger requiring leading jet p_T above 440 GeV after the online GSC calibration has been applied to jets measuring above 225 GeV in p_T
L1_J100	Single jet Level-1 trigger requiring leading jet p_T above 100 GeV
L1_J100.31ETA49	Single forward jet Level-1 trigger requiring leading jet p_T above 100 GeV and $3.1 < \|\eta\| < 4.9$
L1_4J20	Multijet Level-1 trigger requiring at least four jets with p_T above 20 GeV
HLT_j460_a10r_L1J100	Single large-R jet trigger requiring leading jet p_T above 460 GeV, denotes R=1.0 reclustered jets seeded from L1J100 trigger

Table 4.2: Table showing example jet trigger names and descriptions. Many more triggers exist in the full trigger menu, but a sampling of the naming schemes are shown here.

4.1.2 Jet Trigger Prescaling

Jet objects are the most common products of proton-proton collisions. Therefore, it is impossible to save every event containing final state jets as even the full L1 trigger bandwidth could not handle the event rate, even without considering the multitude of non-jet triggers needed by ATLAS. In order to strategically lower the jet trigger rate to an acceptable value in terms of trigger bandwidth and data storage limitations, the prescaling technique previously introduced in Chapter 2 is utilised. Jet trigger prescaling is something of a necessary evil, as it ensures that trigger bandwidth is available to the more infrequently firing high-p_T jet triggers where it is more likely that interesting physics events will be seen, but greatly limits sensitivity to the more common low-p_T jet events due to the loss of statistical significance in this range. Some analyses in the low-p_T range, like measurements of well-understood standard model objects, have such a high event rate that they are relatively unaffected by prescaling, while others, like searches for potential rare new physics signatures, are made more difficult by throttling already minuscule event rates. Prescale factors for various jet triggers may range from 1 (meaning all events passing the trigger are written to disk) to $\mathcal{O}(10000)$ (meaning one event out of $\mathcal{O}(10000)$ passing the trigger is written to disk), with the more aggressive prescaling applied to jet triggers with the lowest p_T thresholds.

As the luminosity of the LHC increased over the course of Run 2, the jet trigger prescaling strategy was adjusted accordingly, including increasing the jet p_T thresholds where prescaling is no longer required. Increasing the LHC luminosity naturally leads to higher event rates, necessitating more aggressive prescaling to maintain jet trigger rates within the constraints of the trigger system's bandwidth limitations.

This further limited the statistical precision achieved by lower-p_T jet triggers as the Run-2 data taking period progressed. For instance, the lowest un-prescaled single jet triggers, meaning the lowest p_T threshold single jet triggers to have no prescaling applied, increased from HLT_j360 to HLT_j380 to HLT_j420 from 2015 to 2016 to 2017/2018, respectively. The analyses most effected by trigger prescaling are those that rely on purely jet signatures, such as multijet analyses without leptonic trigger options, standard model measurements of jets and cross-sections, and calibrations such as the multijet balanace and those involving jets recoiling off of a reference object. This is observed in Figure 3.6, where the total uncertainty of the in situ calibration curve at low p_T values is dominated by the statistical uncertainty of the jet balance components. Here, the larger statistical uncertainty is due to the smaller sample size acquired by the prescaled triggers active in this range. The unavoidable loss of statistical precision in prescaled triggers at lower p_T ranges underscores the importance of maximally efficient jet triggers, as it is increasingly important that the events that make it through the prescaling process are useful for further analysis.

4.2 Jet Trigger Efficiency Studies

Not all jet events that pass a given jet trigger are necessarily useful for further offline analysis. For each jet trigger, a leading jet p_T threshold is defined for the event to pass the trigger, and it is not uncommon for events containing jets with p_T values near this threshold to incorrectly pass a trigger due to slight mis-calibration. This happens at both the L1 and HLT levels. As a result, each jet trigger has a so-called turn-on region above the trigger p_T threshold before the trigger becomes fully efficient and the saved data is safely usable for further physics analysis. The

analysis discussed in this section is aimed at studying the efficiency of the full suite of ATLAS jet triggers active in Run-2, highlighting the gains achieved via improved HLT jet calibration schemes and noting major causes of jet trigger inefficiencies and areas of potential improvement in the future.

4.2.1 Introduction to Trigger Efficiency Curves

In order to study and understand the performance of the Run-2 jet triggers in detail, trigger efficiency curves, colloquially called turn-on curves, are plotted. Trigger turn-on curves convey a lot of information about the performance of a trigger in a single plot. Some of the important qualities of these plots are described in this section, using the example turn-on curve seen in Figure 4.1 as a reference.

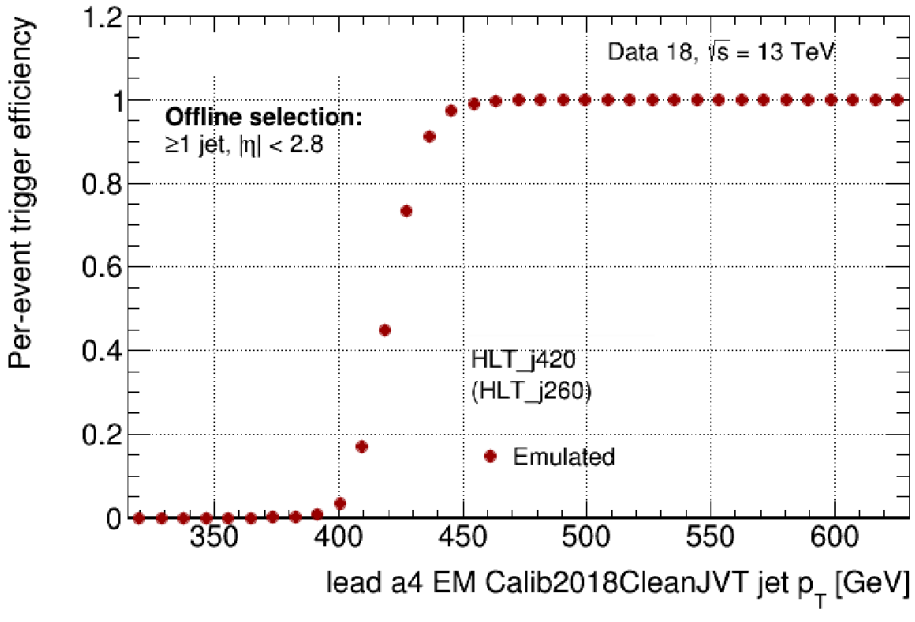

Figure 4.1: An example jet trigger turn-on curve showing the efficiency of the probe trigger HLT_j420 using HLT_j260 as the reference trigger with 2018 data.

Trigger Efficiency

The jet trigger efficiency discussed in this chapter describes the probability that an event with offline jet reconstruction and calibration applied will have a corresponding event at the trigger level that satisfies a given set of trigger selection criteria. This is what is known as per-event trigger efficiency. The most important objects pertaining to per-event trigger efficiency measurement are those used as trigger criteria, typically the leading jet(s) in the event. Thus, the jet trigger efficiency curves presented here will generally show the per-event trigger efficiency as a function of offline leading jet p_T, unless otherwise noted.

Probe/Reference Triggers

In order to analyze a trigger's efficiency, probe and reference triggers must be specified. The probe trigger is the focus of the efficiency analysis and the reference trigger serves as an independent, unbiased trigger necessary to study the probe trigger's efficiency in collision data, as data saved by the probe trigger is biased by having already passed that trigger by default. The reference trigger is typically chosen to have a significantly lower p_T threshold such that the region to be studied for the probe trigger is already fully efficient in the reference. In the example turn-on curve displayed in Figure 4.1, the probe trigger is HLT_j420 and the reference trigger is HLT_j260.

Trigger Turn-On Region

The trigger turn-on region refers to the portion of the curve where the efficiency increases from zero to (ideally) one. In the example shown in Figure 4.1, this region lies between approximately 390-460 GeV. This region shows the range of jet p_T at

the HLT level where jets may be mis-calibrated and allowed to pass the probe trigger when they actually should have been rejected. A broad trigger turn-on region typically indicates a more inefficient trigger than one with a steeper rise in its turn-on curve.

As will be discussed later in this chapter, a primary improvement that can be made to increase the efficiency of jet triggers, and therefore sharpen their turn-on curves, is additional or improved jet calibrations at the trigger level. These serve to reduce the number of events that pass a trigger, rather than be rejected, due to mis-calibration by trigger level algorithms.

In some cases, as will be seen in some of the jet trigger efficiency analysis plots presented later in this chapter, perfectly suitable reference triggers may not be available for a given probe trigger. If the reference trigger's p_T threshold is too close to that of the probe trigger, this may sometimes cause the low-p_T end of the turn-on curve to fail to reach 0 prior to the turn-on region. In other cases, when the reference trigger threshold is very close to that of the probe trigger, this may also cause a prominent uptick in the trigger efficiency curve before the onset of the turnon region. These issues are avoided wherever possible, but they are mainly cosmetic, as the most important takeaway from analysis of jet trigger turn-on curves is how quickly the efficiency reaches 1 (or a value very close to 1).

Trigger Efficiency Point

The jet trigger efficiency point refers to the point in the turn-on curve after which all subsequent points are above a given efficiency value. Physics analyses that rely on data taken with a jet trigger set a cutoff on which events can be used as reliable data based on trigger efficiency points. Efficiency points commonly specified by analyses

include 95% and 99%, and only the events with leading jet p_T above these points would be considered useful data for further physics analysis.

In the example plot given in Figure 4.1, one could estimate by eye the 99% efficiency point to be approximately 470 GeV. This means that a physics analysis looking to use events that satisfy the HLT_j420 jet trigger would actually be forced to start with a lower bound approximately 50 GeV higher than the trigger threshold itself. It is therefore important to optimize jet trigger efficiencies so as to lower the efficiency point as far as possible and maximize the percentage of collected data that can be used for further analysis. Such considerations are especially important when considering physics analyses within ATLAS that probe for new physics in the low-p_T regime.

Trigger Decision Tool Versus Emulation

The jet trigger turn-on curves may depict either data collected using the Trigger Decision Tool (TDT) or through emulation. Data collected with the TDT represents the true number of events that pass a trigger during data collection, while emulation uses all jets reconstructed and calibrated at the HLT level and uses them to recalculate the jet trigger decision of a given trigger, regardless of if they were recorded by that trigger. Emulation is a useful tool that allows for trigger decisions to be analyzed even if a trigger was not fired due to prescaling, allowing for jet trigger efficiency to be studied at much higher levels of statistical precision thanks to an increased number of trigger decisions to analyze. Unless otherwise stated, emulation is used in the jet trigger efficiency studies presented in this chapter.

4.2.2 Results From Run-2 Data

The results presented in this section use the full Run 2 data set. Run 2 data taking spanned from 2015 to 2018, with run conditions varying in each year. The most notable difference from year to year is the increasing average instantaneous luminosity as Run 2 progressed. As a result, the total integrated luminosity, representing the total amount of data collected, also increased in each year of Run 2 data taking, as displayed in Figure 4.2a. The integrated luminosity recorded by ATLAS for each period was approximately 4 fb^{-1}, 36 fb^{-1}, 47 fb^{-1}, and 61 fb^{-1} in 2015, 2016, 2017, and 2018, respectively. As has been discussed in previous chapters, increasing luminosity leads to increasing pileup. The average number of interactions per bunch crossing, a measure of pileup, may be seen in Figure 4.2b. The effects of increased pileup on the performance of the Run 2 jet triggers will be a frequent point of discussion in the analysis presented in this section.

The data used in the following analysis has several selections applied. First, all of the data is cleaned using the "LooseBad" jet cleaning criteria. This data quality check, described fully in [24], uses a selection of tracking and calorimeter-based variables to discriminate high quality jets from background induced by noise and cosmic muons. Next, the Jet Vertex Tagger (JVT) [22] is applied in an effort to remove jets originating from pileup interactions from the dataset. The JVT uses track-based variables to identify jets coming from the primary vertex of a collision event, helping to suppress the effects of pileup jets in the data. As the JVT requires input from the tracking system, it can only be utilized in jets in the central region of the detector ($|\eta| < 2.5$). Lastly, a transverse energy (E_T) cut is applied, removing events that have leading jet $E_T < 15$ GeV from the dataset. This is due to the ATLAS

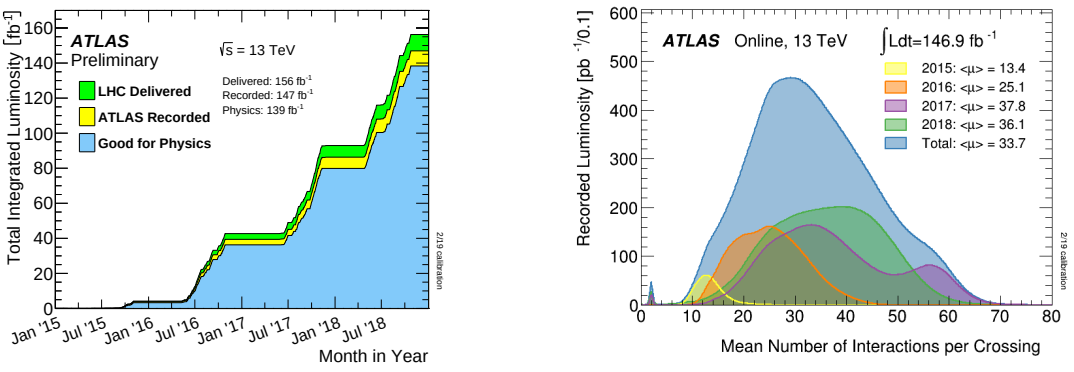

(a) (b)

Figure 4.2: (a) The cumulative integrated luminosity vs time over the course of LHC Run 2 proton-proton data taking. Shown is the LHC delivered, representing the luminosity delivered from the start of stable beams until ATLAS is put in standby mode, ATLAS recorded, which accounts for data acquisition inefficiencies and startup times of various sub detectors, and good for physics, representing when all reconstructed physics objects are of good quality, integrated luminosity distributions [19]. (b) Interactions per bunch crossing for proton-proton collision data collected in each year of Run 2 [19].

recommendation to not use offline jets below 20 GeV for analysis, largely because of the limitations in jet calibrations in the extremely high pileup regime below p_T values of approximately 15 GeV.

Single Jet Trigger Efficiencies

Figure 4.3 depicts the efficiency curves for the full suite of HLT single jet triggers in the standard η range ($|\eta| < 3.2$) for the 2015, 2016, 2017, and 2018 data collection periods. These plots illustrate the range of jet p_T covered by the jet trigger menu during data collection in each year. Figures 4.4, 4.5, 4.6, and 4.7 show zoomed-in views of these single jet efficiency curves in the low, medium, and high p_T regions, where the details of the turn-on curve behavior can be more clearly seen for each

trigger. The 2015 and 2016 plots are made with the full data set from these years, while these versions of the 2017 and 2018 plots are made with approximately 80 and 99 percent of their respective data sets due to data processing issues.

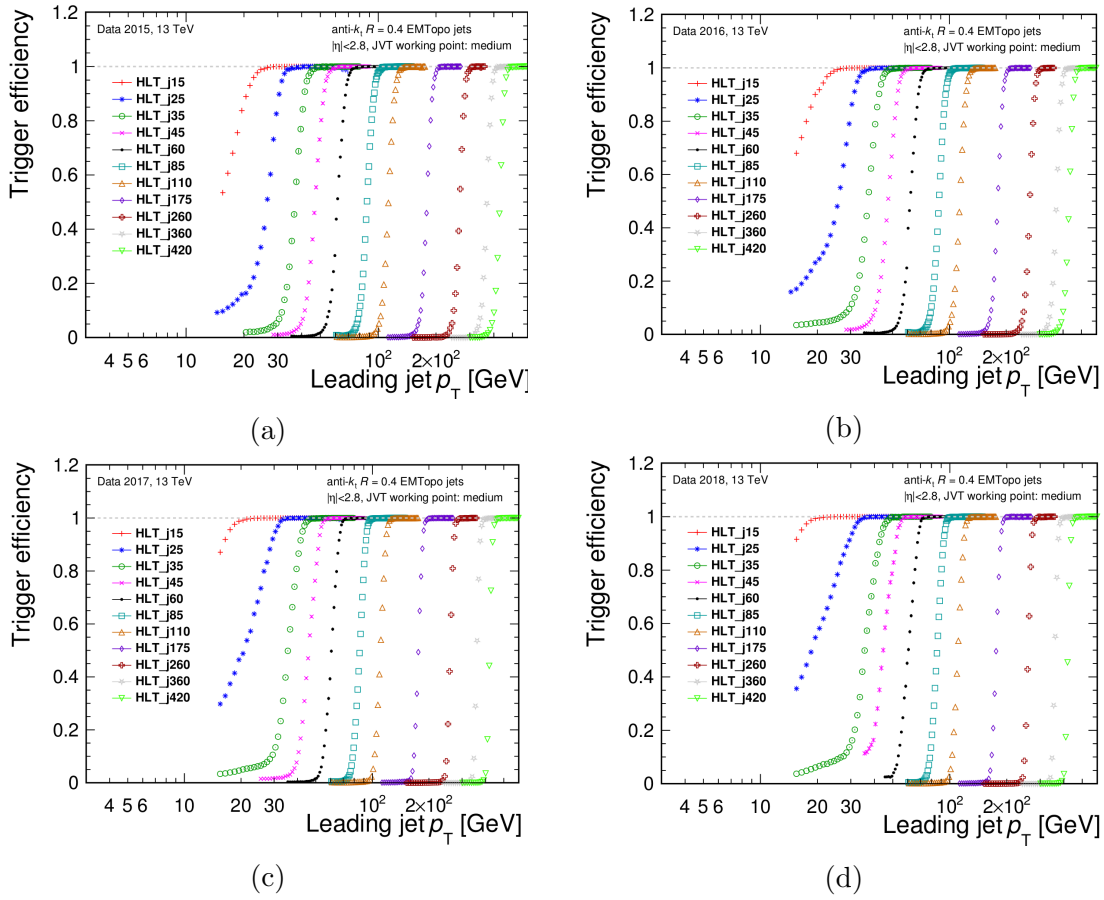

Figure 4.3: The full set of single jet HLT trigger efficiency curves active in 2015 (a), 2016 (b), 2017 (c), and 2018 (d).

As is readily apparent, the E_T cut imposed in data selection leads to an abrupt cutoff in the lowest p_T trigger efficiency curves, namely the HLT_j15 and HLT_j25 curves. This unfortunately limits the range of these curves that is able to be populated

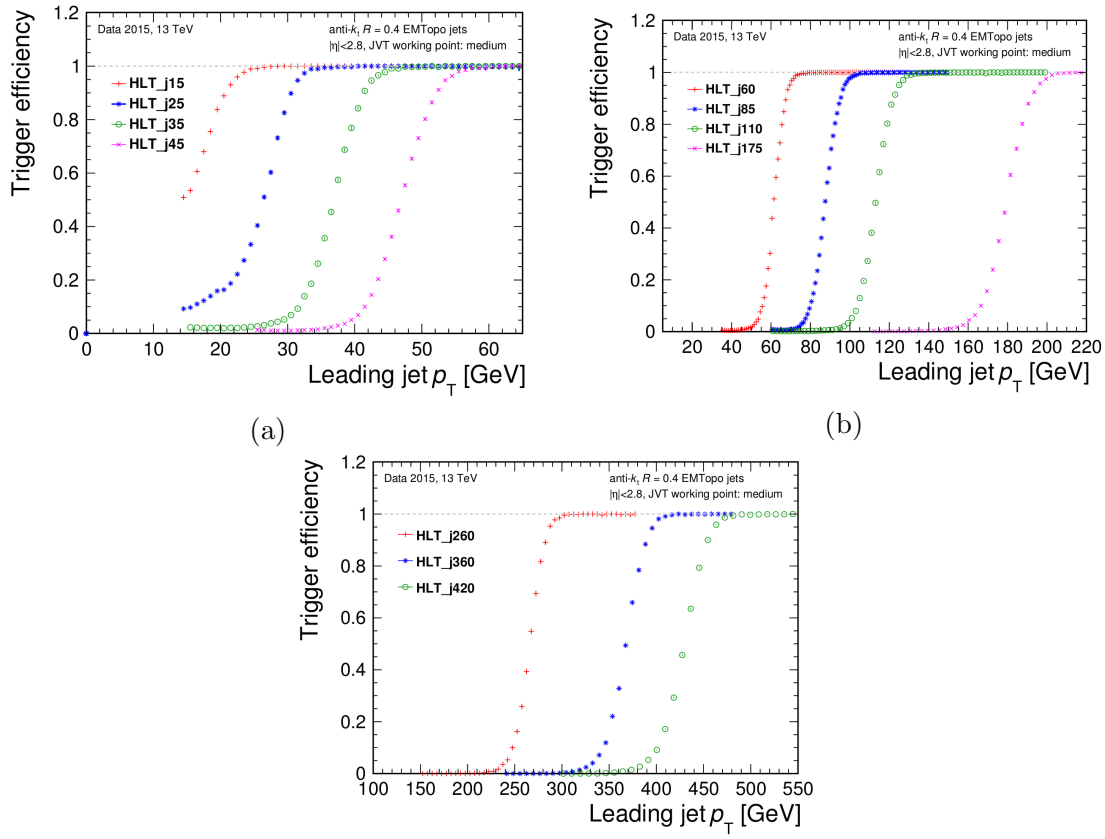

Figure 4.4: A zoomed-in view of the efficiency curves depicted in Figure 4.3a showing the lower-p_T (a), mid-p_T (b), and high-p_T (c) ranges of the 2015 single jet triggers.

with data, primarily effecting the HLT_j15 curve where much of the turn-on region is trimmed away.

Despite best efforts to suppress the effects of pileup, it still has non-negligible effects on the jet trigger efficiency curves shown in this section. This is not unexpected, as pileup jets are ever present in the chaotic proton-proton collision environment and they are often misidentified as having originated from the hard-scattering interaction, especially at lower p_T values where pileup jets are most prevalent. The most noticeable

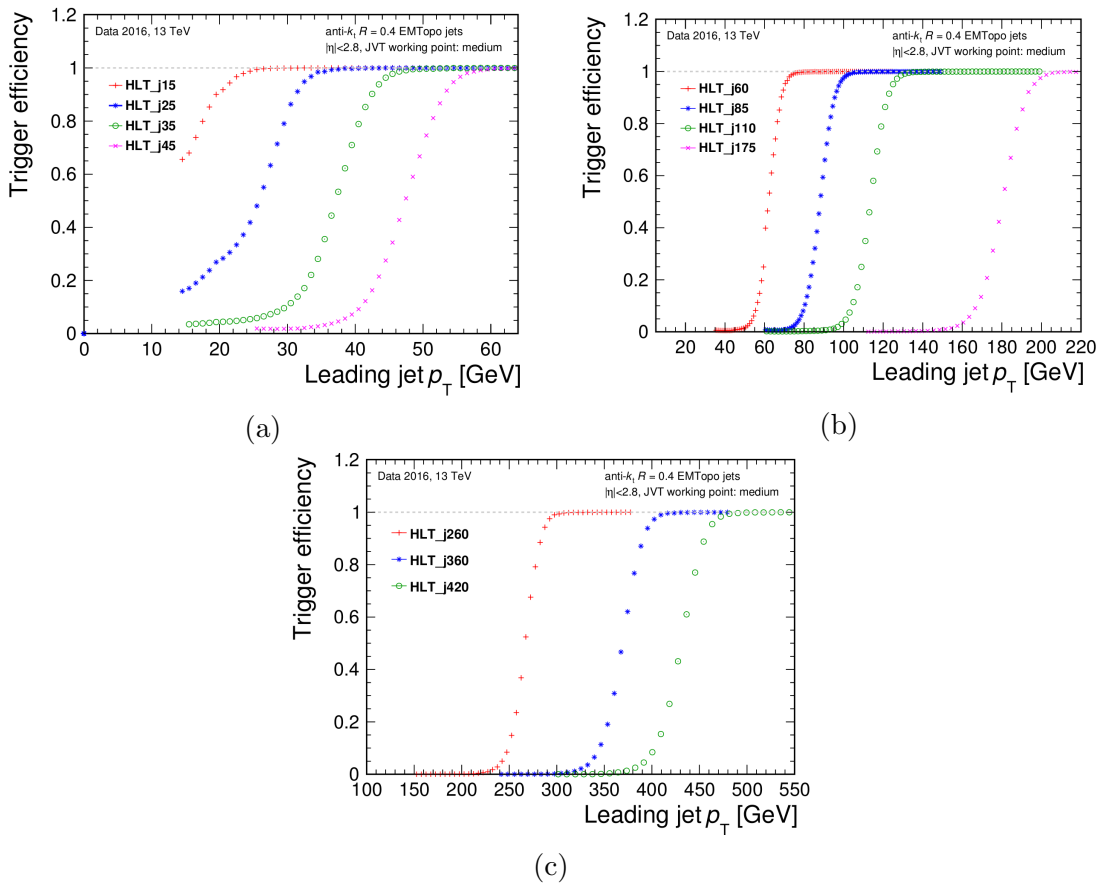

Figure 4.5: A zoomed-in view of the efficiency curves depicted in Figure 4.3b showing the lower-p_T (a), mid-p_T (b), and high-p_T (c) ranges of the 2016 single jet triggers.

pileup effect seen in the single jet trigger efficiency curves presented in Figures 4.3 through 4.7 is the non-smooth curve shape seen most prominently in the low-p_T range of the HLT_j25 efficiency curves, as well as the portion of the HLT_j15 curves prior to the imposed p_T cutoff, in each year. Another significant effect is the widening of the trigger turn-on region in data-taking periods with higher luminosity, and therefor higher pileup. This effect is more clearly seen in the inter-year comparison plots presented later in this section.

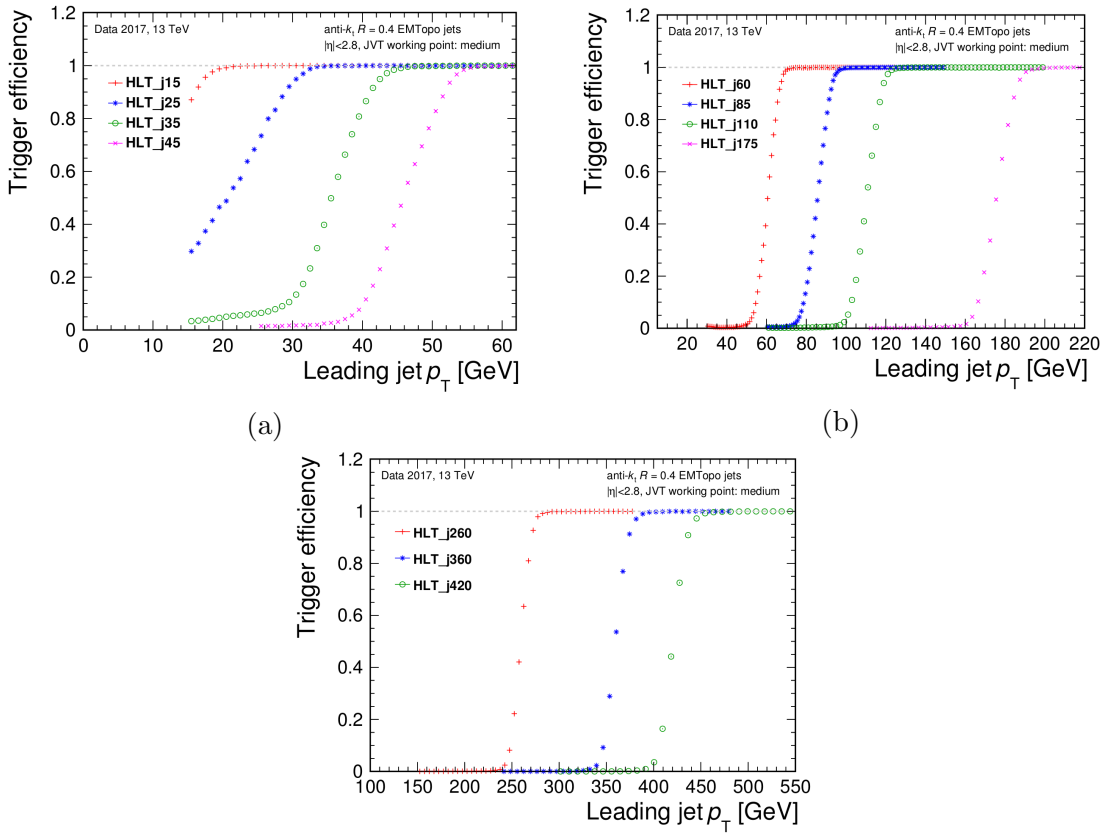

Figure 4.6: A zoomed-in view of the efficiency curves depicted in Figure 4.3c showing the lower-p_T (a), mid-p_T (b), and high-p_T (c) ranges of the 2017 single jet triggers.

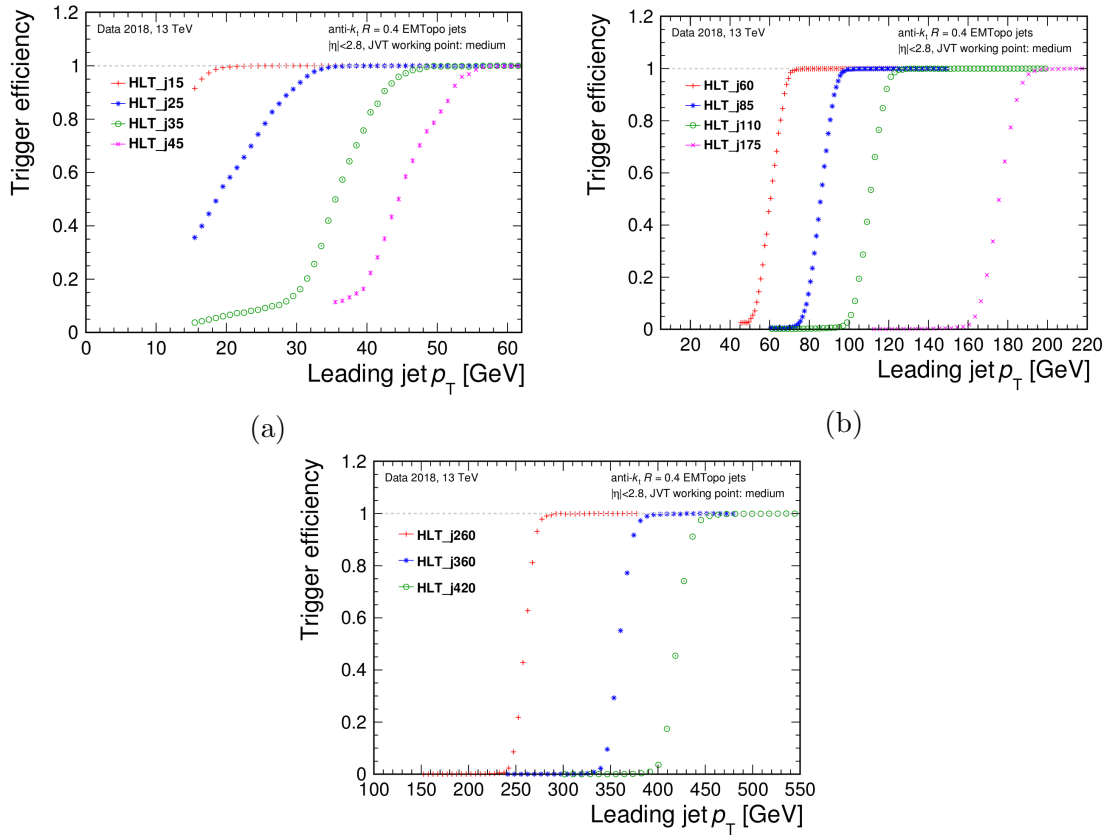

Figure 4.7: A zoomed-in view of the efficiency curves depicted in Figure 4.3d showing the lower-p_T (a), mid-p_T (b), and high-p_T (c) ranges of the 2018 single jet triggers.

Single Jet Forward Triggers

Figure 4.8 shows the trigger efficiency curves for the full suite of HLT single jet triggers in the forward eta range ($3.2 < |\eta| < 4.9$) for 2015, 2016, 2017, and 2018. Figures 4.9, 4.10, 4.11, and 4.12 show zoomed-in views of these forward jet trigger efficiency curves where finer details of their behavior can be seen.

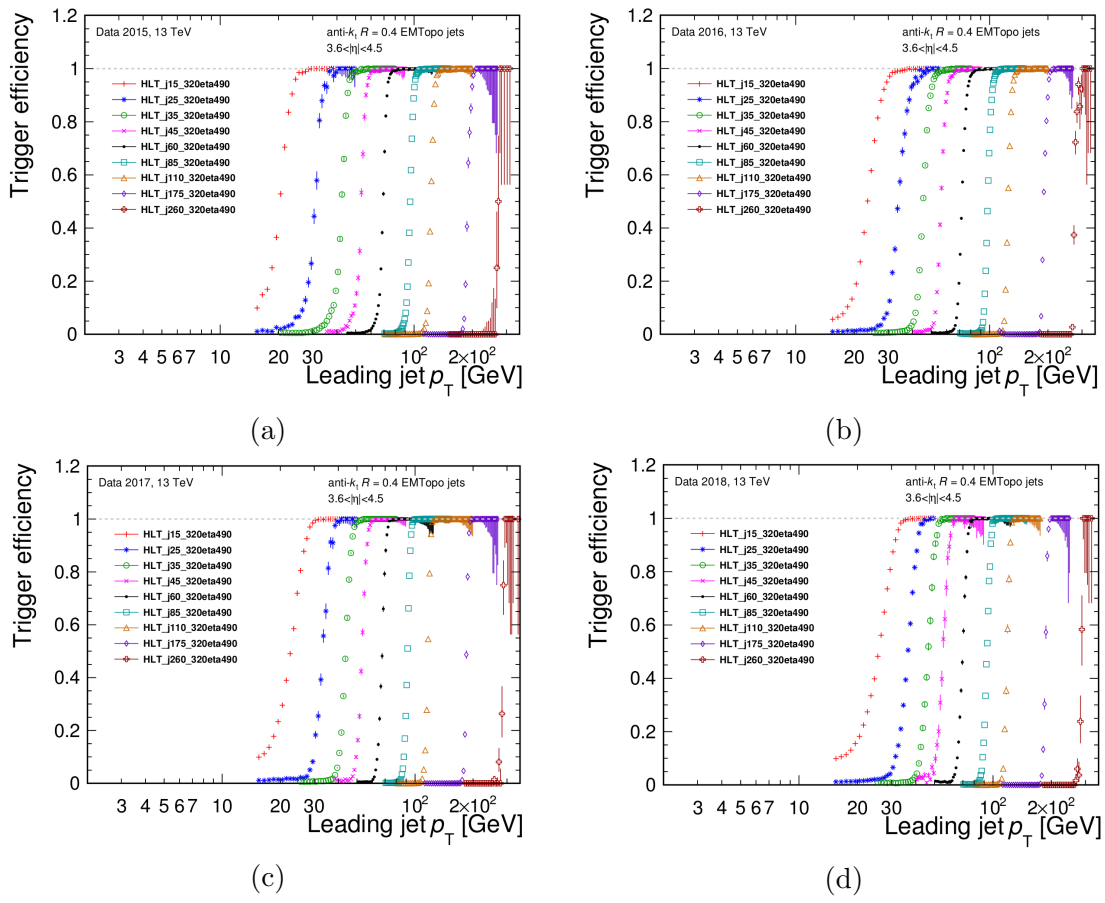

Figure 4.8: The full set of single forward jet ($3.2 < |\eta| < 4.9$) HLT trigger efficiency curves active in 2015 (a), 2016 (b), 2017 (c), and 2018 (d).

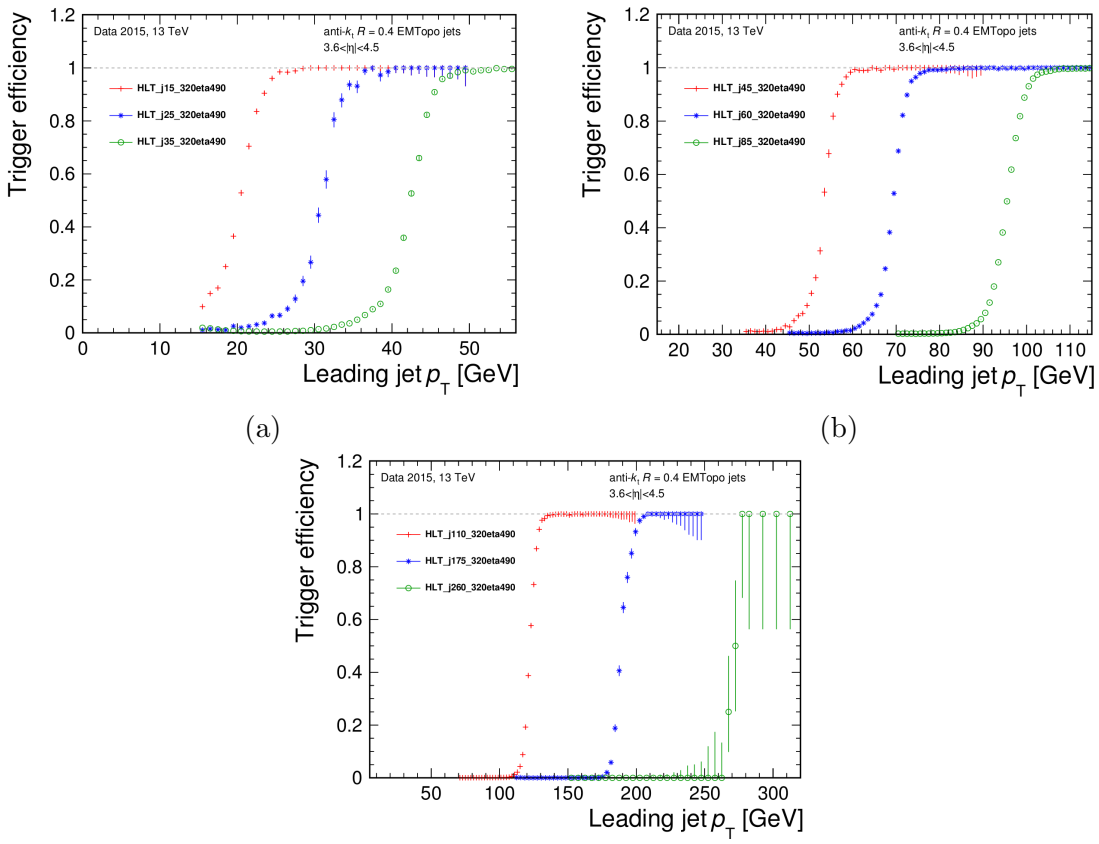

Figure 4.9: A zoomed-in view of the efficiency curves depicted in Figure 4.8a showing the lower-p_T (a), mid-p_T (b), and high-p_T (c) ranges of the 2015 single forward jet triggers.

As the name implies, the HLT forward jet triggers fire on jets detected in the high-η region ($3.2 < |\eta| < 4.9$) of the ATLAS detector. This region typically experiences a very high event rate due to high numbers of glancing collisions that send collision products to the region of the detector nearest to the beamline, which necessitates restrictive prescaling of the forward jet triggers. Additionally, this region sees a large background of low p_T jets, and, without the ability to use tracking information in this

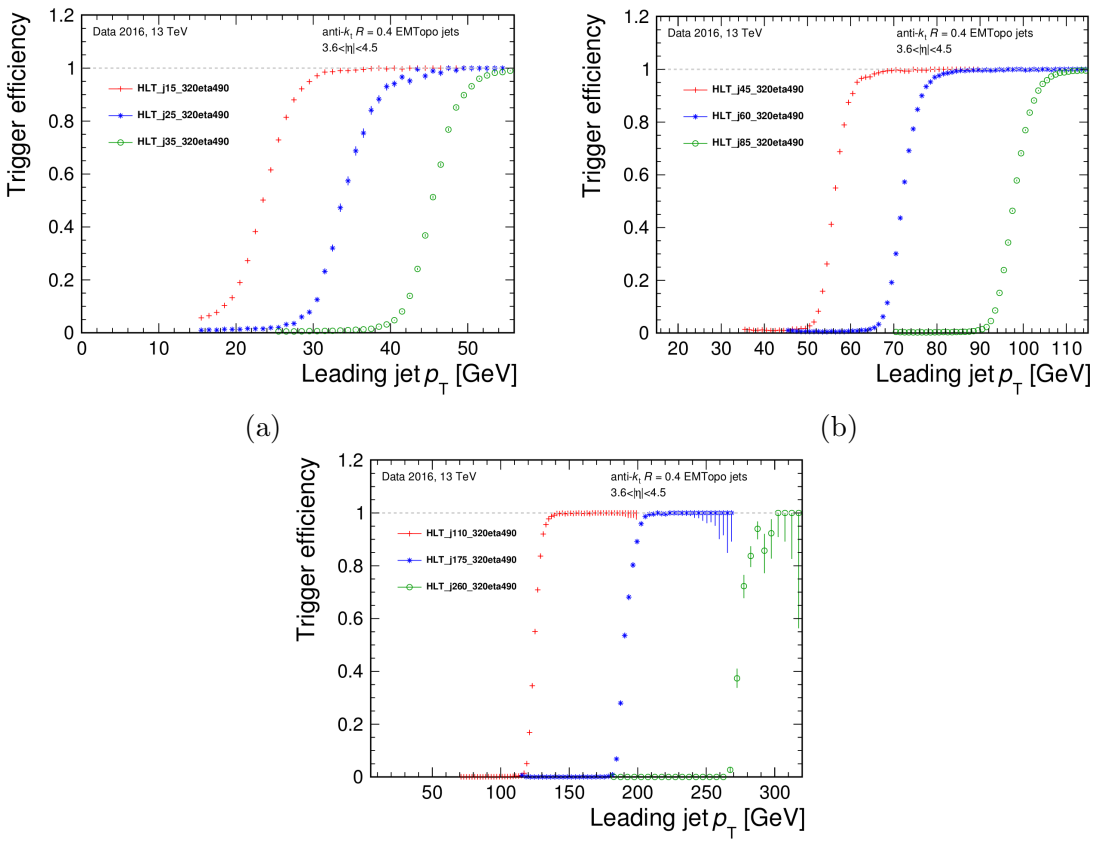

Figure 4.10: A zoomed-in view of the efficiency curves depicted in Figure 4.8b showing the lower-p_T (a), mid-p_T (b), and high-p_T (c) ranges of the 2016 single forward jet triggers.

η range, is very susceptible to the effects of pileup. Both of these factors contribute to a decrease in jet trigger efficiency of the forward jet triggers relative to their central jet equivalents.

As evidenced by the non-negligible error bars seen in several of the forward jet trigger efficiency curves, some of these triggers are somewhat statistically limited. Those at the low range of p_T thresholds, like HLT_j15_320eta490 and HLT_j25_320eta490, are

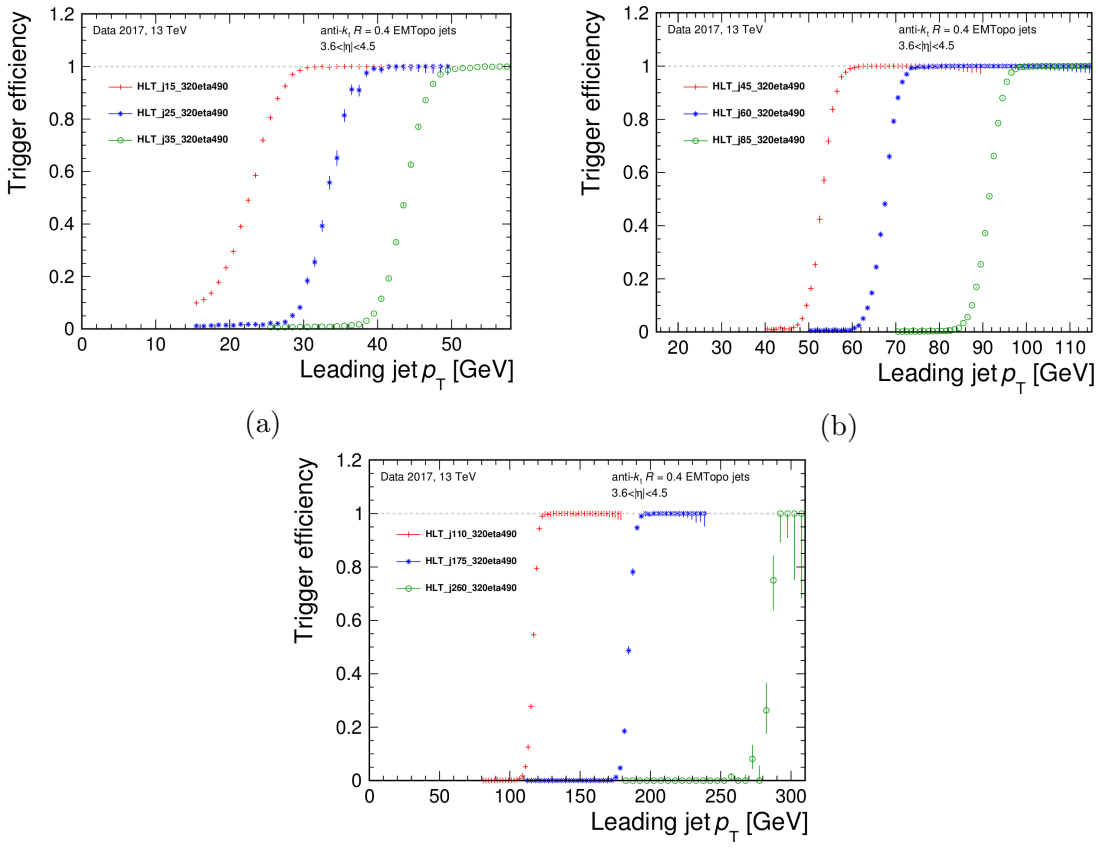

Figure 4.11: A zoomed-in view of the efficiency curves depicted in Figure 4.8c showing the lower-p_T (a), mid-p_T (b), and high-p_T (c) ranges of the 2017 single forward jet triggers.

limited by aggressive prescaling needed to conserve trigger bandwidth against the high event rate in the forward region. Conversely, despite being the lowest unprescaled forward jet trigger, the highest threshold forward jet trigger, HLT_j260_320eta490, has a very low event rate due to kinematic limitations. This is because it is very rare that a jet object has a high enough p_T to satisfy the 260 GeV trigger threshold while also having an η high enough to be found in the forward region.

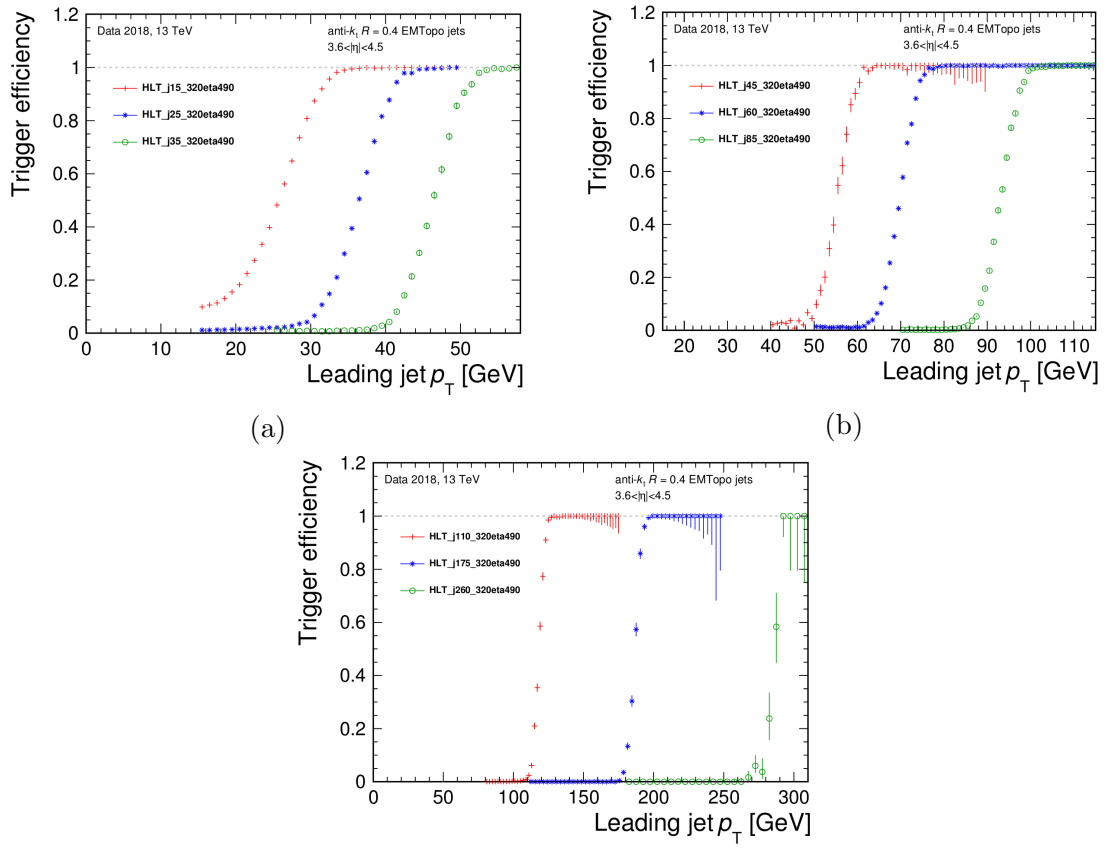

Figure 4.12: A zoomed-in view of the efficiency curves depicted in Figure 4.8d showing the lower-p_T (a), mid-p_T (b), and high-p_T (c) ranges of the 2018 single forward jet triggers.

Multi-Jet Triggers

Figure 4.13 shows the trigger efficiency curves for a selection of HLT multi jet triggers for 2015, 2016, 2017, and 2018. There are a large number of multi jet triggers active in the triggers menus for each year and the multi jet trigger criteria tended to be changed more often than in the case of the single jet triggers. This makes direct side-by-side comparison of the full sets of active multi jet triggers from year to year difficult. Instead, Figures 4.14, 4.15, 4.16, and 4.17 show only the efficiency curves for a selection of HLT_nj45 triggers with varying jet multiplicity requirements. The 45 GeV trigger threshold was chosen for this comparison because a number of triggers with different jet multiplicities and this threshold were active in each year.

As seen in Figure 4.13, the multi jet triggers active in Run 2 range from 3-jet to 10-jet triggers, encompassing a wide range of physics signals. Naturally, the higher the jet multiplicity required by the trigger criteria, the more room for mis-calibration of jets to negatively effect trigger efficiency. This is seen across the board, with 10j efficiency curves tending to have the widest turn-on region out of all of the multi jet triggers studied and the efficiency curves becoming sharper as the jet multiplicity trigger requirement decreases. The HLT_10j40 trigger in particular is found to be quite inefficient. This is due to the high jet multiplicity requirement and low p_T threshold making this trigger especially vulnerable to firing on jets resulting from pileup rather than those exclusively from hard-scattering events.

In the zoomed-in look at the HLT_nj45 efficiency curves plotted in Figures 4.14, 4.15, 4.16, and 4.17, some of the discussed behaviors are more clear. In each year, it is seen that the single jet HLT_j45 efficiency curve has the steepest turn-on, reaching its efficiency point at the lowest p_T value out of the various trigger jet multiplicities

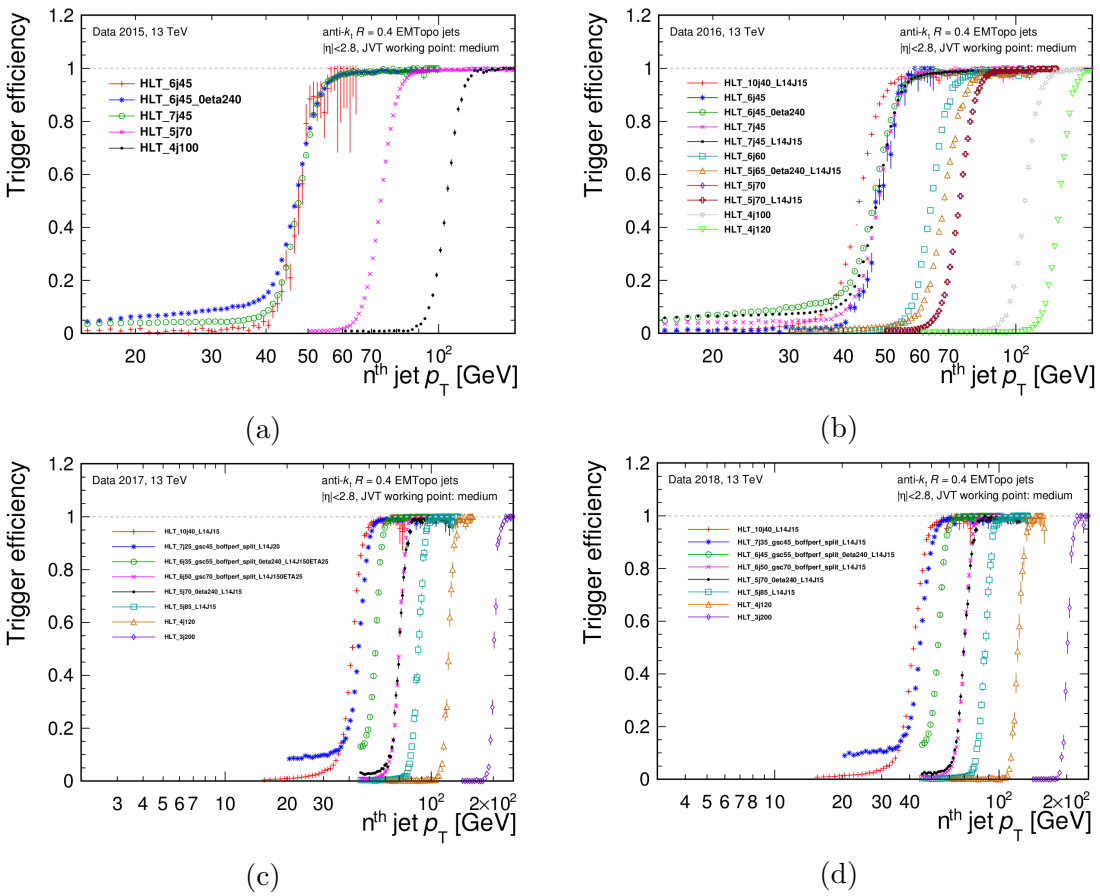

Figure 4.13: A selection of multi-jet HLT trigger efficiency curves active in 2015 (a), 2016 (b), 2017 (c), and 2018 (d). Note that more multi-jet triggers were active in each year that are not displayed here. Instead, the sets of triggers included here are intended to summarize the range of signatures covered by multi-jet triggers in each year. The x-axis shows the nth jet p_T, where n represents the jet multiplicity required by each trigger

shown. It is also more clearly seen in these plots that, as expected, the higher jet multiplicity triggers are less efficient as the multiplicity requirement increases, signified by the broader turn-on regions in their efficiency curves. Also displayed where possible is the HLT_7j45_L14J15 trigger, which is seeded by a multi jet L1 trigger. Only very minor differences are seen between the efficiencies of the HLT_7j45 and

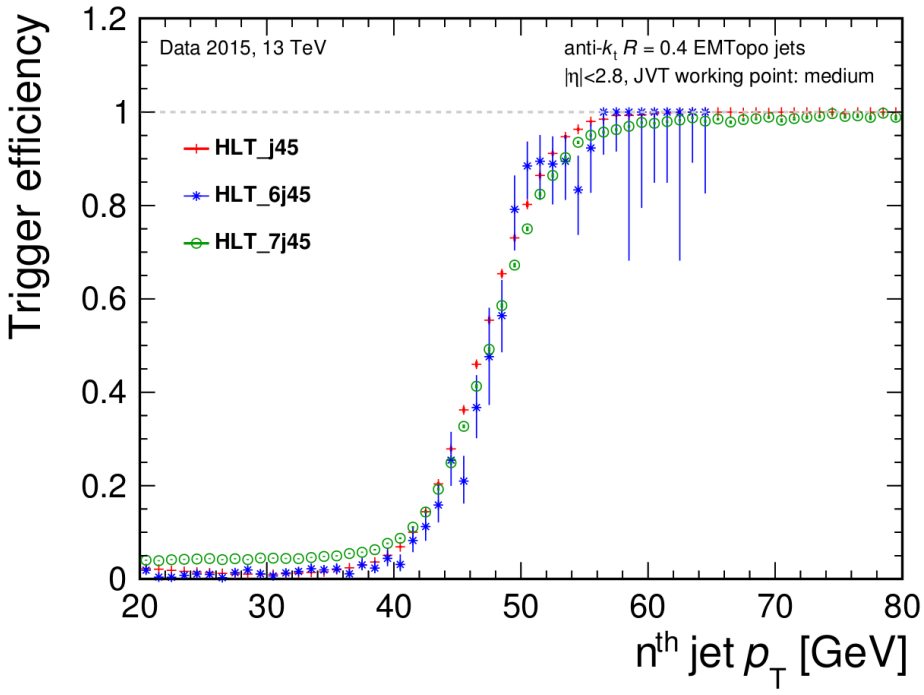

Figure 4.14: A zoomed-in look at the j45 triggers with varying jet multiplicity active in 2015. The x-axis shows the nth jet p_T, where n represents the jet multiplicity required by the trigger, i.e. HLT_nj45.

HLT_7j45_L14J15 triggers. Note that the statistics are limited for the HLT_6j45 trigger, as this was a prescaled trigger in the majority of the Run 2 data taking period. Where possible, an alternative 6j45 trigger efficiency curve with improved statistics is provided in the form of the η-restricted central 6j45 trigger HLT_6j45_0eta240.

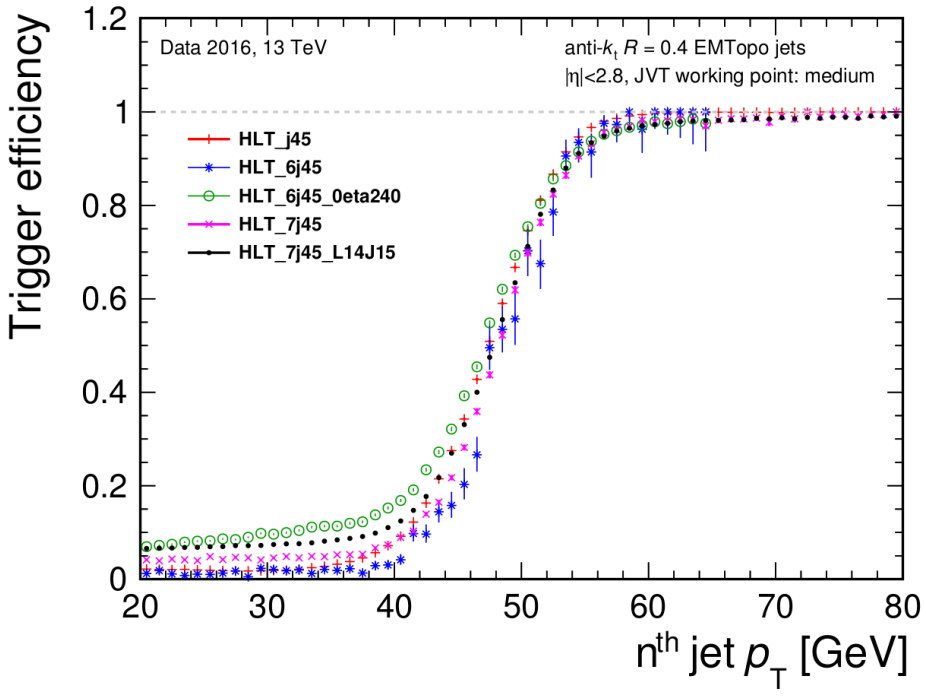

Figure 4.15: A zoomed-in look at the j45 triggers with varying jet multiplicity active in 2016. The x-axis shows the nth jet p_T, where n represents the jet multiplicity required by the trigger, i.e. HLT_nj45.

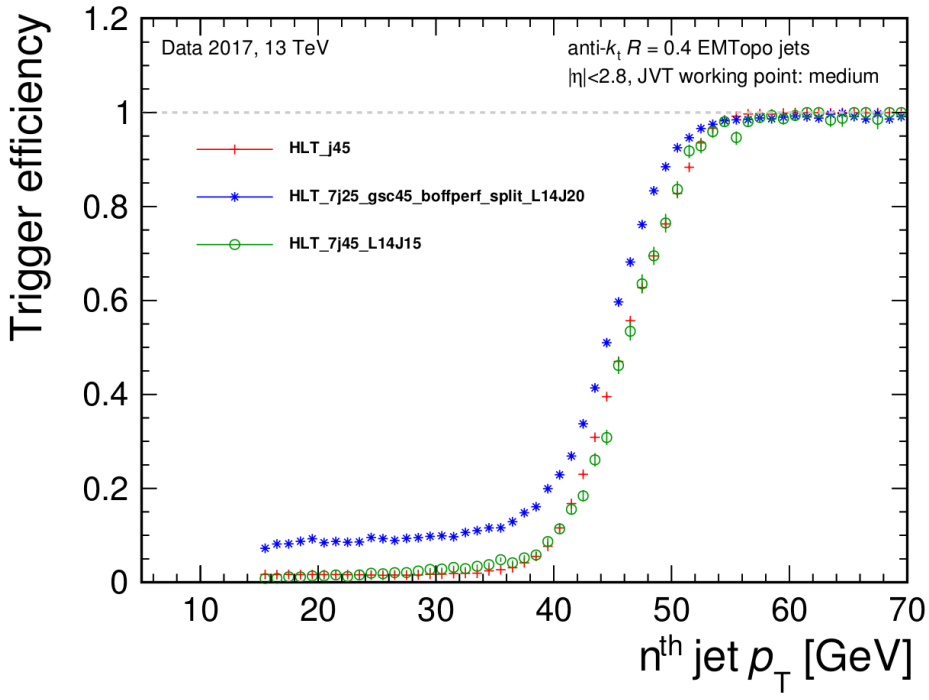

Figure 4.16: A zoomed-in look at the j45 triggers with varying jet multiplicity active in 2017. The x-axis shows the nth jet p_T, where n represents the jet multiplicity required by the trigger, i.e. HLT_nj45.

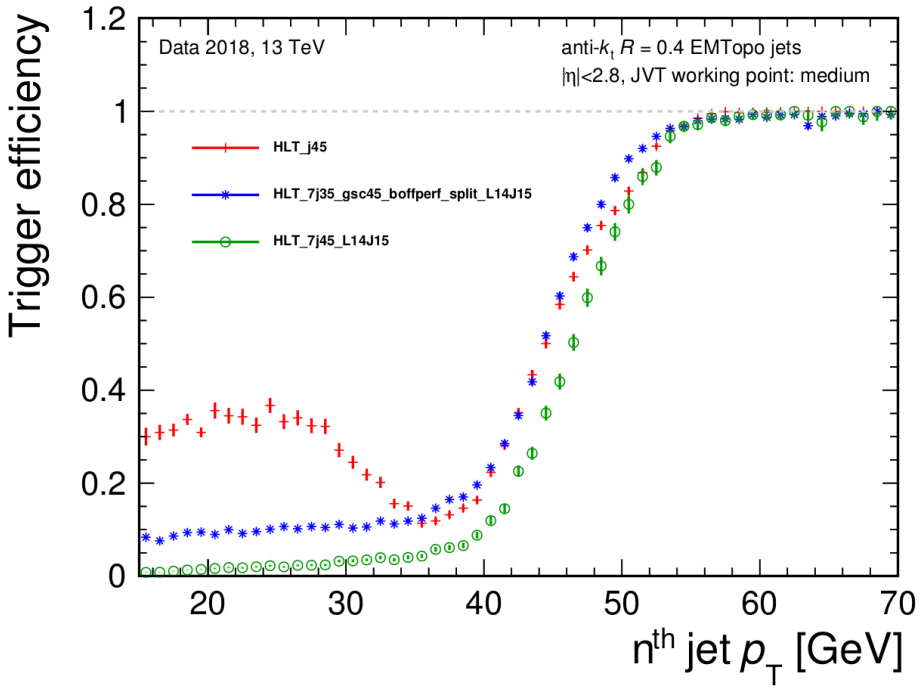

Figure 4.17: A zoomed-in look at the j45 triggers with varying jet multiplicity active in 2018. The x-axis shows the nth jet p_T, where n represents the jet multiplicity required by the trigger, i.e. HLT_nj45. The uncharacteristic uptick in the 2018 trigger turn-on curve is due to the threshold of the reference trigger being too close to that of the j45 trigger being analyzed, as discussed in Section 4.2.1.

Lowest Unprescaled Jet Triggers

As has been discussed, increasing luminosity over the duration of Run 2 necessitated increasing jet trigger prescaling. Side-by-side comparison of the efficiency curves for the lowest unprescaled jet triggers from each year give very useful perspective regarding the changes to the jet trigger menu forced by the increasing LHC luminosity over the course of Run 2. By comparing the lowest unprescaled triggers from each year, it an be directly seen how the p_T threshold for the collection of jet events without the negative effects of prescaling has increased throughout Run 2. These comparisons highlight challenges faced in terms of collecting data to be used for physics analyses requiring jets, especially those preferring lower p_T thresholds, as the LHC run conditions evolve.

Figures 4.18 and 4.19 show the evolution of the efficiencies of the lowest unprescaled triggers for the HLT single jet triggers and an example multi jet trigger, respectively, across Run 2. Additionally, a comparison of the trigger efficiency of the HLT_j45 single jet trigger is also included in Figure 4.20. While not an unprescaled trigger, it is useful to include an inter-year comparison of a trigger that maintains consistent trigger requirements from year to year, allowing for a direct look at how changing run conditions effect jet trigger efficiency.

The lowest unprescaled HLT single jet triggers, compared against each other in Figure 4.18, increased p_T trigger thresholds in each year of Run 2 data taking to conserve trigger bandwidth as the LHC luminosity, and therefore the event rate, increased. The lowest unprescaled trigger thresholds increased from 360 GeV in 2015, to 380 GeV in 2016, to 400 GeV in 2017, to 420 GeV in 2018. This is an unfortunate side effect of increasing luminosity. While the discovery power of detecting

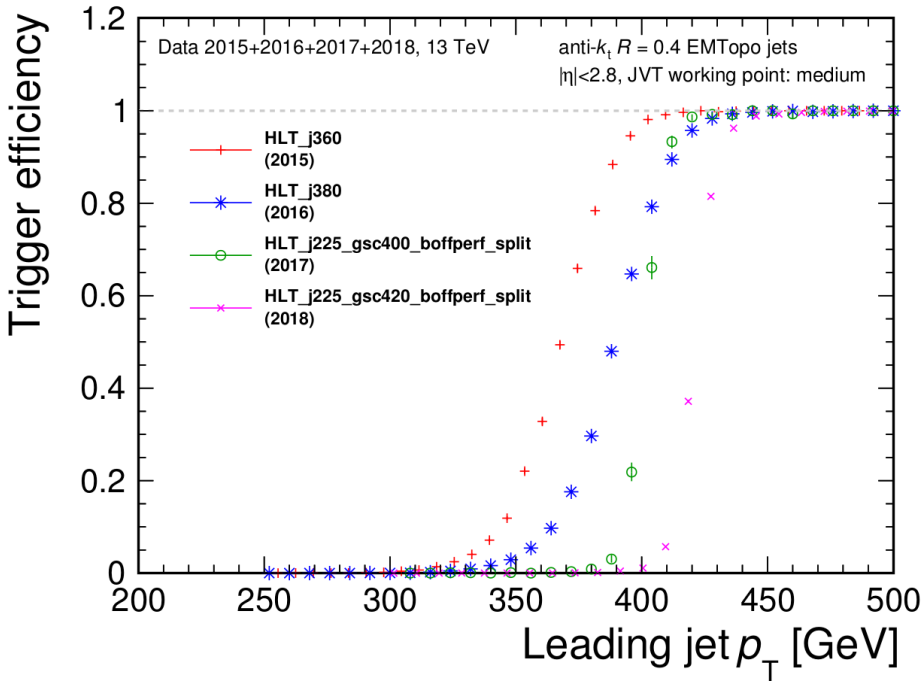

Figure 4.18: An inter-year comparison of the lowest unprescaled single jet trigger efficiency curves from each year of Run-2 data taking. Note that the lowest unprescaled trigger changes from year to year, going from HLT_j360 to HLT_j380 to HLT_j420 in 2015, 2016, and 2017/2018, respectively.

ultra-rare physics processes is increased as a result of the increased event rate, the sensitivity to lower-p_T regions suffers due to the need for more restrictive precaling. Note that the 2017 and 2018 triggers analyzed here have the full global sequential calibration (including tracking information) applied, as is the ATLAS trigger group recommendation.

One way to at least partially counteract the drop in sensitivity caused by the increased p_T thresholds of the lowest unprescaled triggers is to sharpen the trigger turn-on regions through improved calibration methods. Between the 2016 and 2017 data taking periods, the HLT jet calibration scheme was improved with the addition

of the Global Sequential Calibration and In-Situ calibration steps (both previously discussed in detail in Chapter 3). The positive effects of these calibration improvements are readily apparent in the efficiency curves shown in Figure 4.18 in that the efficiency curves for the 2017 and 2018 lowest unprescaled triggers have steeper turn-on regions, allowing these triggers to reach their efficiency points at lower p_T values. Thanks to the improvements to the calibration scheme, the 2017 lowest unprescaled single jet trigger is seen to reach full efficiency at a lower p_T than its 2016 counterpart, despite the latter performing in lower luminosity run conditions and having a trigger threshold lower by 20 GeV. The effects of each stage of the HLT jet calibration sequence will be examined further later in this section.

Figure 4.19 examines the lowest unprescaled triggers for the 4j multi jet trigger in each year of Run 2. As with the single jet unprescaled triggers, the p_T thresholds for these triggers were increased in each year of data taking to conserve trigger bandwidth in changing run conditions, causing the fully efficient regions for unprescaled data collection to begin at higher and higher p_T ranges. The lowest unprescaled 4j multi jet triggers required p_T thresholds of 85 GeV, 100 GeV, and 120 GeV in 2015, 2016, and 2017/2018, respectively. Multi jet triggers are typically more susceptible to pileup and mis-calibration than single jet triggers, causing the turn-on regions of these efficiency curves to be wider. The 2017 and 2018 run conditions and trigger menu were similar, so it is to be expected that their efficiency curves look similar here.

As the lowest unprescaled triggers in each year generally do not have a consistent p_T threshold, they do not give the clearest view of the direct effects of the changes in run conditions between years on the jet trigger performance. For this, it is useful to select a trigger that was active in each year of Run 2 data taking. Figure 4.20 shows

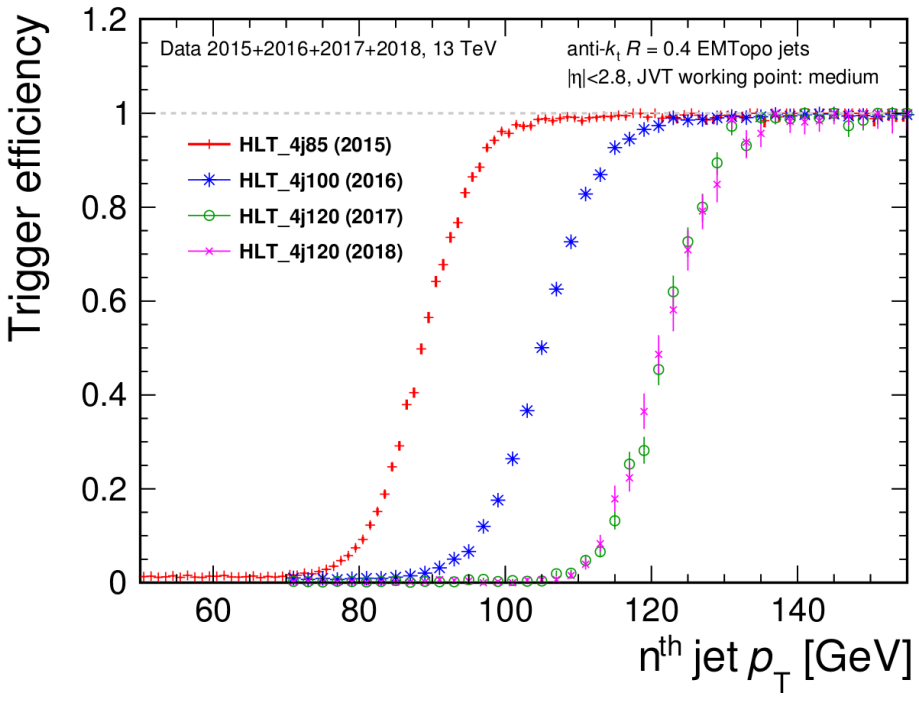

Figure 4.19: An inter-year comparison of the lowest unprescaled 4j multi-jet trigger efficiency curves from each year of Run-2 data taking. Note that the lowest unprescaled 4j trigger changes from year to year, going from HLT_4j85 to HLT_4j100 to HLT_4j120 in 2015, 2016, and 2017/2018, respectively. The 4j multi-jet trigger was chosen as a benchmark for comparing the trigger efficiency of the lowest unprescaled multi-jet triggers from each year.

one such trigger, HLT_j45, for each year. Here, the net effects of the changes in LHC luminosity, and therefor pileup, and the improvements in the jet calibration sequence can be seen. Note that the bump seen at the low-p_T tail of the 2018 curve is due to the reference trigger used to produce the efficiency curve not being fully efficient yet in this region, an effect previously discussed in Section 4.2.1.

As discussed, the LHC luminosity increased each year during Run 2, causing the amount of pileup interactions to increase as well. For this reason alone, it would be

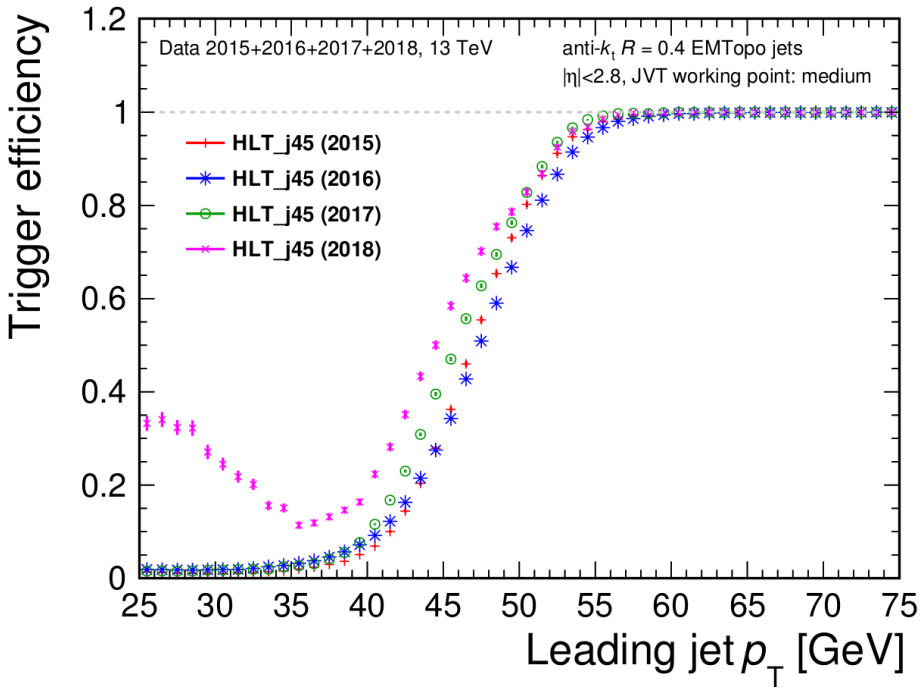

Figure 4.20: An inter-year comparison of the HLT_j45 jet trigger efficiency curves from each year of Run-2 data taking. This trigger was selected as a benchmark for comparing the relative trigger efficiency from year to year. The uncharacteristic uptick in the 2018 trigger turn-on curve is due to the threshold of the reference trigger being too close to that of the j45 trigger being analyzed, as discussed in Section 4.2.1.

expected that the jet trigger performance would be best in the lower pileup environment of 2015 and progressively diminish as the average pileup increases. However, as has also been discussed, the improved jet calibrations at the HLT level can help counteract this loss of performance by improving trigger efficiency. These effects are observed in Figure 4.20. It is seen that the efficiency curve is slightly sharper for 2015 data than 2016 data due to lower average pileup conditions, but the improved calibration scheme implemented starting in 2017 sharpens the turn-ons enough to counter the loss in efficiency due to increased pileup in the later years of Run 2. The effects

of each stage of the HLT jet calibration chain on trigger efficiency are investigated further in the next section.

Calibration Effects on Jet Trigger Efficiency

The final set of jet trigger efficiency curve comparisons discussed here show the effects of the various stages of the jet trigger calibration scheme. Rather than comparing the same triggers between years or different triggers within the same year, Figures 4.21 through 4.26 compare identical triggers with different stages of the HLT jet calibration chain applied. All of these figures were made using data collected during the 2017 data-taking period, as the jet calibration scheme was updated prior to this period. As discussed in depth in Chapter 3, the major changes made to improve the jet calibration chain at the HLT level were the additions of the GSC and in-situ calibration steps. The figures presented here aim to show the improvements to jet trigger efficiency gained from these calibrations through the direct comparison of the efficiency curves with each stage of the calibration chain applied, as well as comparing the various complete calibrations available in 2016 vs 2017/2018.

Figures 4.21, 4.23, and 4.25 show the trigger efficiency curves as calculated at each stage of the jet calibration chain for the HLT_j420, HLT_4j120, and HLT_7j45 triggers, respectively. All of these triggers were unprescaled in the 2017/2018 trigger menus. The stages of the full HLT jet calibration chain include the pileup, constituent, EtaJES, GSC (version with and without tracking information are available), and in-situ scales (see Chapter 3 for descriptions of the various calibration stages). As expected, each subsequent calibration step serves to narrow the trigger turn-on region and improve the trigger efficiency points, with the HLT_j225_gsc420_boffperf_split trigger efficiency curve clearly having the steepest rise to full efficiency. Note that the

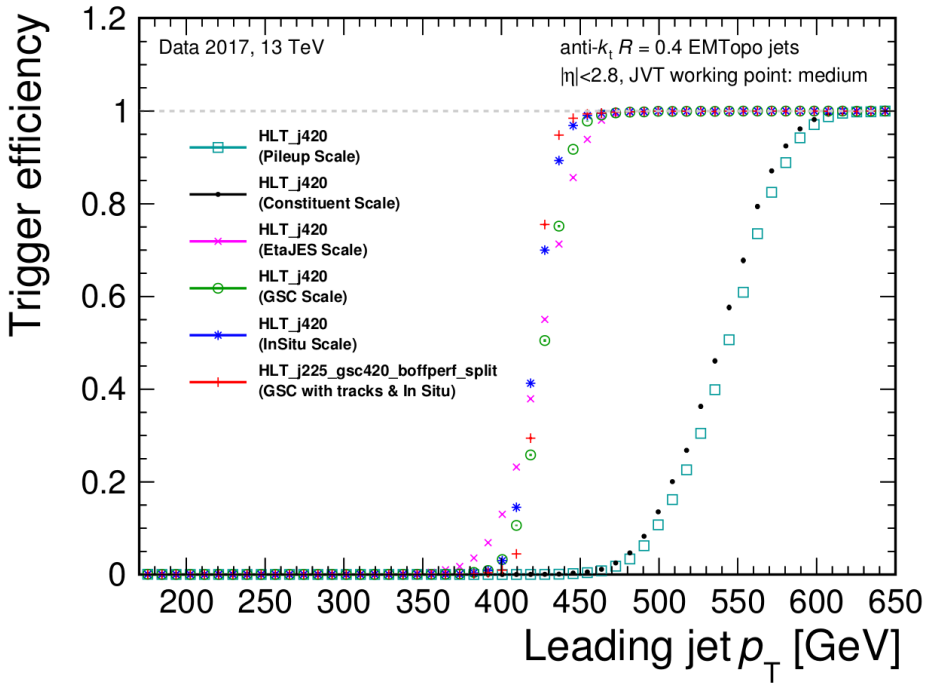

Figure 4.21: A comparison of the lowest unprescaled single jet trigger efficiency curves in 2017/2018 (HLT_j420) at each stage of the jet calibration chain. Data shown here is from the 2017 data-taking period only, as this is when the updated jet calibration scheme went into effect. 2018 data is not shown, but is expected to behave similarly as it relied on the same calibration scheme.

HLT_jX_gscX_boffperf_split triggers have the same trigger threshold as the others in the respective comparison plots, but include the full GSC with tracking information calibration and are thus the ATLAS trigger group recommendation for use when available. While these results do not yield any surprising conclusions, they do serve as satisfying evidence that the stages of the jet calibration scheme are each doing their part to improve the efficiency of the collection of data involving jet objects.

Figures 4.22, 4.24, and 4.26 show calibration scale comparisons for only the calibration steps added prior to the 2017 data taking period for the HLT_j420, HLT_4j120,

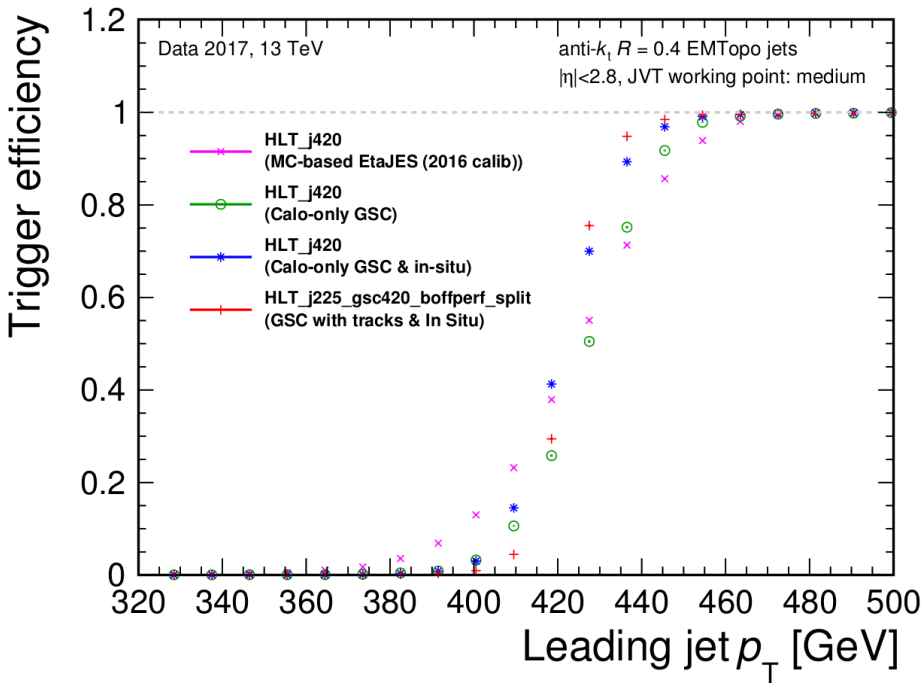

Figure 4.22: A comparison of the lowest unprescaled single jet trigger efficiency curves in 2017/2018 (HLT_j420), explicitly showing the effects of the additional calibrations added prior to data collection in 2017. Data shown here is from the 2017 data-taking period only, however a curve showing the 2016 calibration scheme applied to the 2017 data is shown for comparison. The calibration stages shown here include through the Jet Energy Scale calibration (the full 2016 calibration), with the trackless (calorimeter input only) GSC calibration step added, with the trackless GSC and in-situ calibration steps added, and with the full GSC calibration with tracks and in-situ steps added (the full, optimal 2017/2018 calibration).

and HLT_7j45 triggers, respectively. These plots serve as a zoomed-in view of the full calibration scale comparisons and help put into perspective the improvements made through refinement of the HLT jet calibration. While a very significant improvement can be seen in these triggers between the 2016 calibration and the recommended full 2017/2018 calibration, it is clear that any further calibration improvements could lead to sharper trigger efficiency curves and therefore increased data collection efficiency.

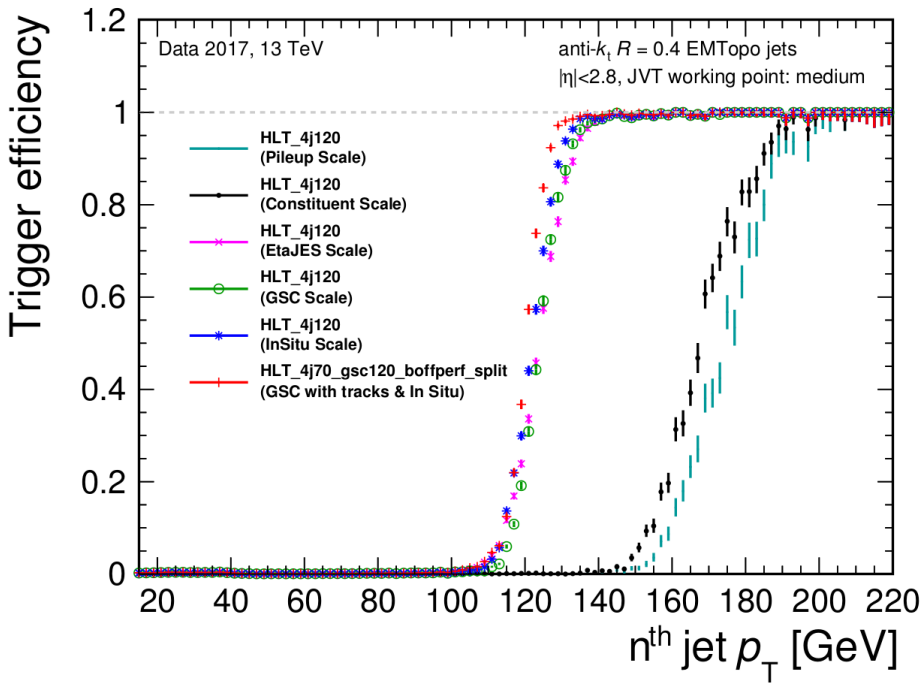

Figure 4.23: A comparison of the lowest unprescaled 4j multi-jet trigger efficiency curves in 2017/2018 (HLT_4j120) at each stage of the jet calibration chain. Data shown here is from the 2017 data-taking period, when the updated jet calibration scheme went into effect. 2018 data is not shown, but is expected to behave similarly as it relied on the same calibration scheme.

Continued analysis and development of further trigger-level jet calibration improvements will be extremely important as the LHC continues to run, especially at the higher and higher luminosities planned for future Run 3 operation.

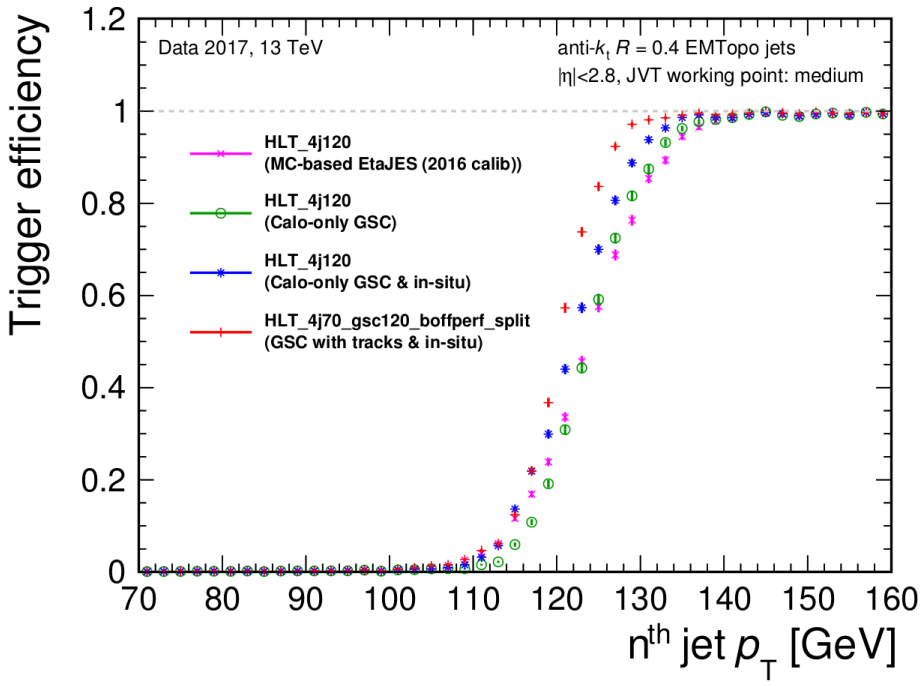

Figure 4.24: A comparison of the lowest unprescaled 4j multi-jet trigger efficiency curves in 2017/2018 (HLT_4j120), explicitly showing the effects of the additional calibrations added prior to data collection in 2017. Data shown here is from the 2017 data-taking period only, however a curve showing the 2016 calibration scheme applied to the 2017 data is shown for comparison. The calibration stages shown here include through the Jet Energy Scale calibration (the full 2016 calibration), with the trackless (calorimeter input only) GSC calibration step added, with the trackless GSC and in-situ calibration steps added, and with the full GSC calibration with tracks and in-situ steps added (the full, optimal 2017/2018 calibration).

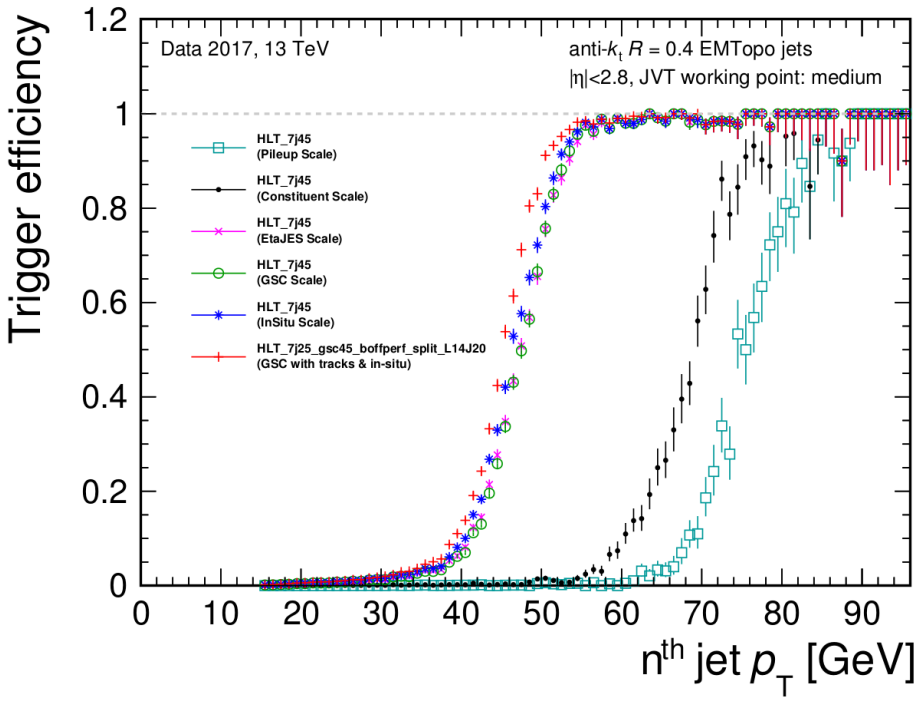

Figure 4.25: A comparison of the lowest unprescaled 7j multi-jet trigger efficiency curves in 2017/2018 (HLT_7j45) at each stage of the jet calibration chain. Data shown here is from the 2017 data-taking period, when the updated jet calibration scheme went into effect. 2018 data is not shown, but is expected to behave similarly as it relied on the same calibration scheme.

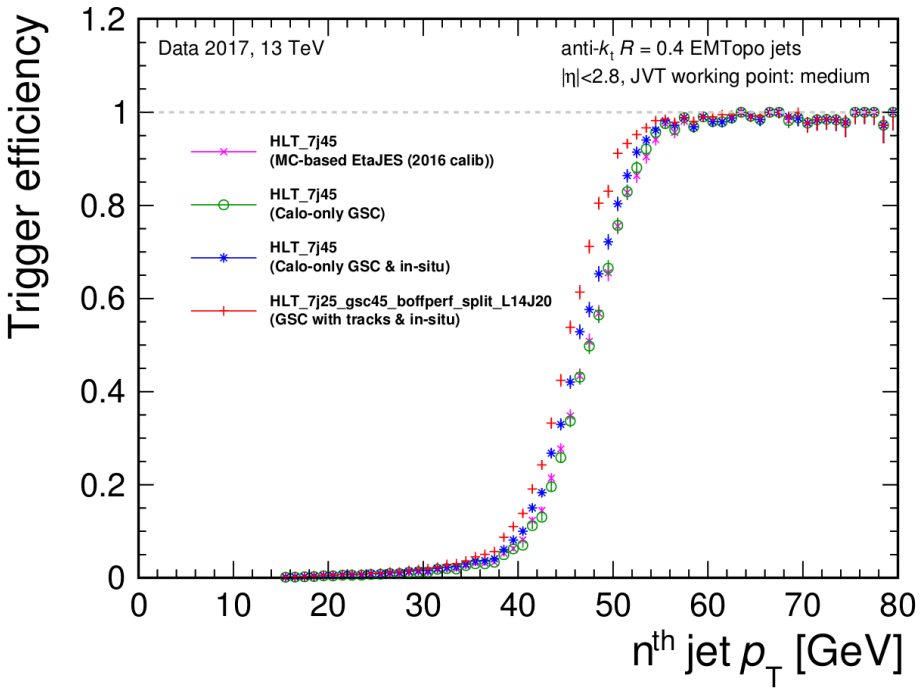

Figure 4.26: A comparison of the lowest unprescaled 7j multi-jet trigger efficiency curves in 2017/2018 (HLT_7j45), explicitly showing the effects of the additional calibrations added prior to data collection in 2017. Data shown here is from the 2017 data-taking period only, however a curve showing the 2016 calibration scheme applied to the 2017 data is shown for comparison. The calibration stages shown here include through the Jet Energy Scale calibration (the full 2016 calibration), with the trackless (calorimeter input only) GSC calibration step added, with the trackless GSC and in-situ calibration steps added, and with the full GSC calibration with tracks and in-situ steps added (the full, optimal 2017/2018 calibration).

4.3 Jet Trigger Impacts On Data

The analysis presented in the previous section showed in great detail how the jet triggers performed under evolving data-taking conditions throughout LHC Run 2 in terms of trigger efficiency. In order to further contextualize the trigger performance and visualize how the various changes in trigger efficiency effect the quality of data collected, further analysis was performed to show the fraction of "useful" data that has passed the jet triggers and been written to disk.

So called "useful" data refers to collision events that are written to disk after not only passing a jet trigger, but also having a fully-calibrated trigger jet p_T that falls in an acceptably efficient region of the trigger efficiency curve. This is in contrast to events that have trigger jet p_T values large enough to satisfy the trigger threshold but low enough that they lie in the trigger turn-on region of the efficiency curve. The former constitutes data that is usable for further analyses like searches for signals of new physics or precision measurements of known processes, while the latter is trimmed away for analyses relying on a specific trigger signature. This again emphasizes the importance on the triggers performing as efficiently as possible, as the steepness of the efficiency curves has a direct impact on the fraction of useful data collected with a given trigger.

The single jet triggers (HLT_jX) were analyzed to show the fraction of useful data collected in each year of Run 2 data taking. This analysis, shown in Figures 4.27 through 4.30, plots the full spectra of offline leading jet p_T from each event that satisfied at least one active single jet trigger and identifies the subset of these events with leading jet p_T values that fall in the efficient regions of the respective jet trigger efficiency curves. So as to avoid double-counting of events in this analysis, each event

is only considered once in the offline leading jet p_T histogram, with events being associated with the highest trigger threshold that they satisfy. For example, an event with a leading jet p_T of 300 GeV would be treated as having passed the HLT_j260 trigger but not the HLT_j175 trigger.

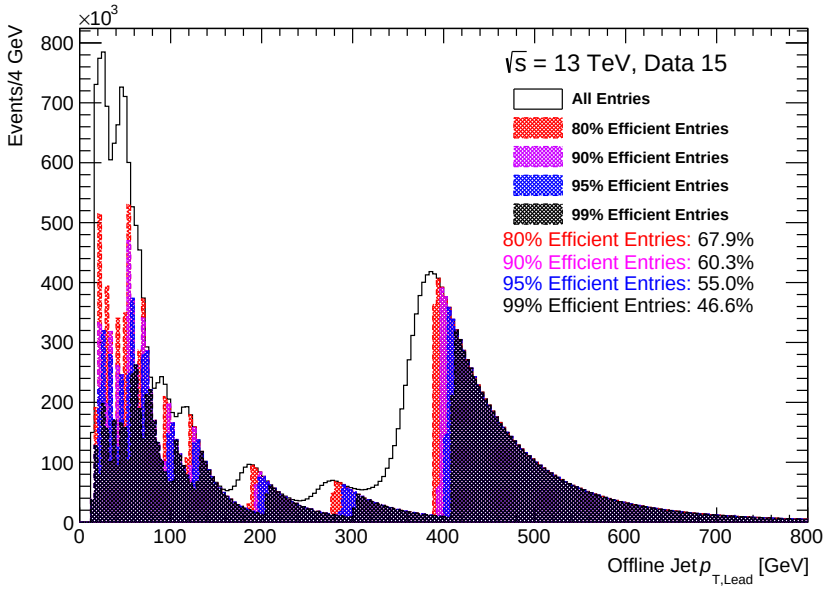

Figure 4.27: The offline leading jet p_T for all events passing a minimum of one single jet trigger (HLT_jX) in 2015 data. Shaded regions indicate where the single jet triggers satisfy a specified efficiency threshold and therefor the regions where the data may be safe to use in further physics analyses. This analysis uses the 80% (red), 90% (violet), 95% (blue), and 99% (black) efficiency points.

For each trigger, four efficiency point thresholds were chosen as benchmarks- 80%, 90%, 95%, and 99%. The efficiency points for each trigger were calculated from their respective trigger efficiency curves as the first point after which all subsequent points on the curve fall above the given efficiency threshold. This method approximates the

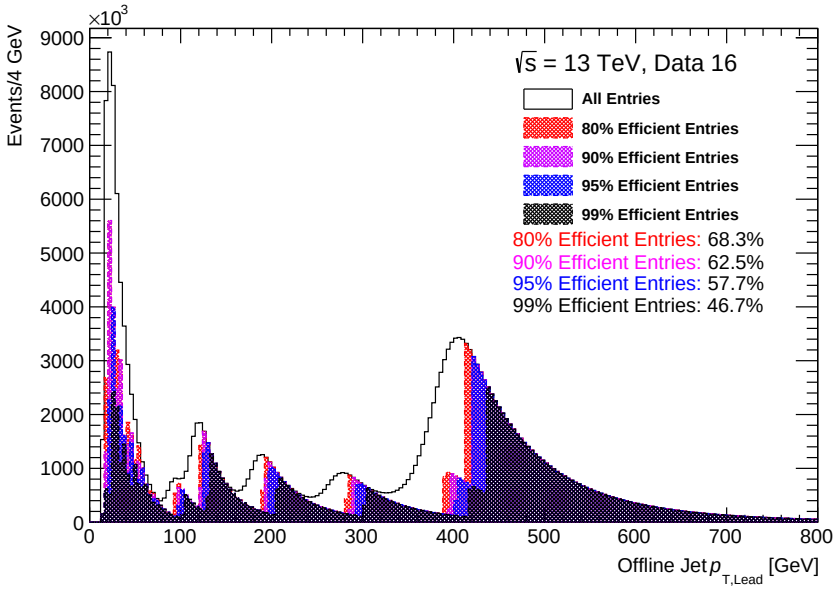

Figure 4.28: The offline leading jet p_T for all events passing a minimum of one single jet trigger (HLT_jX) in 2016 data. Shaded regions indicate where the single jet triggers satisfy a specified efficiency threshold and therefor the regions where the data may be safe to use in further physics analyses. This analysis uses the 80% (red), 90% (violet), 95% (blue), and 99% (black) efficiency points.

trigger efficiency points to an accuracy dependant on the binning of the efficiency curves, which is typically 1-3 GeV per bin, depending on the curve. The trigger efficiency points calculated from the efficiency curves are listed in Table 4.3.

The offline leading jet p_T spectra plotted in Figures 4.27 through 4.30 exhibits a distinctive sawtooth shape where local maxima are seen at p_T values where individual triggers go into effect. The magnitude of these peaks varies due to both the event rate of a given trigger and the degree of prescaling applied. The lower-p_T triggers have a very large event rate even after prescaling, leading to a large number of events written to disk, as seen in high number of entries in the left-most maxima in the

	80% Eff. Pt. (GeV)	90% Eff. Pt. (GeV)	95% Eff. Pt. (GeV)	99% Eff. Pt. (GeV)
2015				
HLT_j15	19.5	21.5	22.5	25.5
HLT_j25	29.5	31.5	32.5	35.5
HLT_j35	40.5	41.5	43.5	45.5
HLT_j45_L1RD0_FILLED	50.5	52.5	54.5	57.5
HLT_j60_L1RD0_FILLED	66.5	68.5	69.5	73.5
HLT_j85	92.5	95.5	97.5	103.5
HLT_j110	119.0	123.0	125.0	131.0
HLT_j175	187.5	193.5	196.5	205.5
HLT_j260	277.5	287.5	287.5	302.5
HLT_j360	388.5	395.5	402.5	409.5
2016				
HLT_j15	18.5	19.5	22.5	25.5
HLT_j25	30.5	31.5	33.5	36.5
HLT_j35	41.5	42.5	44.5	47.5
HLT_j45_L1RD0_FILLED	51.5	53.5	55.5	58.5
HLT_j60_L1RD0_FILLED	66.5	68.5	70.5	74.5
HLT_j85	93.5	96.5	98.5	103.5
HLT_j110	121.0	123.0	125.0	131.0
HLT_j175	190.5	193.5	196.5	205.5
HLT_j260	282.5	287.5	292.5	302.5
HLT_j360	388.5	395.5	402.5	416.5
HLT_j380	412.5	420.0	420.0	436.0
2017				
HLT_j15	14.5	16.5	17.5	20.5
HLT_j25	27.5	29.5	31.5	33.5
HLT_j35	39.5	41.5	43.5	45.5
HLT_j45_L1RD0_FILLED	50.5	52.5	53.5	55.5
HLT_j60_L1RD0_FILLED	65.5	66.5	68.5	70.5
HLT_j85	90.5	92.5	94.5	97.5
HLT_j110	117.0	119.0	121.0	123.0
HLT_j175	184.5	187.5	187.5	193.5
HLT_j260	267.5	272.5	277.5	282.5
HLT_j360	374.5	374.5	381.5	395.5
HLT_j420	436.5	436.5	445.5	454.5
2018				
HLT_j15	14.5	15.5	16.5	19.5
HLT_j25	26.5	29.5	31.5	34.5
HLT_j35	40.5	42.5	44.5	48.5
HLT_j45	50.5	52.5	53.5	56.5
HLT_j60	65.5	67.5	69.5	71.5
HLT_j85	90.5	93.5	94.5	97.5
HLT_j110	117.0	119.0	121.0	125.0
HLT_j175	184.5	187.5	190.5	193.5
HLT_j260	267.5	272.5	277.5	282.5
HLT_j360	374.5	374.5	381.5	395.5
HLT_j420	436.5	436.5	445.5	454.5

Table 4.3: Efficiency points for the various single jet triggers active in each year of Run 2 data collection as taken from the efficiency curves for each trigger.

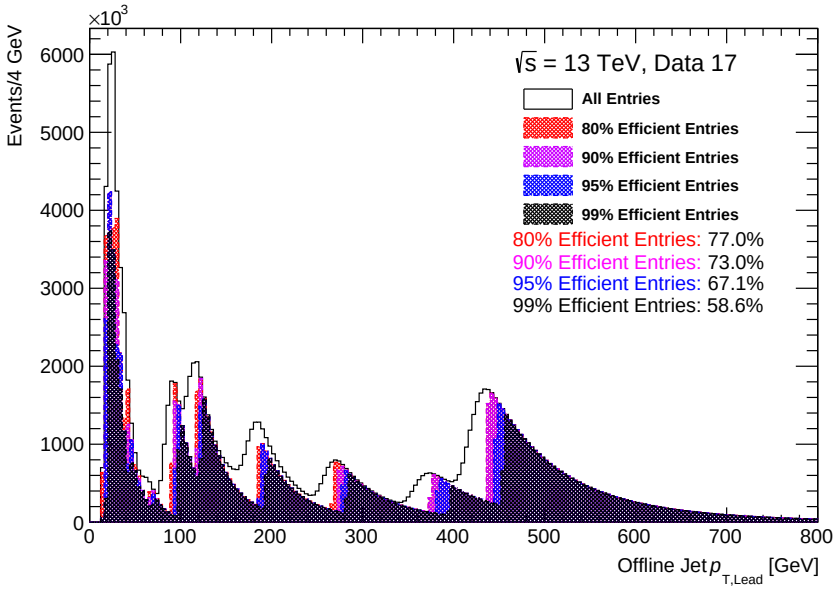

Figure 4.29: The offline leading jet p_T for all events passing a minimum of one single jet trigger (HLT_jX) in 2017 data. Shaded regions indicate where the single jet triggers satisfy a specified efficiency threshold and therefor the regions where the data may be safe to use in further physics analyses. This analysis uses the 80% (red), 90% (violet), 95% (blue), and 99% (black) efficiency points.

p_T spectra in each year. The number of entries in the low-p_T peaks of the spectra also appears very high due to the relatively small difference in trigger throsholds of the low-p_T triggers, which causes the peaks in the spectra from these triggers smear together in this more crowded p_T range. On the high-p_T end of the leading jet p_T spectra, the relatively high event rate of the lowest unprescaled triggers lead to the most significant peak in the p_T spectra in each year. This further shows the benefit of operating with no or minimal prescaling, as the difference in number of recorded events of these triggers is quite significant.

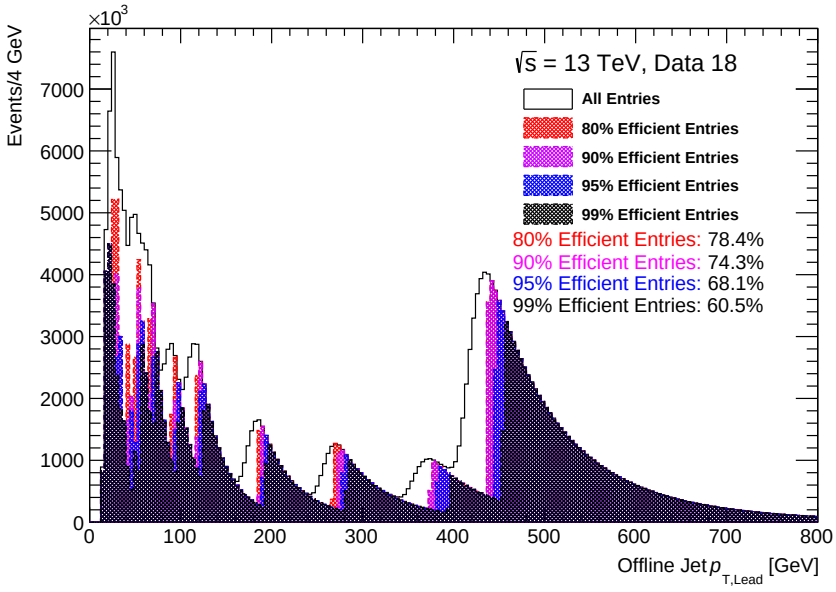

Figure 4.30: The offline leading jet p_T for all events passing a minimum of one single jet trigger (HLT_jX) in 2018 data. Shaded regions indicate where the single jet triggers satisfy a specified efficiency threshold and therefor the regions where the data may be safe to use in further physics analyses. This analysis uses the 80% (red), 90% (violet), 95% (blue), and 99% (black) efficiency points.

The percentage of useful data collected by the full set of single jet triggers analyzed in each year is calculated as the integral of the efficient events, represented by the shaded regions corresponding to each efficiency threshold analyzed, divided by the integral of the full leading jet p_T histogram. The resulting percentages of useful data recorded in each year are summarized in Table 4.4. The results show that a significant fraction of the data that satisfied the trigger requirements to be written to disk does not fall in the fully efficient range of the trigger that it passes. Logically, as the event rate increases very quickly as leading jet p_T decreases, it is unsurprising that a large fraction of events are recorded before the jet triggers become fully efficient.

Year	Efficient Data % (80%)	Efficient Data % (90%)	Efficient Data % (95%)	Efficient Data % (99%)
2015	67.9	60.3	55.0	46.6
2016	68.3	62.5	57.7	46.7
2017	77.0	73.0	67.1	58.6
2018	78.4	74.3	68.1	60.5

Table 4.4: The percentage of data collected using the full suite of single jet triggers that satisfies the listed trigger efficiency thresholds in each year.

A positive takeaway, however, is that the effects of the jet calibration improvements made prior to 2017 data collection (discussed in Section 4.2.2) are readily apparent, with the percentage of events saved satisfying the 99% trigger efficiency benchmark increasing from 46.6% to 60.5% from the start of Run 2 in 2015 to the end in 2018. This is evidence that the slight sharpening of the turn-on region of the trigger efficiency curves gained as a result of the improved jet calibration scheme translates to a significant improvement in the quality of data collected by the jet triggers. As even seemingly small improvements to the jet trigger efficiencies are seen to translate to much more effective data collection, these results should serve to motivate work towards further improvements on the jet trigger and calibration systems.

4.4 Future Perspectives

As the analysis presented in this chapter has shown, effective data collection relies on maximally efficient triggers and effective calibration schemes to identify and save the most impactful physics data. With the upcoming LHC Run 3 and the run conditions continuing to evolve into the High Luminosity LHC era, these considerations will remain as important as ever. As was evident throughout the course of Run 2, increasing luminosity comes with unavoidable challenges caused by increased pileup-induced backgrounds, especially when it comes to detecting jet signatures. Thankfully, it has been seen that these issues may be at least partially counteracted through improvements to the jet calibration scheme that work to keep the jet triggers performing efficiently.

One of the prominent avenues for potential improvement to the jet trigger efficiency in the future is through increased trigger-level tracking capabilities. It is clear when analyzing the performance of the Run 2 jet calibration scheme (Figures 4.21-4.26) that the addition of tracking information leads to significant improvement to jet trigger performance. Extrapolating this behavior out, it is reasonable to imagine that increased computing resources that allow for more effective particle tracking at the trigger level will be a very useful tool for further development of improved trigger and calibration techniques. The results presented in this chapter have shown that incremental improvements to the jet trigger efficiency can have significant impacts on the quality of data recorded for future analysis, and further improvements will be integral to maximizing the discovery power of ATLAS going forward.

Chapter 5: Search for New Physics with Dijet Trigger Level Analysis

The previous chapters have extensively discussed the methods used in ATLAS to reconstruct, calibrate, and record data containing hadronic jet objects, as well as presented an analysis of the full Run 2 jet trigger menu done to investigate the efficiency of the jet triggers and the quality of the jet data that was saved throughout Run 2. In this chapter, a dijet Trigger Level Analysis (TLA)[29] that directly makes use of the trigger-level jet objects previously introduced to search for new physics in the dijet final state will be discussed.

Analysis of the full Run 2 data set is currently underway. In lieu of these results, this chapter focuses on the results of the dijet TLA using a partial Run 2 data set that includes 36 fb^{-1} of data recorded through the 2016 data-taking period. Contributions to the full Run 2 dijet TLA, which uses an approximately four times larger data set, are highlighted, including end-of-fill data collection and data preparation, quality checks, and cleaning.

5.1 Dijet Searches And Trigger Level Analysis Motivation

Dijet analyses search for new physics by utilizing the idea that any new particles produced in proton-proton collisions must interact with the partons making up the

proton, and thus may also decay back into these partons. Such a decay would be detectable as a pair of hadronic jets in the final state. Standard Model predictions call for a smoothly falling distribution of dijet invariant mass reconstructed from the two highest p_T jets in the final state. Any new physics would deviate from these predictions and present itself as a bump in the dijet invariant mass distribution. Thus, a common search strategy for new physics phenomena at hadron colliders is to reconstruct the dijet invariant mass spectrum from collision events that produce two high p_T jets and probe it for anomalous bumps that could indicate the presence of BSM phenomena.

Standard dijet analyses are statistically limited at lower mass ranges due to jet trigger prescaling, discussed extensively in previous chapters, which limits the number of events that can be collected for analysis. This in turn limits the strength of limits that may be set on extremely rare processes, as larger numbers of events are required to rule out smaller coupling values between SM particles and BSM physics. Increasing luminosity and collision energy, while increasing discovery power at higher masses, decreases sensitivity in the ranges where the triggers must be prescaled. This fact is borne out in Figure 5.1, which shows the upper limits of the coupling between quarks and a theoretical BSM Z' particle set by various collider experiments in past years. As is seen in this plot, despite advancements in collider and detector technologies, the oldest experiments shown, CDF and UA2, still set the strongest limits in the low mass region. This is due to their lower collision energies making these experiments more sensitive to lower dijet invariant mass ranges, as the aggressive jet trigger prescaling that limits trigger bandwidth allocation to triggers in this region at the LHC experiments was not present.

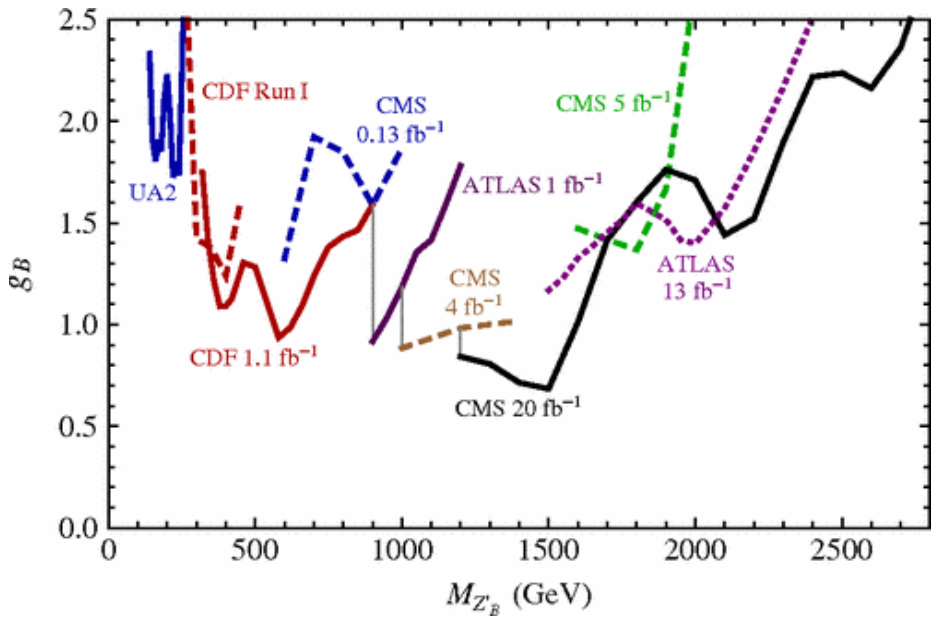

Figure 5.1: Limits set by various collider experiments on coupling g_B between quarks and a theoretical Z' particle as a function of the Z' mass. The regions above each contour are excluded, meaning that for a given value of Z' mass along the x-axis, coupling values above each curve have been ruled out by the experiment responsible for setting the limit [32]

.

Jet trigger prescaling restricts the amount of data that may be collected with low jet p_T triggers, making searching for rare BSM processes at lower dijet invariant mass ranges difficult. The dijet TLA provides a method to partially avoid these limitations, allowing for the dijet invariant mass spectrum to be studied at much lower mass ranges than are possible with a standard dijet analysis that relies on offline data. The TLA strategy uses a separate data collection stream that is independent of HLT triggers to save online trigger-level events that contain a fraction of the information of fully

reconstructed offline events. This data collection stream, the so-called data scouting stream, allows for events reconstructed at the HLT level to be saved regardless of HLT prescales. These events are not entirely unprescaled because the the L1 trigger prescales are still in effect, but a significant improvement in statistics at lower jet p_T is gained. In order to save as many of these trigger level events as possible, only information essential for further dijet analysis is written to disk. The dijet TLA relies solely on a subset of information from the calorimeter system, and saves trigger bandwidth by neglecting to save information from the muon system, inner detector, and non-essential parts of the calorimeters. This allows for the dijet TLA to collect events that are a small fraction of the size of a standard offline event that saves information from the full set of detector subsystems, with TLA dijet events totaling approximately 5 kB per event versus standard offline dijet events totaling approximately 1 MB per event.

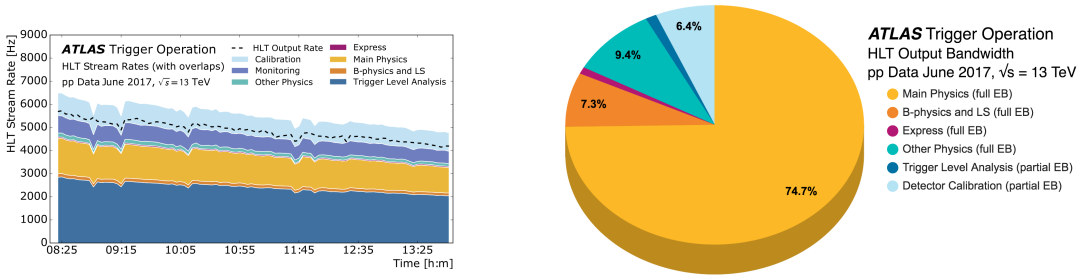

(a) (b)

Figure 5.2: The full HLT event rate separated in terms of various data streams (a) and the corresponding trigger bandwidth used by each data stream (b) for a representative run from 2017 data collection [20].

Through the TLA stream, events are able to be saved at an impressive rate relative to the physics main stream that is used for typical offline analyses. Figure 5.2 shows the total HLT event rate from various data streams, including the TLA stream, and the corresponding trigger bandwidth of each stream from an example run in 2017. It is seen that while the TLA stream clearly has the largest event rate, accounting for about 43% of the total HLT rate, it is only responsible for approximately 1% of the total HLT trigger bandwidth. This obviously leads to a significant increase in the amount data available for analysis at lower dijet mass ranges than is available to a standard offline analysis.

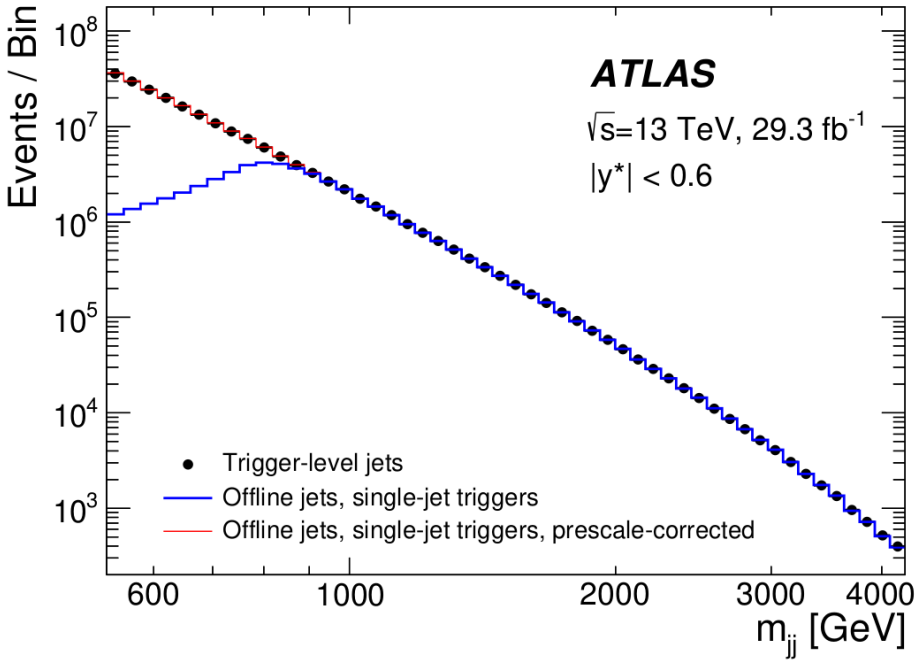

Figure 5.3: The number of dijet events as a function of dijet invariant mass, m_{jj}, collected for use in the TLA analysis (black points) compared to the number of events as selected by single jet triggers with prescaling applied (blue line). Also shown is the number of events corrected for prescaling (red line), representing the expected number of events if the single jet triggers were unprescaled [29].

Recalling from Chapter 4, the single jet triggers active in 2016 were prescaled below jet p_T of 380 GeV. Therefore, a significant number of events with sub-TeV dijet invariant mass are discarded. Figure 5.3 shows the number of events collected as a function of the dijet invariant mass, m_{jj}, as collected by the TLA stream compared to the number of events selected by the suite of active single jet triggers. This plot clearly demonstrates the benefits of the TLA strategy, as the number of events accessible at lower mass values is increased by up to more than an order of magnitude.

5.2 Analysis Strategy

5.2.1 TLA Data Sample

The data sample used in the 2016 dijet TLA analysis discussed here includes only trigger-level jet events. Trigger-level jets are reconstructed using the HLT jet reconstruction algorithm discussed in Chapter 3. The information stored at this level that is accessible for use in the TLA includes the jet four-momentum and a set of calorimeter variables used to characterize the jet quality and structure. This information constitutes only about 0.5% of the size of a full event.

The dijet TLA selected events containing at least one L1 jet with $E_T > 100$ GeV from 2016 data taking, leading to a total analyzed luminosity of 29.3 fb^{-1}. A subset of data was collected containing at least one L1 jet with $E_T > 75$ GeV, amounting to 3.6 fb^{-1} of data using this selection. Naturally, the data selected with the $E_T > 75$ GeV requirement partially overlaps with the data set requiring a L1 jet with $E_T > 100$ GeV.

5.2.2 Trigger-Level Jet Calibration

The calibration scheme for trigger-level jets is very similar to the calibration chain derived for offline jets that was discussed in detail in Chapter 3, with some notable differences necessitated by the limited information available for trigger jets. The full trigger-level jet calibration scheme is summarized in Figure 5.4, with steps unique to the trigger jet-specific calibration outlined with a dashed line. The steps outlined in solid lines will not be discussed in detail here, as they do not differ from what was described previously in Chapter 3.

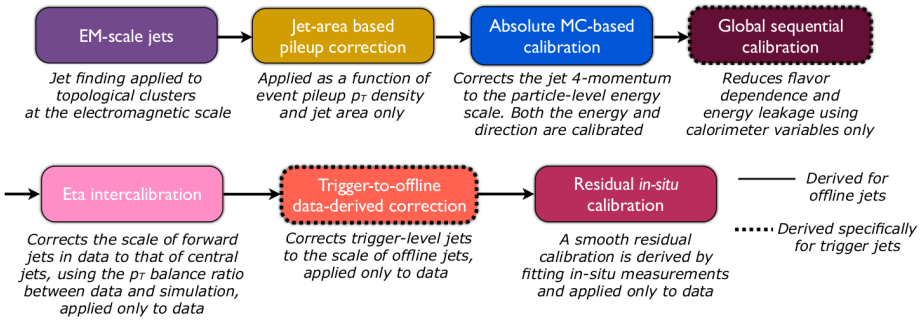

Figure 5.4: The calibration steps applied to trigger-level jets.[29]

The first difference between the trigger-level and offline jet calibration procedures occurs in the Global Sequential Calibration (GSC) step. While a GSC is applied when calibrating both offline and trigger-level jets, the offline version makes use of tracking information, which is not available in trigger-level jet data. Thus, alterations were made to the trigger-level version of the GSC to use only the calorimeter information available. While the offline GSC uses several track-based variables, the trigger-level

GSC makes use of only calorimeter-based variables to reduce the dependence on jet flavor and calorimeter energy leakage. The variables used relate to the trigger-level jet energy fractions in the electromagnetic and hadronic calorimeters and the number of calorimeter cells containing 90% of the trigger-level jet energy. Compared to the previous stage of the calibration chain, these corrections improve the trigger-level jet energy resolution by 8% for jets with p_T of 85 GeV and up to 40% for jets with p_T of 1 TeV.

The next difference between the trigger-level and offline jet calibration schemes is the addition of a trigger-to-offline correction. This correction is based on the jet p_T response and is derived from data in bins of jet η and p_T. The size of the trigger-to-offline correction on average is 1%, growing up to 4% in the endcap regions.

Lastly, the in situ calibration, the final step of the calibration chain, is calculated slightly differently for trigger-level jets than offline jets. The core methods of balancing jets against three types of well-calibrated reference objects (Z bosons, photons, and multijets), as discussed in Chapter 3, remain unchanged, but the fit done to combine these input measurements is calculated differently. While the offline jet in situ calibration uses a spline-based combination procedure, the trigger-level jet in situ calibration curve is produced by a polynomial $\log(p_T)$ fit. This curve serves as the in situ calibration correction applied to trigger-level jets and the choice of fit produces a smoother curve, making the final dijet invariant mass spectrum less sensitive to localized fluctuations in the jet p_T distribution. The trigger-level jet in situ calibration curve is shown in Figure 5.5 alongside the curve produced with the spline combination method for comparison.

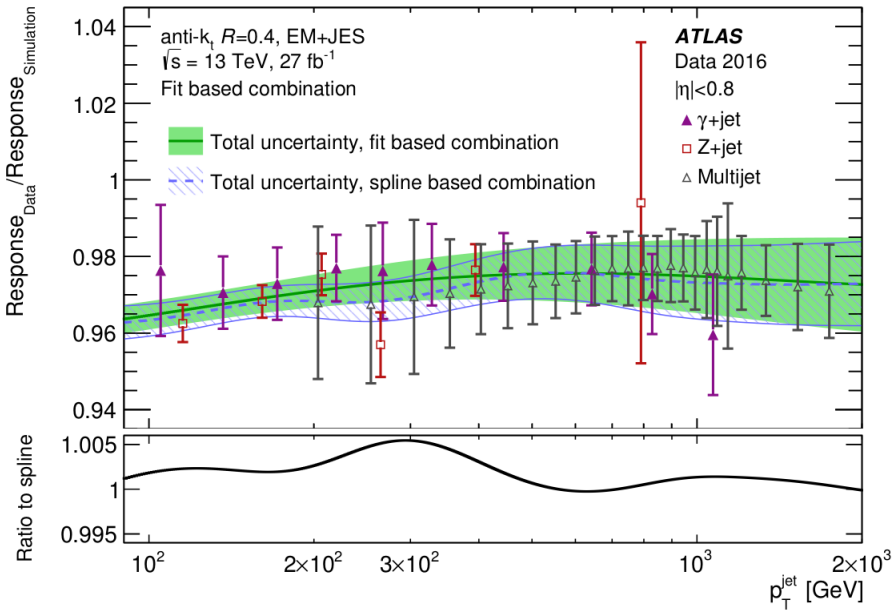

Figure 5.5: The trigger-level in situ calibration curve for both the spline (dashed line) and polynomial $\log(p_T)$ fitted (solid line) combination methods. The lower panel shows the ratio between the curves generated by the two combination methods [29].

After the full trigger-level jet calibration scheme has been applied, the trigger-level jet energy shows agreement with offline jet energy to a degree better than 0.05% for invariant masses of 400 GeV. The difference in jet energy is negligible at an invariant mass of 1 TeV.

5.2.3 TLA Event Selection

Events used for the dijet TLA described here are required to contain at least two trigger-level jets, both with $|\eta| < 2.8$. The leading trigger-level jet is required to have either $p_T > 185$ GeV or $p_T > 220$ GeV for the $E_T > 75$ GeV and $E_T > 100$ GeV L1 trigger selections, respectively. These requirements ensure that the L1 triggers are

fully efficient in the momentum ranges analyzed. The subleading trigger-level jet is required to have $p_T > 85$ GeV for both L1 trigger selections. The jet data quality criteria outlined in [24] is applied to reject jets originating from calorimeter noise, beam-induced background, or cosmic ray particles. The track-based charged fraction selection variable is removed from the data quality checks due to the lack of tracking information in the trigger-level jets, but this is found to have a negligible impact. The trigger-level jet reconstruction efficiency for jets satisfying the selection criteria listed here is 100%, with less than 0.1% of trigger-level jets failing to be reconstructed and selected offline.

The full analysis searches the mass range from 450-1800 GeV for dijet resonances. This is done using two separate selection criteria to cover different but overlapping ranges of the dijet invariant mass spectrum. A selection variable y^*, defined as $y^* = (y_1 - y_2)/2$, where y_1 and y_2 represent the rapidity of the leading and subleading trigger-level jets, respectively, is used to characterize the separation between the leading and subleading trigger-level jets. To search the dijet invariant mass range of 700-1800 GeV using the larger data sample requiring a L1 jet with $E_T > 100$ GeV, events are required to have $|y^*| < 0.6$. The smaller data sample requiring a L1 jet with $E_T > 85$ GeV is used to search the dijet invariant mass range of 450-1800 GeV, requiring events have $|y^*| < 0.3$. The stricter y^* selection is used to select higher-p_T jets at a given invariant mass, leading to a distribution that is unbiased by the leading jet selection for $m_{jj} > 450$ GeV.

5.2.4 Background Estimation

Standard Model predictions state that the dijet invariant mass spectrum is expected to be smoothly falling as mass increases. However, due to the large statistical precision of the trigger-level data collected and the wide range of mass values analyzed, simple functional forms used by previous analyses to describe the shape of the dijet invariant mass spectrum are not adequate to parametrize the shape. Instead, a data-driven sliding-window fit is used to determine the Standard Model dijet invariant mass distribution from data.

$$f(x) = p_1(1-x)^{p_2}x^{p_3+p_4 lnx+p_5 lnx^2} \tag{5.1}$$

$$f(x) = p_1(1-x)^{p_2}x^{p_3+p_4 lnx} \tag{5.2}$$

The sliding-window fit background estimation method is described in full detail in [26],[29]. In short, a fitted curve is evaluated in the center of a window, which then slides bin-by-bin along the full dijet invariant mass distribution. The background estimate is evaluated in each bin in this manner, and the complete background shape is obtained when the results from each bin are combined. Three different functional forms are evaluated for the fit in each bin, and the fit with the best χ^2 value over the full fitted m_{jj} range of each signal selection is chosen. The functional forms of the fits chosen for the $|y^*| < 0.6$ and $|y^*| < 0.3$ signal selections are given by Equations 5.1 and 5.2, respectively. An alternative function is chosen in order to evaluate the systematic uncertainty of the fit by comparing the difference.

5.3 Results

The results of the dijet TLA come from analyzing the dijet invariant mass spectrum as reconstructed with the collected trigger-level events. Figure 5.6 shows the dijet invariant mass distributions reconstructed from data for the $|y^*| < 0.3$ and $|y^*| < 0.6$ signal regions, as well as the background estimates resulting from the sliding window estimates. The data is found to agree well with the Standard Model background and the BumpHunter algorithm [6],[17] is used to identify the most discrepant region between data and the background estimate. The region from 889-1009 GeV for the $|y^*| < 0.6$ signal region is identified as the most discrepant, with a significance of 0.16σ. Clearly, this does not meet the discovery threshold of 5σ, nor is there evidence of any significant excess.

In the absence of a new discovery, limits are set on two physics models- a leptophobic Z' dark matter model, detailed in [7], and a generic Gaussian signal model. The Z' model used assumes the decay rate of the Z' to dark matter particles is negligible and the dijet production rate and resonance width depend solely on the coupling between the Z' and quarks, g_q, and the mass of the Z' particle, $m_{Z'}$. The Guassian model is used to set limits on a generic signal modeled as a Gaussian contribution to the dijet invariant mass spectrum. Gaussian models with four different widths are considered for limit setting- a width equal to the simulated mass resolution, and 5%, 7%, and 10% of the Gaussian signal mass, m_G. The limits set for the Z' and Gaussian models are shown in Figures 5.7 and 5.8, respectively. The full details of the limit setting process may be found in [29].

An obvious feature of the limit plots shown in Figures 5.7 and 5.8 that warrants further discussion is the fluctuation seen around a dijet mass of about 1 TeV. This

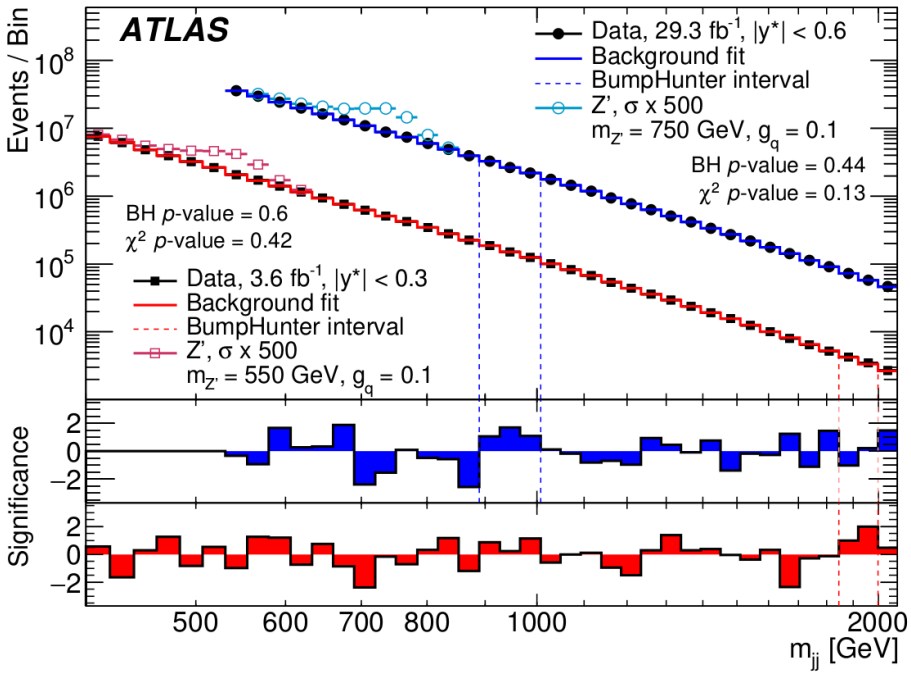

Figure 5.6: The dijet invariant mass distribution reconstructed from trigger-level jets from the $|y^*| < 0.3$ and $|y^*| < 0.6$ signal regions. The results from data (black points) are compared against the background estimates (solid lines). The agreement between data and background is analyzed using the BumpHunter algorithm, with the most discrepant region marked (dashed lines). Also shown are two possible signal models of a hypothetical Z' particle as an example of how a significant signal over background would appear [29].

fluctuation results from a difference in the background estimation methods used in the invariant mass spectrum, seen in Figure 5.6, and the limit setting process. The background estimate used when analyzing the invariant mass spectrum for excesses does not include any contributions from signal in the functional form used to fit the data. However, for the limit setting, the signal shape for each model is included in the background parameterization. A fit of data including both signal and background contributions has more degrees of freedom than a fit of only background, and is thus

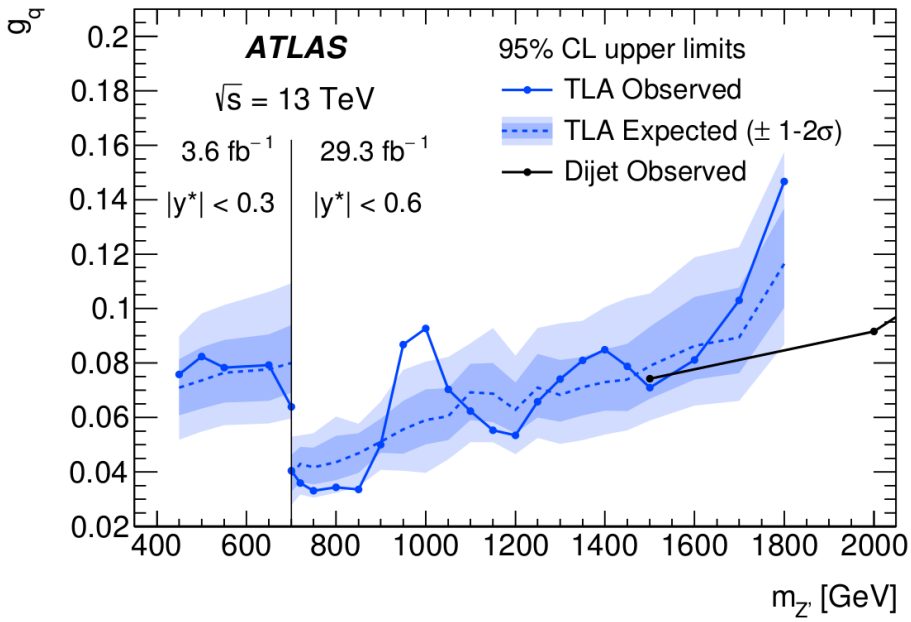

Figure 5.7: The 95% confidence-level upper limits on g_q as a function of m'_Z for the leptophobic Z' dark matter model. A portion of the limits set by an offline dijet search[26] is shown for additional context [29].

more sensitive to fitting local data fluctuations. The expected limits are estimated from the background-only fit and do not account for these fluctuations.

Figure 5.9 provides context for where the limits set by the dijet TLA lie relative to other ATLAS dijet search strategies. While many other dijet searches rely on more unique trigger signatures to collect and analyze data at lower invariant mass ranges, they still suffer from restrictive event rates that prevent them from probing lower ranges of the coupling between quarks and the hypothetical Z' particle, g_q. Improving the constraints set on the coupling requires a larger data sample, as smaller couplings represent rarer and rarer decay processes. This highlights a relative strength of the

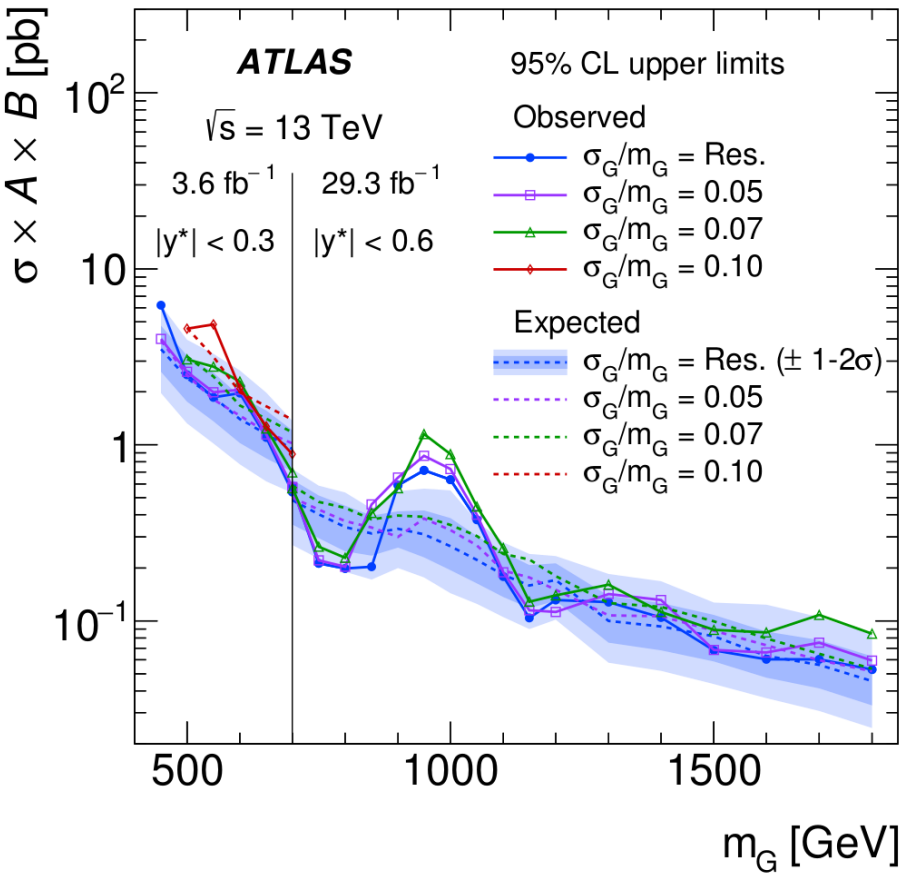

Figure 5.8: The 95% confidence-level upper limits on cross-section times acceptance as a function of m_G for a generic Gaussian signal model. Limits are calculated for four relative Gaussian widths σ_G/m_G [29].

dijet TLA. As is clearly seen in this figure, the limits set by the dijet TLA are able to reach the lowest ranges of g_q due to the very large event rate available to the analysis.

5.4 Full Run-2 Dijet TLA Analysis and End-Of-Fill Data

An updated version of the dijet TLA using the full Run-2 dataset is underway in ATLAS. This will analyze an expanded dataset that includes trigger-level data collected in the 2017 and 2018 data-taking periods. This full dataset is expected to

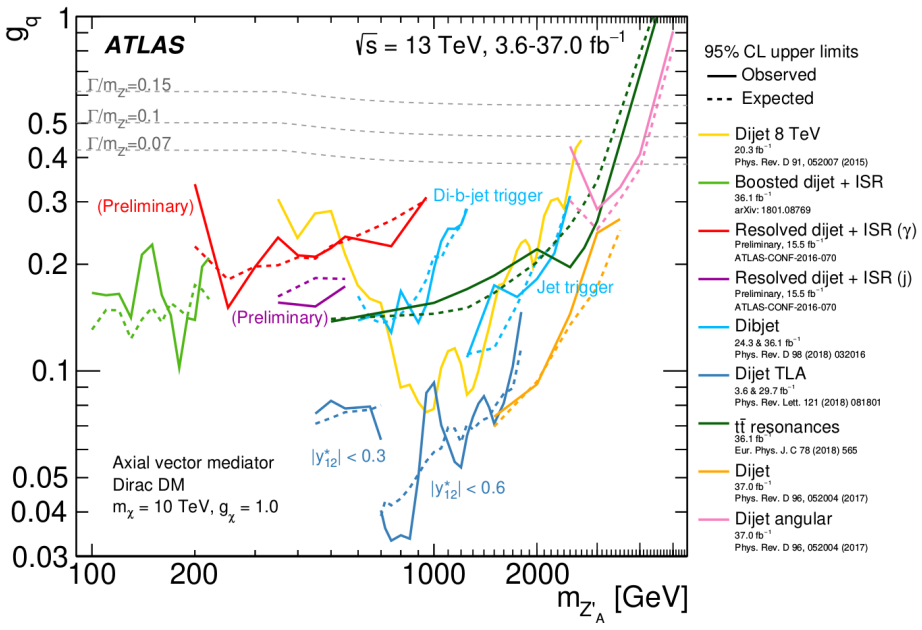

Figure 5.9: A summary of limits set on a Z' dark matter model by various ATLAS dijet searches. Limits on the coupling between quarks and the Z' particle, g_q, as a function of the particle mass, m'_Z. The constraints set by the dijet TLA are shown in blue [30].

further expand the reach of the dijet TLA search strategy to lower couplings and mass ranges. This is thanks to an increase in the amount of data collected, from 36 fb^{-1} in the partial Run 2 analysis to approximately 140 fb^{-1} in the full Run 2 analysis, and the addition of an end-of-fill data collection strategy.

The end-of-fill data collection strategy was added in 2018 and significantly increased the amount of trigger-level data available for analysis while also helping to expand the search range into lower mass ranges. This end-of-fill data represents an exciting addition to the dijet TLA and contributions to the end-of-fill strategy are the primary focus of this section.

As discussed, the TLA strategy leads to a significantly higher event rate of dijet events to analyze than the standard offline analysis methods. However, the TLA is still limited by the L1 trigger rate, which decreases over the course of a LHC fill as the instantaneous luminosity decreases. As the L1 trigger rate decreases with instantaneous luminosity, additional L1 trigger and computing resources are available at these end-of-fill periods. In 2018, the ATLAS end-of-fill strategy put this extra trigger bandwidth to good use, allowing for reconstruction and collection of additional trigger-level events using lower threshold TLA triggers. This provides the TLA with additional events to analyze at a lower mass range than previously accessible when using the L1_J100 and L1_J75 triggers to seed the TLA data stream.

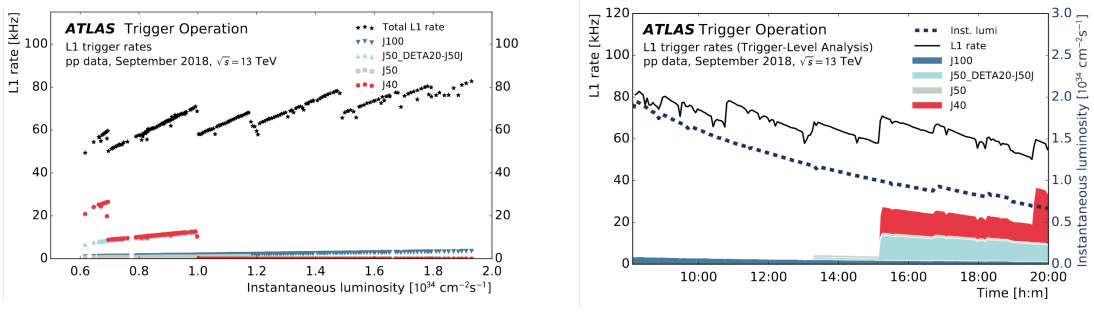

(a) (b)

Figure 5.10: The L1 trigger rate and the rates of L1 triggers that seed the TLA data stream as a function of instantaneous luminosity (a) and time (b) for a LHC fill taken in 2018. The jumps in trigger rate seen are due to adjustments in prescaling at set luminosity thresholds.[20]

Figure 5.10 shows the total L1 trigger rate as a function of instantaneous luminosity and time for an example LHC fill from 2018, with the rates of various L1

triggers that seed the TLA data stream also plotted. The effects of the end-of-fill TLA strategy are readily apparent, with jumps in the L1_J50 and L1_J40 rates in the end-of-fill period. These jumps translate directly to a very large increase in the TLA event rate, as shown in Figure 5.11. As shown, the TLA stream rate reaches as high as about 25 kHz in the end-of-fill period of the run, but still represents just a small fraction of the total output HLT bandwidth due to the very low per event size of the TLA data.

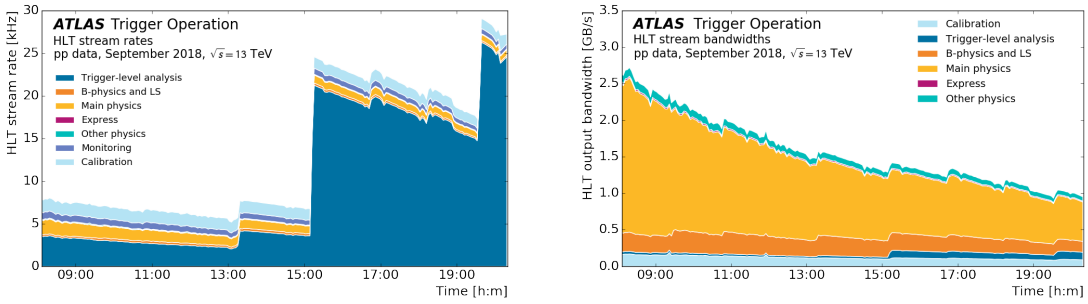

(a) (b)

Figure 5.11: The HLT trigger rate as a function of time (a) and the corresponding HLT output bandwidth (b) for all trigger streams for a LHC fill taken in 2018.[20]

The benefit of adding this end-of-fill data to the full Run-2 dijet TLA is the expanded reach of the analysis into a lower dijet invariant mass range. Referring back to Figure 5.9, there is a large area of g_q-$m_{Z'}$ parameter space where dijet searches have been unable to reach in the low mass and low coupling region. Extending the search range to lower coupling values simply requires more data to be collected to search for extremely rare processes, but the mass range accessible by the dijet TLA

is limited by the L1 triggers used to seed the TLA data stream. The first iteration of the dijet TLA used L1_J75 and L1_J100 to seed the TLA data stream in 2015 and 2016, respectively, and the non-end-of-fill 2017 and 2018 data collection used L1_J100. As is seen in Figure 5.12, which shows the L1 trigger efficiency curves from 2015 and 2016 data for several single jet triggers of interest to the dijet TLA, the L1_J100 trigger does not become fully efficient until approximately 250 GeV. The L1 trigger efficiencies are expected to perform similarly in 2017 and 2018, and thus the start of the dijet invariant mass spectrum reconstructed from trigger-level jets passing this trigger is approximately 500 GeV.

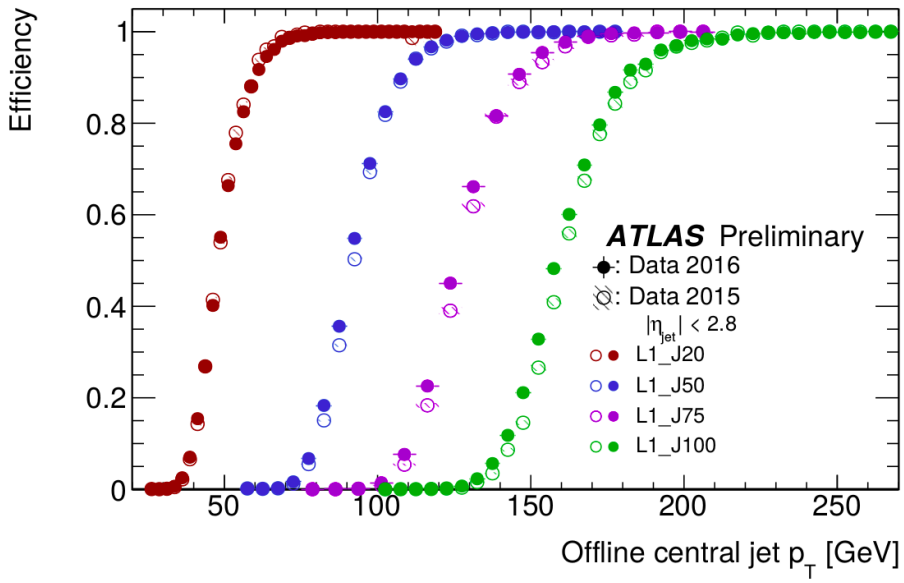

Figure 5.12: The L1 trigger efficiencies for single jet triggers key to seeding the TLA data stream in 2015/2016. The 2016 TLA used data seeded by the L1_J75 and L1_J100 triggers. The efficiencies of these triggers are expected to behave similarly in 2017 and 2018 data [18].

Instead of being limited by the L1_J100 trigger and its efficiency threshold, the end-of-fill TLA data is collected mainly with a TLA data stream seeded by the L1_J40 and L1_J50 triggers. A conservative estimate of the L1 jet trigger efficiency of the L1_J50 trigger from Figure 5.12, which again is assumed to be similar for 2017 and 2018 data, puts the trigger efficiency point around 150 GeV. This allows for the the trigger-jet dijet invariant mass to be reconstructed beginning around 350 GeV. This is a significant improvement in the mass range analyzed, even with very conservative estimates. In the context of Figure 5.9, limits set using end-of-fill TLA data would reach more than 100 GeV lower than those set by the 2016 dijet TLA and reach similar ranges of quark coupling thanks to the very high event rate of the end-of-fill TLA triggers. Therefore, it is expected that, in the absence of a discovery, the end-of-fill TLA strategy will allow for limits to be set on a Z' dark matter model in a low mass, low coupling region not reached by other ATLAS dijet searches.

5.5 Future Trigger-Level Analyses

The dijet TLA has proven that online analysis is a very useful tool for probing regions of parameter space that cannot be reached through offline analysis, and future TLAs represent an exciting direction for the upcoming LHC Run 3 period. Especially with the upcoming High Luminosity LHC upgrade, navigating through jet trigger prescaling to search the low mass region for new physics will continue to require strategies like TLA.

Additional trigger-level tracking capabilities are expected to be available in ATLAS beginning in Run 3. As discussed in Chapter 4, this should improve the performance of the jet triggers system, which may help online analyses maximize their

search range. Additionally, trigger-level tracking will also make possible TLAs that search for signatures beyond just dijet events. This means that dijet plus initial state radiation or multijet TLAs may be possible, which could further extend the search for new physics into the low-mass, low-coupling regime that is currently unreachable, as seen in Figure 5.9. Additional physics signatures including photons and muons may also be possible in future TLAs, allowing for more BSM physics models to be investigated.

Chapter 6: Conclusion

A detailed overview of the ATLAS jet trigger system has been presented, along with a description of the jet detection, reconstruction, and calibration methods used throughout LHC Run 2. An analysis of the performance of the jet trigger system, focusing on small radius HLT jet triggers, was presented. This analysis was done using the full Run 2 dataset collected from 2015 through 2018. Additionally, an analysis searching for evidence of new physics in the dijet invariant mass spectrum using trigger-level jets was also presented.

Hadronic jets are the most prevalent collision products at hadron colliders and thus are extremely important to the search for new physics with ATLAS. Due to the high rate of jet events, aggressive trigger prescaling is implemented, which greatly limits the experimental precision achievable at lower jet p_T values and makes analysis at this important region difficult. Additionally, the effects of pileup are seen to negatively impact jet trigger efficiency. These issues are even more significant with increasing LHC luminosity, as was the case throughout Run 2 and will be a continued consideration moving forward in the LHC physics program. While increasing luminosity is helpful for gaining more data to analyze in the hunt for rare new physics processes, it comes with an unavoidable increase in pileup and stricter jet trigger prescaling.

In order to maximize the discovery potential of analyses involving jet signatures, it is important that the jet triggers perform as efficiently as possible to ensure that the bandwidth allocated to the jet trigger menu is put to good use. One way that the jet trigger efficiencies may be improved is through more effective jet calibrations at the trigger level. Additional jet calibration steps were implemented prior to the 2017 data collection period in the form of the GSC and in situ calibrations. These were seen to lead to improvements in the jet trigger efficiencies and in turn the fraction of events saved by the trigger menu that are useful for further offline analysis. Continued analysis and development of further calibration improvements will continue to be of great importance as the LHC moves into its high luminosity phase beginning in Run 3.

The dijet trigger-level analysis presented uses a novel approach to probe the dijet invariant mass spectrum for signs of new physics using jets at the trigger level. This method allows for HLT prescales to be avoided by saving only the minimum amount of information necessary for the analysis, leading to trigger-level jet events that are only a small fraction of the size of their offline equivalents. The analysis presented used 2015 and 2016 data to set limits on a Z' dark matter model from 450-1800 GeV.

An updated version of the dijet TLA using the full Run 2 dataset is currently underway in ATLAS. This analysis, barring a discovery, is expected to strengthen the limits set by the partial Run 2 analysis with the addition of an end-of-fill strategy that will extend the search range to lower dijet invariant mass ranges. With conservative estimates, the end-of-fill strategy is expected to extend the search range down to approximately 350 GeV, representing a 100 GeV improvement.

Bibliography

[1] Go on a particle quest at the first cern webfest, Aug 2012. https://cds.cern.ch/journal/CERNBulletin/2012/35/News%20Articles/1473657.

[2] Linear Accelerator 2. Sep 2012. https://cds.cern.ch/record/1997427.

[3] The Proton Synchrotron. Jan 2012. https://cds.cern.ch/record/1997189.

[4] The Proton Synchrotron Booster. Jul 2012. https://cds.cern.ch/record/1997372.

[5] The Super Proton Synchrotron. Jan 2012. https://cds.cern.ch/record/1997188.

[6] T. Aaltonen et al. Global search for new physics with 2.0 fb^{-1} at CDF. *Physical Review D*, 79(1), Jan 2009. http://dx.doi.org/10.1103/PhysRevD.79.011101.

[7] Daniel Abercrombie et al. Dark matter benchmark models for early lhc Run-2 searches: Report of the ATLAS/CMS Dark Matter Forum. *Physics of the Dark Universe*, 27:100371, Jan 2020. http://dx.doi.org/10.1016/j.dark.2019.100371.

[8] ATLAS Collaboration. The ATLAS Experiment at the CERN Large Hadron Collider. *JINST*, 3:S08003, 2008.

[9] ATLAS Collaboration. Track reconstruction performance of the ATLAS inner detector at $\sqrt{s} = 13$ TeV. Technical Report ATL-PHYS-PUB-2015-018, CERN, Geneva, Jul 2015. https://cds.cern.ch/record/2037683.

[10] ATLAS Collaboration. Jet reconstruction and performance using particle flow with the ATLAS Detector. *Eur. Phys. J. C*, 77:466, 2017.

[11] ATLAS Collaboration. Topological cell clustering in the ATLAS calorimeters and its performance in LHC Run 1. *Eur. Phys. J. C*, 77:490, 2017.

[12] Cliff Burgess and Guy Moore. *The Standard Model: A Primer*. Cambridge University Press, 2006. http://cds.cern.ch/record/1003111.

[13] Matteo Cacciari, Gavin P Salam, and Gregory Soyez. The anti-kt jet clustering algorithm. *Journal of High Energy Physics*, 2008(04):063–063, apr 2008. https://doi.org/10.1088/1126-6708/2008/04/063.

[14] M Capeans, G Darbo, K Einsweiller, M Elsing, T Flick, M Garcia-Sciveres, C Gemme, H Pernegger, O Rohne, and R Vuillermet. ATLAS Insertable B-Layer technical design report. Technical Report CERN-LHCC-2010-013. ATLAS-TDR-19, Sep 2010. https://cds.cern.ch/record/1291633.

[15] Jean-Luc Caron. Diagram of LHC injection accelerator complex. https://cds.cern.ch/record/841568, May 1993.

[16] Jean-Luc Caron. LHC layout: Schema general du LHC. https://cds.cern.ch/record/841573, Sep 1997.

[17] Georgios Choudalakis. On hypothesis testing, trials factor, hypertests and the bumphunter, 2011. https://arxiv.org/abs/1101.0390.

[18] ATLAS Collaboration. Jet trigger public results run 2. https://twiki.cern.ch/twiki/bin/view/AtlasPublic/JetTriggerPublicResults. Accessed: 2021-10-07.

[19] ATLAS Collaboration. Luminosity public results run 2. https://twiki.cern.ch/twiki/bin/view/AtlasPublic/LuminosityPublicResultsRun2. Accessed: 2021-03-11.

[20] ATLAS Collaboration. Trigger operation public results run 2. https://twiki.cern.ch/twiki/bin/view/AtlasPublic/TriggerOperationPublicResults. Accessed: 2021-03-16.

[21] ATLAS Collaboration. Commissioning of the ATLAS muon spectrometer with cosmic rays. *Eur. Phys. J. C*, 70(arXiv:1006.4384. CERN-PH-EP-2010-045):875–916. 58 p, Aug 2010. https://cds.cern.ch/record/1275998.

[22] ATLAS Collaboration. Tagging and suppression of pileup jets with the ATLAS detector. Technical report, CERN, Geneva, May 2014. https://cds.cern.ch/record/1700870.

[23] ATLAS Collaboration. Jet global sequential corrections with the ATLAS detector in proton-proton collisions at $\sqrt{s} = 8$ TeV. Technical report, CERN, Geneva, Mar 2015. https://cds.cern.ch/record/2001682.

[24] ATLAS Collaboration. Selection of jets produced in 13 TeV proton-proton collisions with the ATLAS detector. Technical report, CERN, Geneva, Jul 2015. https://cds.cern.ch/record/2037702.

[25] ATLAS Collaboration. The Run-2 ATLAS trigger system. Technical Report ATL-DAQ-PROC-2016-003, CERN, Geneva, Feb 2016. https://cds.cern.ch/record/2133909.

[26] ATLAS Collaboration. Search for new phenomena in dijet events using 37 fb[1] of pp collision data collected at $\sqrt{s} = 13$ tev with the atlas detector. *Physical Review D*, 96(5), Sep 2017. http://dx.doi.org/10.1103/PhysRevD.96.052004.

[27] ATLAS Collaboration. Measurement of inclusive jet and dijet cross-sections in proton-proton collisions at $\sqrt{s} = 13$ TeV with the ATLAS detector. *Journal of High Energy Physics*, 2018(5), May 2018. http://dx.doi.org/10.1007/JHEP05(2018)195.

[28] ATLAS Collaboration. Operation and performance of the ATLAS Tile Calorimeter in Run 1. *Eur. Phys. J. C*, 78(CERN-EP-2018-062. 12):987. 69 p, Jun 2018. https://cds.cern.ch/record/2622093.

[29] ATLAS Collaboration. Search for low-mass dijet resonances using trigger-level jets with the ATLAS detector in *pp* collisions at $\sqrt{s} = 13$ TeV. *Phys. Rev. Lett.*, 121:081801. 20 p, Apr 2018. https://cds.cern.ch/record/2312376.

[30] ATLAS Collaboration. Constraints on mediator-based dark matter and scalar dark energy models using $\sqrt{s} = 13$ TeV *pp* collision data collected by the ATLAS detector. *JHEP*, 1905:142. 84 p, Mar 2019. https://cds.cern.ch/record/2665436.

[31] ATLAS Collaboration. Jet energy scale and resolution measured in proton-proton collisions at $\sqrt{s} = 13$ TeV with the ATLAS detector, 2020. https://arxiv.org/abs/2007.02645.

[32] Bogdan A. Dobrescu and Felix Yu. Coupling-Mass mapping of dijet peak searches. *Phys. Rev. D*, 88:035021, Aug 2013. https://link.aps.org/doi/10.1103/PhysRevD.88.035021.

[33] R. K. Ellis, W. J. Stirling, and B. R. Webber. *QCD and Collider Physics*. Cambridge Monographs on Particle Physics, Nuclear Physics and Cosmology. Cambridge University Press, 1996. https://cds.cern.ch/record/318585.

[34] Lyndon Evans and Philip Bryant. LHC machine. *JINST*, 3:S08001, 2008.

[35] Christian Wolfgang Fabjan and F Gianotti. Calorimetry for particle physics. *Rev. Mod. Phys.*, 75(CERN-EP-2003-075):1243–1286. 96 p, Oct 2003. https://cds.cern.ch/record/692252.

[36] L. A. Harland-Lang, A. D. Martin, P. Motylinski, and R. S. Thorne. Parton distributions in the LHC era: MMHT 2014 pdfs. *The European Physical Journal C*, 75(5), May 2015. http://dx.doi.org/10.1140/epjc/s10052-015-3397-6.

[37] P Lipari. Introduction to neutrino physics. 2003. https://cds.cern.ch/record/677618.

[38] Simone Marzani, Gregory Soyez, and Michael Spannowsky. *Jets and Jet Algorithms*, pages 23–34. Springer International Publishing, Cham, 2019. https://doi.org/10.1007/978-3-030-15709-8_3.

[39] ATLAS Outreach. ATLAS fact sheet : To raise awareness of the ATLAS detector and collaboration on the LHC. https://cds.cern.ch/record/1457044, 2010.

[40] Joao Pequenao. Computer generated image of the ATLAS calorimeter. https://cds.cern.ch/record/1095927, Mar 2008.

[41] Joao Pequenao. Computer generated image of the ATLAS inner detector. https://cds.cern.ch/record/1095926, Mar 2008.

[42] Joao Pequenao. Computer generated image of the ATLAS muons subsystem. https://cds.cern.ch/record/1095929, Mar 2008.

[43] Joao Pequenao. Computer generated image of the whole ATLAS detector. https://cds.cern.ch/record/1095924, Mar 2008.

[44] J. Proudfoot. Hadron calorimetry at the LHC. *34th SLAC Summer Institute on Particle Physics*, 2006. https://www.slac.stanford.edu/econf/C060717/papers/L012.PDF.

[45] Andrei D Sakharov. Violation of cp invariance, c asymmetry, and baryon asymmetry of the universe. 34(5):392–393, may 1991. https://doi.org/10.1070/pu1991v034n05abeh002497.

[46] Matthias Schott and Monica Dunford. Review of single vector boson production in pp collisions at $\sqrt{s} = 7$ TeV. Review of single vector boson production in pp collisions at $\sqrt{s} = 7$ TeV. *Eur. Phys. J. C*, 74(arXiv:1405.1160):60 p, May 2014. https://cds.cern.ch/record/1699952.

[47] I. Wingerter-Seez. Particle physics instrumentation. (arXiv:1804.11246):20 p, Apr 2018. https://cds.cern.ch/record/2315747.

[48] P.A. Zyla et al. Review of particle physics. *PTEP*, 2020(8):083C01, 2020.